Receptivity and Growth of Two- and Three-Dimensional Disturbances in a Blasius Boundary Layer

by

Rudolph A. King

B.S.M.E., Old Dominion University (1987)
M.S., Old Dominion University (1991)

Submitted to the Department of Aeronautics and Astronautics
in partial fulfillment of the requirements for the degree of
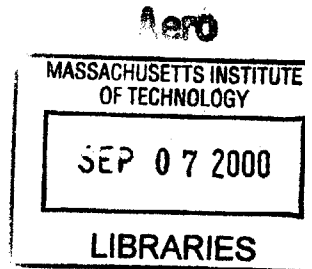
Doctor of Philosophy

at the

MASSACHUSETTS INSTITUTE OF TECHNOLOGY

February 2000

© Rudolph A. King, 1999. All rights reserved.

Author_____
Department of Aeronautics and Astronautics
November 18, 1999

Certified by_____
Kenneth S. Breuer
Visiting Associate Professor
Thesis Supervisor

Certified by_____
Mark Drela
Associate Professor
Committee Member

Certified by_____
Ian A. Waitz
Associate Professor
Committee Member

Certified by_____
Richard W. Wlezien
Program Manager, Tactical Technology Office, DARPA
Committee Member

Accepted by_____
Professor Nesbitt W. Hagood IV
Chairman, Department Committee on Graduate Students

Receptivity and Growth of Two- and Three-Dimensional Disturbances in a Blasius Boundary Layer

by

Rudolph A. King

Abstract

In this experimental study, acoustic receptivity was examined for a Blasius boundary layer formed on a flat plate. Non-localized surface roughness, 2-D and oblique, were considered for various roughness heights and acoustic wave amplitudes. The receptivity sites (surface roughness) had a well defined wavenumber spectrum with a fundamental wavenumber of k_w. A planar downstream-traveling acoustic wave was created to temporally excite the flow near the resonance frequency, ω_{ts}, of an unstable eigenmode corresponding to $k_{ts} = k_w$. Branch I was selected to occur near the streamwise center of the roughness to maximize the receptivity. The range of acoustic forcing levels ϵ and roughness heights Δh examined resulted in a linear dependence of receptivity coefficients; however, the larger values of the combination $\epsilon \cdot \Delta h$ resulted in subsequent nonlinear development of the Tollmien-Schlichting (T-S) wave. The measured receptivity was seen to increase markedly with increasing obliqueness of the surface roughness patterns. Detuning of the 2-D and oblique disturbances was investigated by varying the streamwise wall-roughness wavenumber α_w and measuring the T-S response. Oblique transition was also investigated by exciting a pair of oppositely-oriented oblique Orr-Sommerfeld modes $(\omega/\omega_{ts}, \pm\beta/\beta_w) = (1, \pm 1)$. For small values of $\epsilon \cdot \Delta h$, a peak-valley structure corresponding to a spanwise wavenumber of $2\beta_w$ was observed. The maximum streamwise velocity fluctuations, $u_t(f_o)$, occur at peak locations as expected. For the largest value of $\epsilon \cdot \Delta h$, significant mean-flow distortion was observed in the mean streamwise velocity. Large spanwise velocity gradients, $|dU/d\zeta|$, exist between peaks and valleys and appear to generate a secondary instability. The maximum values of u_t no longer occur at peak locations of the stationary structure but at locations of spanwise inflection points. The magnitude of u_t scales with $|dU/d\zeta|$. A nonlinear interaction of two nonstationary modes was conjectured as a possible mechanism for the enhancement of the streak amplification rate.

Thesis Supervisor: Kenneth S. Breuer
Title: Visiting Associate Professor

Acknowledgments

Contents

6

List of Figures

10

11

13

List of Tables

List of Symbols

A cross-sectional area.

a_n coefficients used throughout document (e.g. hot-wire calibration).

B number of rotor blades.

$\hat{B}_X$ bias limit of X.

C receptivity coefficient referenced to Branch I, $\frac{u_{ts,I}}{u_{ac}}$.

c acoustic wave speed.

c_{ph} phase speed of boundary-layer disturbance.

E mean hot-wire voltage.

E_c corrected mean hot-wire voltage.

$e(t)$ fluctuating hot-wire voltage.

F nondimensional frequency, $2\pi f \nu / U_\infty^2$.

f frequency in Hz.

f   data reduction equation.

f_o applied frequency of controlled acoustic field.

H shape factor, δ^*/θ.

h normalized step height, $\Delta h_k / \Delta h_1$ where $k = 1, 2$, or 3.

k wavenumber, $(\alpha^2 + \beta^2)^{1/2}$, or spatial harmonic of stator vanes.

M molecular weight.

N LST amplification factor, $\int_{x_I}^x -\alpha_i(x; f) dx$.

n harmonic of blade passing frequency.

P mean pressure.

$\hat{P}_X$ precision limit of X.

p fluctuating pressure.

R	Reynolds number base on δ_r, $\sqrt{Re_x}$.
R_a	ideal gas constant for dry air.
Re	Unit Reynolds number, $\rho U_\infty / \mu$.
Re_x	Reynolds number based on x, $\rho U_\infty x_v / \mu$.
r	hot-wire sensor resistance.
$S_A(f)$	auto power spectral density of A.
$S_{A,B}(f)$	cross power spectral density between A and B.
SPL	sound pressure level, $SPL = 20 \cdot \log \left(\frac{p_{ac}}{20\mu Pa} \right)$.
$\hat{S}_X$	precision index (sample standard deviation).
T	temperature.
t	time.
U	mean streamwise velocity.
U_∞	mean freestream velocity.
$\hat{U}_X$	uncertainty of X.
u	broadband rms streamwise fluctuating velocity.
u_{ac}	rms freestream velocity amplitude induced by forced acoustic field.
u_t	narrow-band rms streamwise disturbance velocity.
u_{ts}	narrow-band rms streamwise T-S velocity.
V	number of stator vanes.
X	independent variable in uncertainty analysis.
x	streamwise distance measured from leading edge of model.
x_o	virtual origin location.
x_v	streamwise distance measured from virtual origin, $x - x_o$.
y	wall-normal distance measured from model surface.
z	spanwise distance measured from tunnel centerline.
α	streamwise wavenumber or temperature coefficient of hot-wire sensor.
α_i	spatial amplification rate.
β	spanwise wavenumber.
ΔU	maximum U difference in spanwise survey (measure of streak amplitude).
Δh	surface roughness step height.

δ	boundary-layer thickness
δ_r	nondimensional length scale used in LST, x/R.
δ^*	displacement thickness.
$\delta(\frac{U}{U_\infty})$	difference between perturbed and unperturbed (reference) velocity.
ϵ	normalized acoustic wave amplitude, u_{ac}/U_∞.
ϕ	phase of disturbance velocity or relative humidity.
γ	coherence function between signals A and B, $\frac{|S_{A,B}(f)|^2}{S_A(f) \cdot S_B(f)}$.
η	normalized wall-normal coordinate, $(y/x_v) \cdot Re_x^{1/2}$.
λ	wavelength, $2\pi/k$.
μ	viscosity.
ν	kinematic viscosity, μ/ρ.
θ	momentum thickness or circumferential coordinate.
$\hat{\theta}$	absolute sensitivity coefficients.
ρ	density.
σ	detuning parameter, $\frac{\alpha_w - \alpha_{ts,I}}{\alpha_{ts,I}}$.
σ'	detuning parameter for finite acoustic wave speed, $\sigma + \frac{\alpha_{ac}}{\alpha_{ts,I}}$.
τ_r	hot-wire resistive overheat ratio, r_{hw}/r_{cw}.
Ω	angular frequency of rotor.
ω	radian frequency, $2\pi f$.
ψ_w	angle between roughness wavenumber vector and streamwise direction.
ζ	nondimensional spanwise coordinate measured from roughness centerline.

Subscripts

$1, 2, 3$	acoustic forcing level and step height designations (refer to Table 3.1).
a	dry air property.
ac	freestream acoustic field.
cw	cold wire.
dn	downstream-traveling component.

e	test-section entrance.
I	Branch I (lower branch) location.
rs	rough surface .
rw	heated wire.
sat	saturation vapor property.
sc	settling chamber.
ss	smooth surface .
T	total (stagnation) condition.
tr	laminar-to-turbulent transition.
ts	T-S wave.
up	upstream-traveling component.
v	water vapor property.
w	surface roughness condition.

Chapter 1

Introduction

Laminar-to-turbulent transition of boundary-layer flows remains one of the key unresolved problems in fluid mechanics to date. The state of a boundary layer, laminar or turbulent, dramatically affects parameters such as skin friction, form drag, heat transfer rates, etc. Practical applications that are affected include, but are not limited to, controllability of airfoils and high-lift devices, turbine and engine performance, and aircraft and spacecraft performance. An understanding of the transition process can lead to improved transition prediction techniques and eventually transition control methodologies. This can ultimately result in improvements of air transportation (civil, military, and space) safety with enormous economic benefits in light of predicted increases in air-travel density at the turn of the century.

1.1   Background

1.1.1   Brief historical overview of boundary-layer transition

Research has been conducted in boundary-layer transition for over a century starting with the classical pipe-flow transition experiment of Reynolds [1] in the late 1800's. At elevated flow speeds, spark photography of injected dye tracers revealed a relatively distinct set of eddies in rapid (high frequencies) three-dimensional motion. More than four decades later, calculations of the Orr-Sommerfeld equations predict-

ing the growth of small two-dimensional wave-like disturbances for laminar flow over a flat plate were performed by Tollmien [2] and Schlichting [3]. These wave-like disturbances later became known as Tollmien-Schlichting (T-S) waves. The notion that the transition process was initially excited by two-dimensional T-S waves was largely ignored by the research community because it was not believed that such an instability existed and because of the overwhelming experimental evidence of the highly three-dimensional nature of transition leading to turbulence. Due to the high freestream turbulence levels of wind tunnels at the time, these two-dimensional disturbances were not realizable by experimentalists for many years because of the rapid boundary-layer transition via the freestream turbulence mechanism. A ground-breaking experiment was conducted at the National Bureau of Standards in the 1940's by Schubauer & Skramstad [4]. By significantly reducing the freestream turbulence intensity using damping screens and honeycombs, they measured growth rates and propagation speeds of wave-like two-dimensional disturbances excited by an oscillating ribbon placed near the plate surface. Their results were in substantial agreement with the predictions of Tollmien [2] and Schlichting [3]. Some years later, Emmons [5] noticed the intermittent appearance of turbulent spots (also referred to as Emmons spots) surrounded by laminar flow in shallow running water. Several years later, the disconnect between the initially two-dimensional T-S waves and the formation of turbulent spots was addressed in the experiments of Klebanoff & Tidstrom [6] and Klebanoff, Tidstrom, & Sargent [7]. Their experiments demonstrated that after a sufficiently large amplitude was achieved for the two-dimensional T-S wave, three-dimensionality with spanwise periodicity ensued and resulted in longitudinal vorticity and spanwise energy redistribution.

1.1.2 Boundary-layer transition overview

In this section, a brief overview of the transition process in a wall-bounded shear flow is presented for the scenario where small wave-like disturbances are amplified to finite levels leading to laminar breakdown. A sketch depicting a typical transition process is presented in Figure 1-1. The transition process can be described as a three-stage
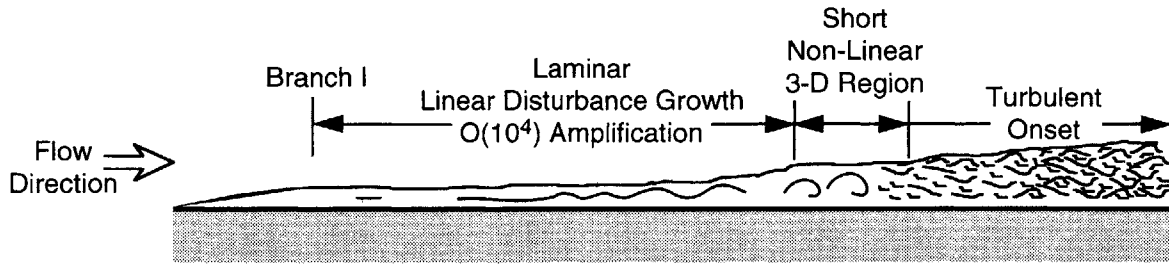
Figure 1-1: Schematic depicting a typical transition process in the absence of a bypass mechanism.

process: *(i)* the receptivity stage, *(ii)* the linear-amplification stage, and *(iii)* the nonlinear stage.

The linear-amplification (second) stage of the transition process has been studied for many years and is the most understood of the three stages. This stage is modeled using linear stability theory (LST), governed by the well-known Orr-Sommerfeld equation for an incompressible flow, where an incipient instability in the base flow is allowed to grow. A complete review of linear stability theory is readily available in the literature (e.g. Schlichting [8] and Mack [9]). Linear stability theory assumes that the mean (base) flow is perturbed by small amplitude oscillations in velocity and pressure which may vary (grow, decay, or remain constant) in both time and space. Three-dimensional disturbances of the form $u', v', w', p' \sim e^{i(\alpha x \pm \beta z - wt)}$ with angular frequency ω and streamwise and spanwise wavenumbers α and β are assumed. These instabilities may possess different forms including T-S instabilities, crossflow instabilities (see Reed *et al.* [10]), and Görtler instabilities (see Saric [11]). In this document, instabilities are limited to the T-S type and the reader can refer to the cited review papers for other forms of instabilities. The linear stage typically evolves over an extended spatial distance as indicated in Figure 1-1 with amplification on the order of 10^3 - 10^4 for small initial amplitudes. The spatial amplification growth rate α_i (for the spatial approach α is assumed complex, i.e. $\alpha = \alpha_r + i\alpha_i$) determines the evolution of the disturbances. The disturbances grow for $\alpha_i < 0$, decay for $\alpha_i > 0$, and are neutrally stable for $\alpha_i = 0$. A typical plot of nondimensional spatial growth rates, α_i^*, versus Reynolds number, R, for a two-dimensional T-S wave of fixed frequency is presented in Figure 1-2. The data were computed using LST at a

25
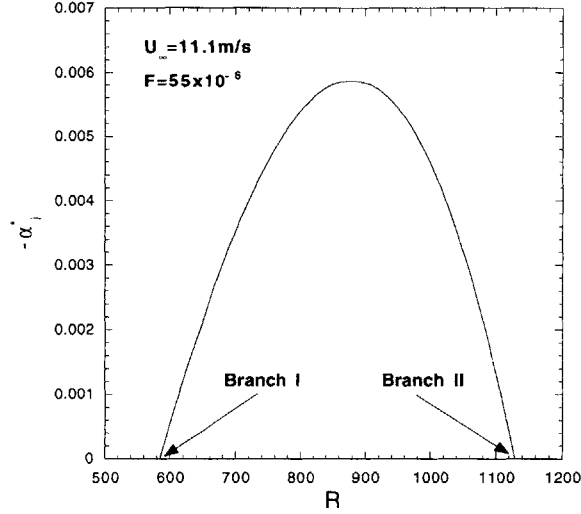
Figure 1-2: Nondimensional spatial growth rates, α_i^*, for a two-dimensional T-S wave computed using LST. The growth rate is nondimensionalized by δ_r.

nondimensional frequency F $(= 2\pi f\nu/U_\infty^2)$ and nondimensionalized using the length scale δ_r $(\delta_r = x/R)$. Amplification occurs for $-\alpha_i^* > 0$. The locations of Branch I (lower branch) and Branch II (upper branch) are indicated in the figure. The locus of neutrally stable points $(\alpha_i = 0)$ in the F versus R plane forms a boundary between stability and instability. Figure 3-2 shows a neutral stability plot for a Blasius boundary layer. Amplification or N factors are computed using the growth rates for a given dimensional frequency f as follows

$$N(x; f) = \int_{x_I}^{x} -\alpha_i(x; f)dx \tag{1.1}$$

where x_I is the Branch I location. The disturbance amplitude ratios are then calculated using the N factors. For example, the streamwise velocity disturbance (root-mean-square) amplitude ratio is given by

$$\frac{u_{ts}}{u_{ts,I}} = e^N. \tag{1.2}$$

Here $u_{ts,I}$ is the T-S amplitude at Branch I, which will be used in the definition of the receptivity coefficient C $(= u_{ts,I}/u_{ac})$. LST has been applied with some success to predict the onset of transition using the e^N method proposed by Smith & Gamberoni [12] and Van Ingen [13]. The e^N method is a semiempirical method that uses LST to determine the value of N (amplitude ratio $= e^N$ relative to the lower neutral

stability point (Branch I)) that correlates with experimentally measured transition locations. Typical values of N in the literature may range from 7 to 9, depending on the flow geometry and external disturbance environment. An overview outlining different applications of e^N method is given by Bushnell et al. [14].

The final and generally *explosive* stage in the transition process is the nonlinear stage which is characterized by significant three dimensionality and a short time scale relative to that in the linear-growth region. Here the disturbances grow to large enough amplitudes that mode interaction can occur. The large T-S amplitudes and nonlinear interactions can sufficiently distort the base flow such that it can sustain a secondary instability (see Herbert [15]) in the form of oblique waves. This leads to a spanwise alternating peak-valley structure and the formation of Λ-vortices. Depending on the primary T-S disturbance and the background disturbance spectra, the Λ-vortices may be aligned or staggered indicating fundamental (K-type) or subharmonic (C-type or H-type) breakdown, respectively. The nonlinearity remains operative until the boundary layer becomes completely turbulent. Refer to Section 1.1.4 for more on the different paths to laminar breakdown.

In the initial stage, the term *receptivity* (Morkovin [16]) is used to define the process by which external disturbances are internalized into the boundary layer to generate boundary-layer instability waves. External disturbances can include freestream disturbances (which may be acoustic and/or vortical in form), surface inhomogeneities such as short-scale variations in surface geometry (i.e. roughness) and/or imposed velocities at the surface (via suction/blowing or surface vibration). Receptivity is perhaps the least understood of the three stages; however, considerable advances have been made in this area in the past two decades. A fundamental understanding of receptivity is important since it provides the initial conditions (amplitude, frequency, and phase) for the subsequent growth of unstable modes which may ultimately lead to laminar breakdown. Because of the significant wavelength mismatch between the long-wavelength freestream disturbances and the much shorter wavelength T-S waves, a length-scale conversion must take place to facilitate the energy transfer required for excitation of the instability modes. Receptivity occurs in regions where nonparallel
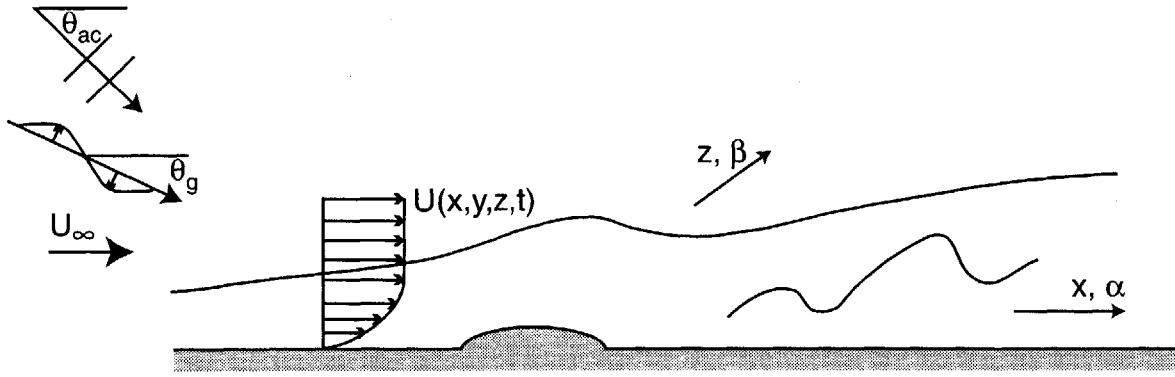
Figure 1-3: Schematic depicting the receptivity process resulting from the interaction of freestream acoustic and/or convected gust and a surface inhomogeneity.

effects are significant, such as regions near the leading edge and abrupt changes in surface geometry. A schematic depicting the receptivity problem in the vicinity of a surface hump is given in Figure 1-3. Acoustic and vortical (gust) freestream disturbances are indicated in the figure at inclination angles of θ_{ac} and θ_g, respectively. Note that the gust, used to model spanwise vorticity in freestream turbulence, produces vorticity and velocity fluctuations normal to the propagation direction. The velocity fluctuations produced by freestream acoustic (sound) disturbances are parallel to the propagation direction. The flow depicted here has to make an abrupt adjustment in the presence of the surface inhomogeneity which facilitates the receptivity process. The excited instability waves are characterized by the streamwise, α, and spanwise, β, wavenumbers associated with the surface inhomogeneity and temporal scale of the freestream disturbances. The receptivity problem along with some relevant receptivity studies are addressed in Section 1.1.3.

This three-stage process represents a fairly adequate representation of laminar-to-turbulent transition. Transition scenarios that do not follow this general trend, in particular the omission of the linear-amplification region, was termed *bypass* transition by Morkovin [17] due to the lack of understanding of the process.

28

1.1.3 Receptivity

In this section, a brief review of the literature on receptivity with respect to the generation of T-S instability waves will be presented. The review included here in no way represents a comprehensive list of available literature. There are many unresolved issues with regards to the many different paths through which a disturbance can be introduced into a boundary layer. The question of how the external disturbance environment excites T-S instability waves of the boundary layer was not resolved until two decades ago. It was long recognized that the receptivity problem was mathematically different from the stability problem (see Reshotko [18]). Receptivity must be posed mathematically as an initial value problem as opposed to an eigenvalue problem for stability. The early theoretical works of Goldstein [19, 20, 21], Zavol'skii *et al.* [22], and Ruban [23] solidified the mechanisms by which long-wavelength freestream disturbances at a particular frequency are converted to a wavelength commensurate with the boundary-layer instability wave. They utilized high Reynolds number asymptotic methods to analyze the receptivity problem. They showed that receptivity occurs in regions where the boundary-layer flow changes abruptly in the streamwise direction, i.e. significant nonparallel effects.

Two general classes of receptivity regions were recognized by Goldstein, I) the leading edge regions where the boundary layer is thin and growing rapidly and II) regions further downstream where the boundary layer is forced to make a rapid adjustment. A common feature between both receptivity regions, classes I and II, is the importance of nonparallel effects and is manifested via the disturbance motion being governed by the unsteady boundary-layer equations. Class II can be further subdivided into *localized* and *non-localized* receptivity. Localized receptivity results from an interaction between the freestream disturbances and steady localized disturbance generated by a surface inhomogeneity (e.g. humps, gaps, suction/blowing slots, etc.). On the other hand, non-localized receptivity stems from an interaction in boundary-layer flow with unsteady freestream disturbances and the steady disturbance created over surfaces with extended regions of short-scale variations (e.g. waviness, distributed

roughness, uneven suction, etc.). Choudhari [24] investigated the extent of synchronization between the surface waviness and neutral instability motion, where for perfect resonance at Branch I $\alpha_w = \alpha_{ts,I}$. Here α_w and $\alpha_{ts,I}$ denote the wall wavenumber and instability wavenumber at Branch I, respectively. He shows that the extent of the resonance region corresponds to a spatial extent of $\Delta x = O(x_I \cdot R_I^{-3/8})$, which is of the same order as the geometric mean of the distance from the leading edge and instability wavelength at Branch I. This implies a synchronized surface waviness will lead to instability amplitudes which are larger than those produced by an isolated surface roughness by a factor of $O(R_I^{3/8})$. Choudhari's simple analytical result helped to explain some earlier results computed by Crouch [25] where he found significantly larger values for non-localized receptivity versus localized receptivity. Reviews of different receptivity mechanisms are given by Goldstein & Hultgren [26], Kerschen [27], Heinrich et al. [28], Choudhari & Streett [29], Crouch [30], Nishioka & Morkovin [31], Kozlov & Ryzhov [32], Wlezien [33], Saric et al [34], and Kachanov [35].

Leading-edge receptivity

There has been significant progress made in reconciling differences between experiment and theory for leading-edge receptivity due to acoustic excitation. The same progress has not been forthcoming for receptivity due to freestream turbulence. Acoustic receptivity is the main focus in this document and as a result, receptivity due to acoustic excitation will be emphasized in the discussions.

<u>Acoustic excitation:</u>   The wealth of experimental studies conducted on leading-edge receptivity has been conducted with controlled acoustic freestream excitation. These include experiments by Leehey and coworkers [36, 37, 38, 39, 40], Dovgal et al. [41], Ball [42], Parekh et al. [43], Wlezien et al. [44], and Saric et al. [45, 46, 47, 48]. Theoretical calculations by Heinrich et al. [28] show that leading-edge receptivity on an infinitely thin flat plate is highly dependent on disturbance orientation for both acoustic and convected gust excitation. For acoustic excitation, receptivity is minimum for downstream-traveling acoustic excitation ($\theta_{ac} = 0°$) and maximum

for upstream-traveling excitation ($\theta_{ac} = 180°$). For downstream-traveling excitation, receptivities for both acoustic and convected gust excitation are on the same order of magnitude [28].

The early experiments of Leehey & Shapiro [36, 37] examined the effects of acoustic receptivity on a flat-plate boundary layer with a 6 : 1 elliptic leading edge in a low-turbulence wind tunnel. They found that the T-S wave amplitude was proportional to the acoustic excitation (receptivity was found to be $O(1)$) for acoustic levels large enough so that the T-S wave was not dominated by freestream turbulence. Upstream of Branch I, a standing wave pattern with wavelength equal to the T-S wave at the excitation frequency was measured. Downstream of Branch I, T-S growth was observed with a phase corresponding to the calculated phase speed of the T-S wave given by LST. Leehey & Shapiro postulated that, whatever the mechanism, the acoustic waves excited T-S waves in the immediate region of the leading edge. The theoretical work of Goldstein [19] demonstrated that T-S waves are generated near the leading edge of an infinitely thin flat plate where nonparallel effects are significant supporting the conclusion drawn by Leehey & Shapiro [36, 37]. Later experiments by Leehey et al. [39, 40] demonstrated the generation of T-S waves for both sound and vibration excitation near the leading edge of the flat-plate model.

The experimental study of Ball [42] investigated leading-edge receptivity of a flat-plate boundary layer for various acoustic excitation angles of incidence. His high-frequency results for normal incidence of the acoustic excitation demonstrated the importance of the leading-edge diffraction field to the receptivity process (see theoretical work by Heinrich et al. [28]). The receptivity ratio of the upstream-traveling (grazing) versus the normal incidence acoustic excitation for the experimental [42] and theoretical [28] studies were in reasonable agreement. For the low-frequency results of Ball [42], the receptivity mechanism for the normal incidence excitation was in substantial agreement with the high-frequency results and theory [28]. However, for the upstream-traveling excitation a different receptivity mechanism was realized, namely receptivity at the juncture of the leading edge and flat plate.

Hammerton & Kerschen [49, 50] theoretically considered the effects of finite thickness distribution with parabolic leading edges on acoustic receptivity. The nose radius enters the theory in the definition of the Strouhal number. Their results show for a Strouhal number of 0.3, a significant reduction in the receptivity level compared to an infinitely thin flat plate. For small Strouhal numbers, their solutions revealed a divergence between asymptotic and numerical results [50]. Their findings clearly demonstrated the importance of including the effects of finite nose radius in any receptivity study. The receptivity to freestream acoustic disturbance of a laminar boundary layer over a semi-infinite flat plate with an elliptic leading edge was investigated using direct numerical simulations by Lin et al. [51]. The effect of leading-edge curvature was studied for a grazing sound wave ($\theta_{ac} = 0°$) by varying the aspect ratio of the ellipse. The boundary layer was found to be less receptive with a sharper leading edge. The receptivity contribution from the discontinuity in curvature at the juncture of the leading edge and flat plate was a significant fraction of the total receptivity. A new leading-edge geometry for flat plates, based on a modified super ellipse, was proposed to eliminate the receptivity contribution due to the discontinuous curvature. Experiments by Saric et al. [45, 46, 47, 48] were conducted, and continue to this date, to study acoustic receptivity of flat-plate boundary layers with modified super ellipses. Two modified super ellipses were considered, a 20 : 1 and 40 : 1. Larger receptivity was observed for the 20 : 1 modified super ellipse than for the 40 : 1 modified super ellipse. These as well as other results are summarized by Saric et al. [52].

Freestream turbulence excitation: Understanding of leading-edge receptivity to freestream turbulence is much more perplexing than the acoustic counterpart (see review by Kendall [53]). This is due in part to the fact that no method currently exists for creating reproducible or repeatable turbulence. A brief overview is presented here for completeness, but the interested reader can refer to the cited papers for more information. Limited experiments have been performed to study the effects of freestream turbulence on the generation of T-S waves at the leading edge of flat-plate models

(e.g. Klebanoff [54], Kachanov *et al.* [55], Kendall [56, 57, 58, 59, 53], Westin *et al.* [60], and Boiko *et al.* [61]). Direct numerical calculations to investigate the effects of freestream vorticity on receptivity for a flat plate with an elliptic leading edge was conducted by Buter & Reed [62] (also refer to theoretical references cited earlier). A clear connection has not yet been established experimentally between the ingestion of freestream turbulence into the laminar boundary layer and the generation of T-S waves which may ultimately lead to breakdown. The original work on the effect of freestream turbulence on laminar boundary layers (flat plate) was done by Klebanoff and the only report exist in the form of an abstract [54]. The freestream turbulence level was increased from its baseline value by installing grids in the settling chamber. He observed low-frequency ($f < 12Hz$) perturbations in the boundary layer where the wall-normal profiles of the perturbations resembled a thickening and thinning of the layer. He found that the amplitude of the peak response increased in proportion to the freestream turbulence and grew in the streamwise direction in proportion with the boundary-layer thickness. These low-frequency oscillations are generally referred to as *Klebanoff* modes.

The works of Klebanoff [54] and Kendall [56, 57, 58, 59, 53] have identified three distinct motions generated within the boundary layer as a result of freestream turbulence (see also Westin *et al.* [60], and Boiko *et al.* [61]). The first is the Klebanoff mode mentioned above which is characterized by long, streaky perturbations. A mechanism for the generation of Klebanoff modes is given by Goldstein & Wundrow [63] and later validated in a recent experiment by Ustinov *et al.* [64] in their linear regime. The presence of vertical vorticity (e.g. from immeasurably small spanwise nonuniformities in the incoming flow as discussed by Watmuff [65]) can result in the stretching or wrapping of vortex lines around the leading edge of the model and lead to the streamwise vorticity on the model surface. The streamwise vorticity produces streamwise velocity perturbations within the boundary layer that can lead to the experimentally observed Klebanoff modes [63]. The second is an outer-layer fluctuation (energy peaks near the edge of the boundary layer) dominated by frequencies in the unstable T-S band. The profile shapes are unlike those of the T-S eigenfunction. Correlation measurements by

Kendall indicated propagation speeds of these T-S frequency fluctuations are equal to the stream velocity. These peak fluctuations grow very slowly with downstream distance. The third motion is the well-known T-S mode which grows at much larger rates. T-S modes were only observed by Klebanoff [54] and Boiko et al. [61] by intentionally exciting the modes with use of a two-dimensional roughness element and vibrating ribbon, respectively. Boiko et al. found on average that the T-S waves grew less rapidly with freestream turbulence than without. In the experiments of Kendall, the T-S waves appeared in the form of packets. He found a nonlinear response of the T-S amplitude with freestream turbulence. He raised the possibility of distributed receptivity along the length of the plate which was consistent with various correlation-based measurements. Kendall [59] observed larger receptivity to freestream turbulence for a blunter leading edge than for a slender one. Confusion still exists among the interpretations of results from different receptivity experiments excited by freestream turbulence.

Localized receptivity

Receptivity of laminar boundary layers in the presence of three-dimensional surface roughness will not be presented here. The reader can refer to a recent review paper by Kachanov [35].

Acoustic excitation: Numerous experiments have been conducted on laminar boundary layers over flat plates to examine the effects of two-dimensional surface roughness in conjunction with freestream sound on the generation of T-S waves. These include, for example, experiments by Aizin & Polyakov [66], Saric et al. [67, 68, 48], Zhou et al. [69], Kosorygin et al. [70], Breuer et al. [71], and Kobayashi et al. [72, 73]. Numerical results by Bodonyi et al. [74] and Crouch [75] along with some of the aforementioned references provide essential theoretical results for comparison with experiments.

The experiment by Aizin & Polyakov [66] (see review by Nishioka & Morkovin [31]) was conducted before any formal receptivity theory (class II) was available (Gold-

stein [21] and Ruban [23]). Aizin & Polyakov used extra-thin mylar strips with three different small roughness heights such that the strips were immersed deep in the linear stress region of the Blasius profile. The measured T-S amplitudes were found to respond linearly with acoustic (single-mode) excitation level. Three strip widths were considered, namely $0.24\lambda_{ts}$, $0.5\lambda_{ts}$, and λ_{ts}, where λ_{ts} denotes the wavelength of the T-S wave. They found a maximum response for a strip width of $0.5\lambda_{ts}$ which was later verified by theory. However, the nonzero receptivity value obtained for a strip width of λ_{ts} was inconsistent with theory. The effect of roughness height on the linearity of the receptivity mechanism was studied by Saric et al. [67, 68]. A two-dimensional roughness with a width of $\lambda_{ts}/2$ was placed at Branch I. Their T-S wave measurements demonstrated a high degree of two-dimensionality. The amplitude of the T-S wave was found to respond linearly for roughness heights in the range 40 - $120\mu m$ in agreement with theory by Goldstein [21]. The experiments also seem to confirm the nonlinear triple-deck analysis by Bodonyi et al. [74] which predicts the onset of nonlinear effects to occur when the roughness height exceeds the height of the viscous lower deck.

The effect of broadband sound on receptivity in the presence of a two-dimensional roughness was first examined by Breuer et al. [71] (see also Grimaldi [76] and Gunnarsson & Ullmar [77]) and later by Saric & White [48]. Breuer et al. examined receptivity for the naturally occurring acoustic environment in their facility which demonstrated a large spectral peak at the blade-passage frequency of the drive fan. Using one, three, or five roughness strips placed around Branch I and tuned to the blade-passage frequency, they were able to vary the strip spacings and study the response of the T-S amplitude, which is commonly referred to as *detuning* (the desynchronization of the wall wavelength and instability wavelength). They confirmed a maximum T-S response with zero detuning, i.e. $\alpha_w = \alpha_{ts}$, in agreement with theory. A linear T-S response was also observed with roughness height and the number roughness strips. These results are in general agreement with results obtained for single-mode forcing. This is not very surprising since the dominant and phase-locked nature of the acoustic energy at the blade-passage frequency is akin to single-mode forcing. The follow-up

experiment by Saric & White [48] from the earlier studies [67, 68] investigated the effects of single-mode versus broadband (band-limited white noise) acoustic excitation. No essential differences were observed between single-mode and broadband excitation. For a given sound pressure level, more energy resides in the single mode than for the same frequency in the broadband forcing. The results suggested that the T-S response was still triggered by the amplitude of the individual modes which is in general agreement with the findings of Breuer et al. [71].

The receptivity of a laminar boundary layer on a flat plate was experimentally studied in the presence of a two-dimensional roughness and freestream sound by Kosorygin et al. [70]. They studied the effects of constructive-destructive interference of independent T-S waves generated by multiple localized sources, namely the leading edge and two-dimensional roughness. A coupling between the two T-S waves occurred in the vicinity of the roughness and linear superposition applied since the disturbance amplitudes were typically small. They observed that T-S wave amplitudes with roughness can be less than that for the case without roughness. Consequently, the experimental estimations of receptivity will be subject to small variations with shifts in the source locations on the $O(\lambda_{ts}/2)$. The experiments of Kobayashi et al. [72, 73] were similar in that they looked at the interference between two T-S waves generated by two two-dimensional roughness strips. Here, the leading-edge receptivity component was made negligible by the use of a 36 : 1 modified-super-ellipse leading edge. They were able to show significant increases or decreases in the T-S amplitudes at downstream distances when the spacing between the leading edges of the two roughness elements was λ_{ts} and $1.5\lambda_{ts}$, respectively. In other words, maximum constructive interference occurred for spacings equal to integer multiples of λ_{ts} and maximum destructive interference for spacings equal to $0.5, 1.5, \ldots$ multiples of λ_{ts}. This phenomenon is easily explained by linear superposition of the generated T-S waves. They also investigated the effects of a single two-dimensional roughness. They found that the velocity fluctuations at the leading and trailing edges of the roughness element were $180°$ out of phase, thus explaining (experimentally) the result that a roughness of width $\lambda_{ts}/2$ gives the optimum T-S response for an isolated

two-dimensional roughness.

The experiments discussed above for localized receptivity were all performed with the acoustic source located far upstream of the model and pointing in the downstream direction. A downstream-traveling (grazing) acoustic wave provides maximum receptivity as opposed to the minimum response for normal incidence. An experiment by Zhou *et al.* [69] investigated the effects of acoustic-wave incidence angle on receptivity in the presence of a two-dimensional roughness. Their results were in good agreement with theory as given by Choudhari & Kerschen [78]. They also investigated receptivity for roughness inclination angles between 0° (two-dimensional roughness) and 45° (oblique roughness). Spanwise cross-correlations between two closely spaced hot-wire probes were used to measure the angle of the generated boundary-layer disturbance wave. They found good agreement between the measured wave oblique angle and roughness oblique angle for angles less than 35°. They inferred from their measurements at a fixed streamwise location that receptivity was reduced with increased oblique angle. They did not however consider the reduced linear growth rates associated with increased obliqueness from LST. Calculations done by Crouch & Bertolotti [79] for non-localized receptivity indicated increased receptivity with increased obliqueness.

Receptivity of a laminar boundary layer on a flat plate to acoustic excitation was examined in the presence of a narrow suction slot and porous surface by Wlezien *et al.* [80, 44]. The detection of acoustic receptivity at the porous strips was found to be sensitive to the shape of the plate leading edge and the residual T-S waves persisting from that region. Evidence of a suction-surface receptivity mechanism by acoustic scattering was observed supporting the theoretical findings of Heinrich *et al.* [28]. The receptivity mechanism was activated with no net flow through the porous surface and when the boundary layer was slightly stabilized by weak suction.

Freestream turbulence excitation: The receptivity of a laminar flat-plate boundary layer to convected gust in the presence of a forward-facing step was experimentally investigated by Parekh *et al.* [43]. An array of oscillating ribbons produced a vortical

disturbance in the form of periodic convected gust. No receptivity was measured for the interaction of the convected gust with the forward-facing step.

Non-localized receptivity

The results presented here are for non-localized receptivity with a known discrete wavenumber spectrum (e.g. surface waviness). Receptivity in the presence of distributed roughness will not be discussed (see papers by Reshotko [81] and Corke *et al.* [82]).

Acoustic excitation: The only experimental study to the author's knowledge that examined the effects of acoustic receptivity on a laminar flat-plate boundary layer with wall waviness was conducted by Wiegel & Wlezien [83] (see also Wiegel [84]). Receptivity calculations in the presence of wavy surfaces have been performed by Zavol'skii *et al.* [22], Crouch *et al.* [85, 79] and Choudhari [24]. Wiegel & Wlezien used an array of two-dimensional strips to simulate continuous wall waviness. A downstream-traveling sound field was generated in the freestream to interact with the wall waviness. They showed by successively adding additional strips, thereby increasing the number of wall wavelengths, that an effectively infinite wavy wall can be simulated with a finite number of strips in a small region surrounding Branch I in agreement with Choudhari's [24] findings. They also demonstrated an $O(10)$ increase for non-localized receptivity versus localized receptivity in support of receptivity calculations. Detuning was investigated by changing the freestream velocity while maintaining a constant forcing frequency, f, which resulted in a shift of the nondimensional frequency F ($= 2\pi f\nu/U_\infty^2$). Strong detuning was verified indicating strong receptivity in a relatively narrow band where there was a near match between α_w and α_{ts}. Their results were shown to match the trends as well as absolute amplitudes predicted by theory [85, 24].

Freestream turbulence excitation: Experiments were conducted by Dietz [86, 87] on a laminar boundary layer over a flat plate with a 58 : 1 elliptic leading edge.

He investigated receptivity to freestream vortical disturbances in the presence of two-dimensional roughness strips of various numbers. Dietz's results with both localized and non-localized receptivity sites are discussed together here for continuity. The convected disturbance was generated by a vibrating ribbon located upstream and aligned with the model leading edge. Three types of ribbon forcing were considered – single-frequency waves, pulses, and random noise. He measured the receptivity to broadband transient convected disturbances (using a single roughness strip) as a first step towards validating the use of single-frequency receptivity theories with real-world disturbances. The receptivity was shown to be the same for the three forcing types, demonstrating that the receptivity to a broadband disturbance may be modeled as the linear superposition of that caused by discrete frequencies. Subsequent measurements using a single-frequency wave and an array of roughness strips were conducted. He found that the response of the boundary layer to the convected disturbances was confined to the outer portion of the layer with the streamwise velocity fluctuations being rapidly damped towards the wall. An outer-layer interaction between the convected disturbance and the short-scale mean-flow distortion excited measurable T-S waves. The boundary-layer T-S response with a single roughness element was found to be linear for forcing amplitudes of the convected gust up to 1% of the freestream velocity. He also investigated the T-S response for various roughness heights with a single roughness element. His results were similar to the experimental results obtained for acoustic receptivity by Saric et $al.$ [67] and Zhou et $al.$ [69] and calculations for acoustic receptivity by Bodonyi et $al.$ [74]. By successively adding additional strips, Dietz observed an increase in receptivity with increasing number of roughness elements until an asymptotic limit was evident as was done by Wiegel & Wlezien [83] for acoustic receptivity. He also examined detuning by varying the nondimensional frequency, F, and found that receptivity was highly tuned to the resonance frequency. These results show similar trends to those obtained for acoustic receptivity over a wavy wall by Wiegel & Wlezien [83] and theoretical calculations [24, 79].

1.1.4 Oblique transition

Before embarking on the so called *oblique* transition, a brief discussion of the various paths to laminar-to-turbulent transition on flat-plate boundary layers is in order. It has long been recognized that the occurrence of three-dimensional disturbances (secondary instability) is necessary for the laminar-to-turbulent transition process (see for example Klebanoff *et al.* [6, 7]). The breakdown scenario observed by Klebanoff *et al.* is referred to as fundamental or K-type breakdown. K-type breakdown begins with the amplification of initially two-dimensional T-S waves. As the T-S waves exceed a threshold value of typically 1% of the freestream velocity, three-dimensional structures evolve with spanwise periodicity of alternating *peaks* and *valleys*, which correspond to regions of maximum and minimum velocity disturbance levels, respectively. Smoke visualization images of K-type breakdown are presented, for example, by Saric *et al.* [88, 89] and Thomas [90]. The appearance of **aligned** hair-pin or Λ-shaped vortices corresponding to peaks and valleys are evident in the smoke-flow visualizations, often called peak-valley splitting. The streamwise disturbance growth rates at peak locations are larger than those of the primary T-S instability wave. A system of streamwise vortices appear at the same time as the peak-valley splitting. Low-speed streaks develop due to the *lift-up* effect (see Landahl [91]) which leads to the formation of high-shear layers with highly inflectional instantaneous profiles (which are generally very unstable) at the peak locations. Small-scale instabilities with high-frequency velocity oscillations ("spikes") develop from the shear layers initiating the formation of turbulent spots and ultimately turbulence. The appearance of higher harmonics in the fluctuating velocity spectrum become evident when spikes are observed. It is interesting to note that only a few T-S wavelengths separate the first appearance of three-dimensional structures and transition. Using Floquet theory of secondary instability, Herbert [92] was able to explain essential qualitative and quantitative aspects of the the early stages of K-type breakdown. Herbert's results show that for large initial two-dimensional T-S amplitudes relative to random background disturbances, primary resonance occurs leading to K-type breakdown.

A different route to transition, subharmonic breakdown, was first observed Knapp & Roache [93] on an ogive cylinder and was characterized by a **staggered** peak-valley structure (see photographs of smoke-flow visualization [88, 89, 90]). Self-excited subharmonic spectral energy (three-dimensional excitation derived from background disturbance environment) was first observed on a flat-plate boundary layer by Kachanov *et al.* [94] and later by Saric *et al.* [88, 89], Kachanov *et al.* [95], and Corke & Mangano [96] for self-excited and/or controlled resonance. A long fetch (streamwise amplification distance) is generally required to synchronize and entrain the subharmonic from the background disturbance environment [94, 88, 89, 95]. Subharmonic secondary instabilities are initiated at disturbance amplitudes of less than 0.3% of the freestream velocity and occur at or downstream of Branch II. Subharmonic breakdown is characterized by small two-dimensional T-S amplitudes and produce either a C-type or H-type breakdown. The triad resonance model of Craik [97] for C-type breakdown postulates the existence of two oppositely-oriented oblique O-S modes that are phase locked to the primary two-dimensional T-S disturbance. He showed that a quadratic interaction between the oblique waves can produce a resonance with the primary wave. Resonance of Craik's triad causes a narrow peak of amplification at small spanwise wavenumbers for very small primary wave amplitudes, while the peak is absent for other conditions [92, 15]. For the more robust model of Herbert [15], subharmonic instability originates from Squire modes so that the H-type instability occurs as a parametric resonance. H-type is a more general type of subharmonic instability that occurs for a broadband of spanwise wavenumbers. Smaller spanwise wavelengths are associated with H-type breakdown as compared with C-type breakdown. Spikes are not observed in the subharmonic breakdown process and spectral broadening occurs more gradually than K-type through the interaction of low-frequency fluctuations, including the subharmonic, with the fundamental and higher-harmonic fluctuations. Computations done for Klebanoff's experiment predict H-type as the dominant mechanism for the experimental conditions which is in contrast with measurements. Singer *et al.* [98] showed for plane channel flow that introducing streamwise vortices into the flow can accelerate K-type instability leading to K-type breakdown in favor of H-type

41

breakdown.

The evolution of wavepackets in laminar boundary layers has been studied as a model of *natural* transition to turbulence since a wavepacket produces a broad spectrum of frequencies and spanwise wavenumbers (refer to Gaster & Grant [99]). The evolution of a localized disturbance in a laminar boundary layer from a low-amplitude wavepacket to the formation of a turbulent spot has been experimentally studied by Cohen *et al.* [100] and Breuer *et al.* [101]. In the linear stage of the wavepacket evolution, the wavenumber-frequency spectra indicated that most of the energy was concentrated in two-dimensional modes centered about a fundamental frequency corresponding to the most-amplified mode according to LST. As nonlinear effects evolve in the wavepacket, increased energy corresponding to oblique modes at a frequency one-half of the fundamental (subharmonic modes) were observed to be dominant in the wavenumber-frequency spectra. The spanwise wavenumber corresponding to these oblique modes suggested that the modes grew as a subharmonic resonance triad as described by Craik [97].

The transition scenarios discussed above all start with strong two-dimensional modes, but as the three-dimensional modes gain energy, transition advances rapidly. The distilling process of boundary layers has identified oblique modes as an essential ingredient for the onset of laminar breakdown. Recognizing that direct seeding of oblique modes may be very efficient, Schmid & Henningson [102], using direct numerical simulations (temporal) applied to a channel flow, investigated a transition mechanism involving a pair of oblique O-S modes $(f, \pm\beta)$ in the frequency/spanwise-wavenumber space, the so called *oblique* transition. They found that this transition scenario occurred at a much faster time scale than the one for secondary instability, assuming the same input disturbance energy for both scenarios. They also found that nonlinear interactions were mainly responsible for the initial energy transfer to other spanwise modes that then grew by linear mechanisms. The dominance of the linear transfer mechanism was reduced as transition was approached. Later, Joslin *et al.* [103] and Berlin *et al.* [104] applied spatial numerical simulations covering the transition process to a Blasius boundary layer. This transition scenario was conjectured as

a three stage process: (i) a nonlinear interaction of the primary disturbances ($f, \pm\beta$) to generate a streamwise vortex system ($0, 2\beta$), (ii) a transient growth region of low- and high-speed streaks produced by the vortex system, and (iii) ultimate breakdown of the streaks instigated by nonstationary disturbances due to secondary instability. Subcritical transition resulting from transient disturbance growth was found to be possible, thereby *bypassing* (see Morkovin [17]) the exponential amplification of T-S instabilities.

Elofsson & Alfredsson [105] were the first to verify oblique transition in a physical experiment. The experiments were conducted in a plane Poiseuille flow air channel in which oblique waves were generated by two vibrating ribbons, one on each wall. Other experiments were conducted to study the algebraic growth (see Landahl [106]) of the streaky structures and ultimate breakdown of the flow by direct generation of streaks. The origin of the streaks is not so important since all of these mechanisms generate streaks, some more efficiently than others depending on the initial conditions. Once the streaks are established, the mechanisms thereafter are the same. Elofsson *et al.* [107] experimentally studied in a plane Poiseuille flow the development and stability of streamwise streaks generated by continuous suction through small wall slots. They found that if the streak amplitude exceeded a threshold value, secondary instability ensued in the form of traveling waves that give rise to high rms (root-mean-square) fluctuating velocities in the region of large spanwise mean-flow gradients. Similar findings were observed by Bakchinov *et al.* [108] in a flat plate boundary layer modulated by stationary streamwise vortices generated by means of roughness elements arranged in a regular spanwise array. Recently, Wiegel & Fisher [109, 110] used non-intrusive optical techniques to study the structure of a Blasius boundary layer undergoing transition. They utilized controlled input disturbances in the form of periodic pressure oscillations through surface slots to control initial amplitudes of possible two-dimensional and oblique disturbances. By adjusting the relative amplitudes of the disturbances [110], they were able to visualize the following transition types: fundamental (K-type), subharmonic (C-type and H-type), and oblique type transition. For the oblique transition scenario, streamwise streaky structures with

small α were observed which ultimately resulted in breakdown to turbulence.

1.2 Objectives

The objectives of this research are twofold. The first objective was to further understand the acoustic receptivity process for flow over wavy surfaces and to correlate theoretical results with experimental results. The approach taken was to experimentally investigate acoustic receptivity in the presence of distributed surface waviness and the subsequent boundary-layer disturbance evolution. Previous experimental acoustic receptivity data [83] in the presence of two-dimensional (2-D) surface waviness demonstrated excellent agreement between experimental and theoretical [85, 24] receptivity coefficients. In the presence of oblique surface waviness, previous experimental receptivity data do not exist and inference made from previous experimental results [69] for a localized oblique roughness strip contradict theoretical findings. The current experimental study with 2-D waviness was conducted to (i) validate the current approach with respect to previous experimental data and theoretical results and (ii) extend the measurements into regions of nonlinear T-S wave development. The measurements were then extended to include, for the first time, experimental data obtained with oblique surface waviness for comparison with theoretical results [79]. The second objective was to improve the current knowledge of the oblique transition process and to provide a potential data base for comparison with theory and/or numerical simulations. Oblique transition was experimentally investigated by exciting a pair of oppositely-oriented oblique Orr-Sommerfeld modes. Documentation of the subsequent development of the broadband boundary-layer disturbance evolution for various forcing combinations ($\epsilon \cdot \Delta h$) was acquired. The modal velocities, i.e. for a given frequency and spanwise wavenumber, was mapped along the streamwise direction for the primary modes and higher-order modes resulting from nonlinear interactions. The experimental results were compared qualitatively and quantitatively, when possible, with theoretical and numerical simulation results when available. The complete experimental data set will hopefully provide a data base for verification of

different theoretical models and/or numerical simulations, both linear and nonlinear, and improve the current understanding of laminar-to-turbulent transition physics.

The experimental study was conducted for a Blasius boundary layer over a flat plate. The effect of the forcing combination, roughness height and acoustic forcing level, on the boundary-layer instability initiation and subsequent development was examined. Receptivity/stability experiments are very sensitive to the state of the mean flow and environmental disturbances. As a result, extreme care was taken to document the flow and environmental conditions to avoid ambiguous results as discussed by Nishioka & Morkovin [31] and Saric [111]. A nominal zero-pressure gradient boundary layer was established as the base flow. A planar downstream-traveling acoustic wave provided the freestream excitation. Small-amplitude surface roughness was produced using a photolithographic process to generate the roughness patterns which insured a high degree of spatial accuracy (or well-defined wavenumber spectrum).

1.3   Road map

The set-up, procedure, and results of this experimental study are presented in several chapters and appendices in this document. The experimental set-up and instrumentation used for data acquisition are presented in Chapter 2. A description which includes the experimental overview and general measurement procedures is given in Chapter 3. Results are presented in Chapter 4 which document the freestream environment and mean boundary-layer flow. Receptivity results and subsequent boundary-layer disturbance evolution for 2-D and oblique instability waves are discussed in Chapters 5 and 6, respectively. Results and discussion of oblique transition are presented in Chapter 7. This is followed with concluding remarks in Chapter 8. A detailed uncertainty analysis of the experimental results is given in Appendix A. In Appendix B, a discussion of dynamic pressure measurements obtained in the facility test section is presented.

1.4 Summary of contributions

In this section, a brief summary of the contributions made in the current study are listed. To summarize, we:

- introduced a *clean* approach for exciting 2-D, oblique, and oppositely-oriented oblique boundary-layer instability waves.

- produced a mean boundary layer that compared well to the theoretical Blasius boundary layer.

- measured acoustic receptivity data for 2-D surface waviness which are in excellent agreement with existing data and theoretical results. Good agreement was observed between experimental and LST eigenfunctions.

- produced unique acoustic receptivity data for oblique surface waviness which are in good agreement with theoretical results. Results confirm that receptivity increases with wave obliqueness.

- acquired boundary-layer disturbance evolution throughout the transitional region for a boundary layer excited by two oppositely-oriented oblique modes.

  - Modal velocities are in good qualitative agreement with numerical simulation results.

  - Strong secondary instability appears to be driven by spanwise U gradients, not wall-normal inflectional profiles.

  - Growth rates of streaky structures are believed to be enhanced by a nonlinear (feedback) interaction of two nonstationary boundary-layer disturbance modes.

Chapter 2

Experimental Hardware

2.1 Wind tunnel facility

The experiment was conducted in the 2 Foot by 3 Foot Low-Speed Wind Tunnel located at NASA Langley Research Center. Figure 2-1 shows a schematic of the top and side views of the wind tunnel. The test section is $0.91m$ wide by $0.61m$ high by $6.1m$ long. The tunnel is a closed-loop type and is driven by a vane-axial fan which is powered by 30 horsepower DC motor. The contraction ratio of the tunnel is $10:1$. The turbulence-reduction devices upstream of the contraction consist of a $10cm$-thick aluminum honeycomb with $9.5mm$ cells and four stainless-steel screens, two 24×24 mesh and two 40×40 mesh screens. Speeds of approximately $45m/s$ are attainable in the test section. Measured turbulence intensities, u/U_∞, on the order of 0.1% $(0.1 < f < 400Hz)$ were obtained throughout the speed range.

The test-section floor and ceiling are adjustable to achieve a desired streamwise pressure gradient. The floor and ceiling adjustment stations are separated $0.61m$ in the streamwise direction. The ceiling is equipped with a single row of $0.5mm$-diameter pressure taps every $15.24cm$ along the entire test section length. The row of pressure taps are located $15.24cm$ from the centerline.

Two motorized traverse stages, one with streamwise travel of $2.1m$ and the other with vertical travel of $150mm$, are located just above the test section ceiling (see Figure 2-1). The accuracies of the streamwise (x) and vertical (y) traverse stages are

47
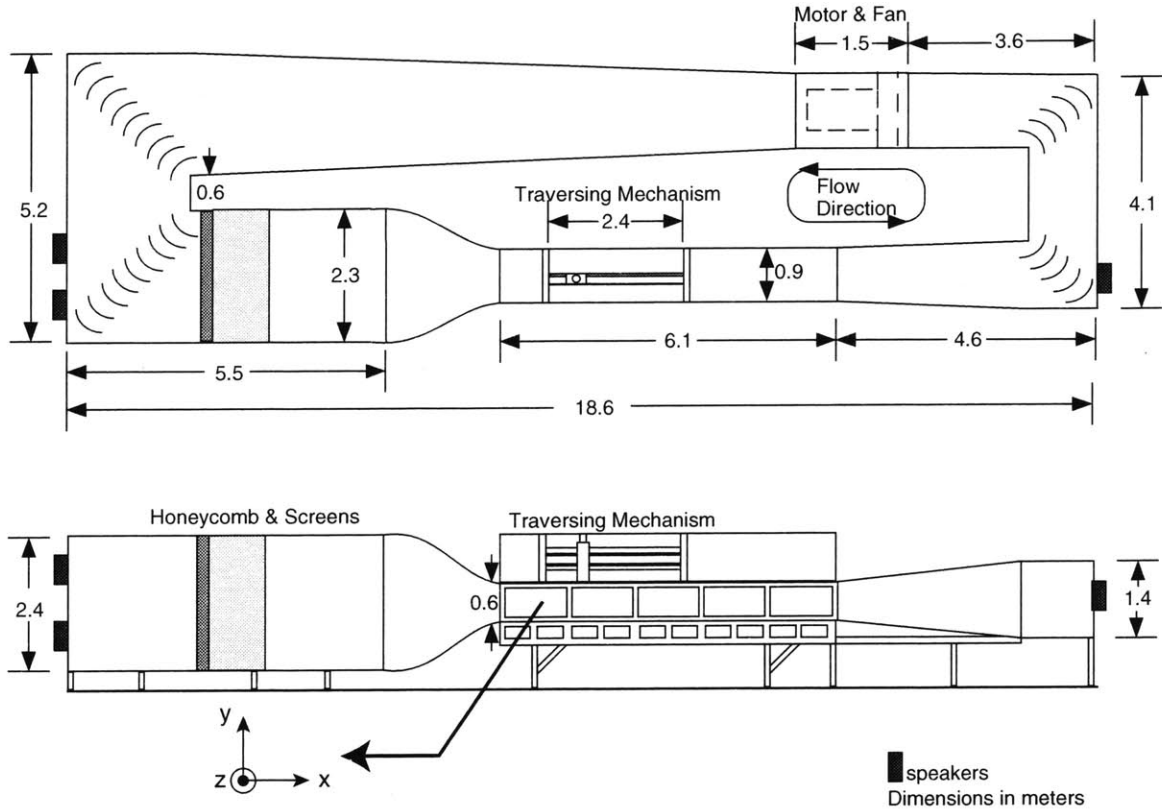
Figure 2-1: Top and side views of wind tunnel.

$\pm166\mu m/m$ and $\pm30\mu m/m$, respectively. The streamwise coordinate, x, and wall-normal coordinate, y, were measured from the leading edge and upper surface of the model, respectively. A 3.8-cm streamwise slot along the centerline of the tunnel ceiling is provided to accommodate a probe support for two-dimensional traverse motion. The slot is covered with a rectangular wool felt strip on both sides of the outer surface to minimize air inflow/outflow from the test section. Both traverse stages employ Aerotech stepper motors that are controlled using a Unidex 12 motion controller. The system provides a linear x resolution of $25.4\mu m$ and a linear y resolution of $0.5\mu m$. For configurations where spanwise traverses were necessary, a third traverse component with a travel of $11.43cm$ was installed in the tunnel test section as shown in Figure 2-2. Note that the 12-$inch$ scale in the figure was included only as a size reference. A Velmex spanwise (z) traverse stage, MicoMO DC servor-motor, encoder, gearhead and coupler were all housed in the stage support indicated in the figure. The spanwise coordinate z was measured from the centerline of the test section. Streamlined cross

48
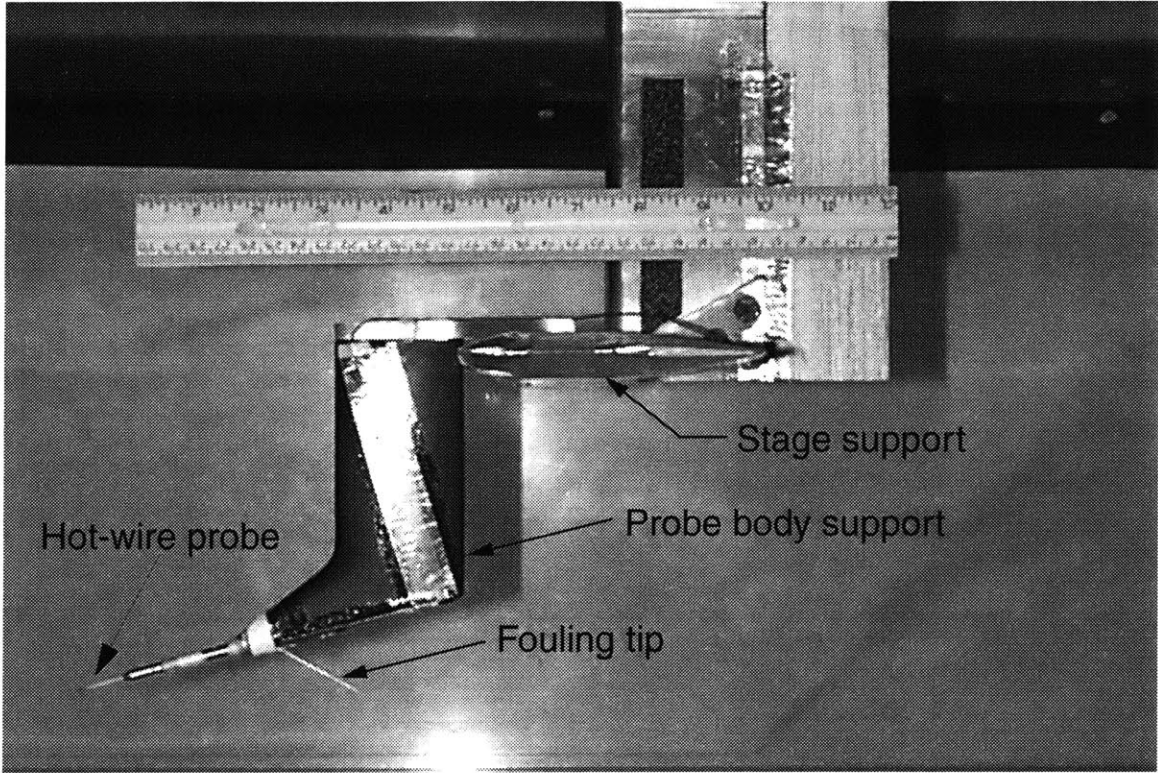
Figure 2-2: End view of spanwise traverse.

sections of the stage support and probe holder support were selected to minimize flow interference. The maximum thickness-to-chord ratios of the stage support and probe holder support are 16% and 15%. The Unidex 12 controller was also used to control the spanwise motion. The accuracy and linear resolution of the spanwise component are $\pm 125 \mu m/m$ and $0.1 \mu m$, respectively.

2.2 Flat plate model

The model tested was a 12.7-mm-thick flat aluminum jig plate. A sketch of the model along with relevant dimensions is shown in Figure 2-3. The model was 90.8cm wide by 262cm long and had a 24 : 1 elliptical leading edge. Because of the potential sensitivity of the receptivity and stability characteristics to surface roughness, the upper surface (measurement side) of the model was polished to a 0.2-μm rms surface finish. The boundary layer on the lower surface of the model was tripped using sandpaper grit to establish turbulent flow on that surface. A flap was hinged to the

49
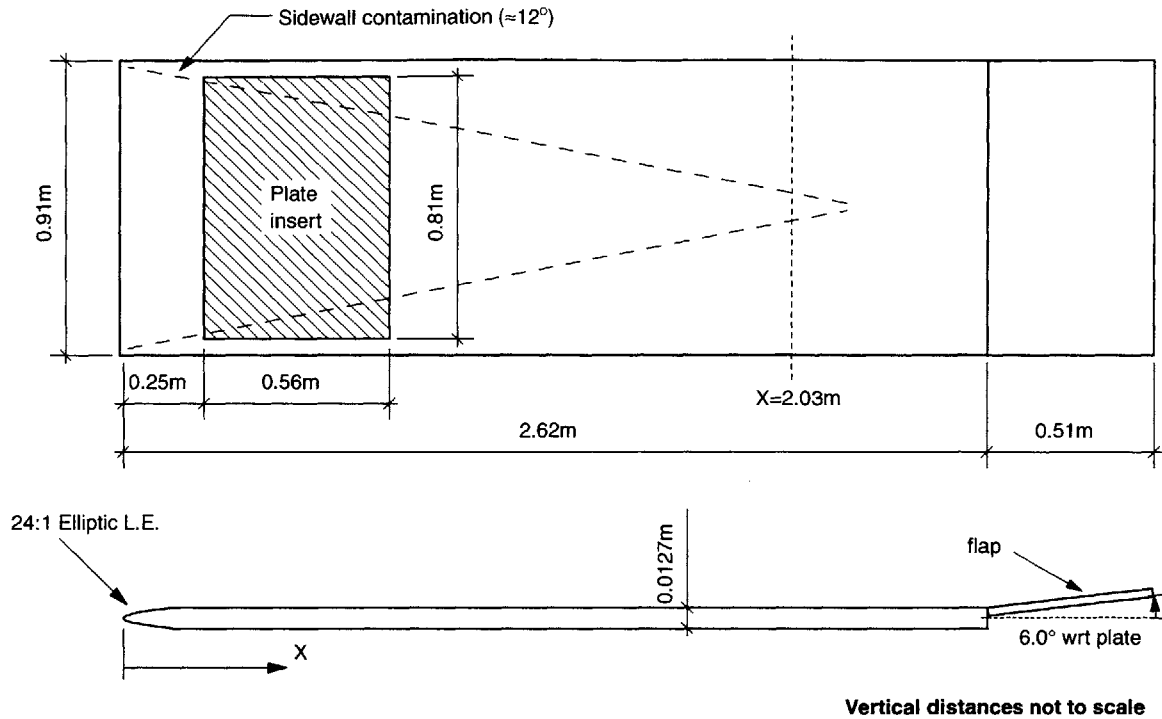
Figure 2-3: Top and side views of flat plate model.

trailing edge of the model to control the location of the flow attachment line at the model leading edge. The model was installed such that its leading edge was located $1.21m$ from the test section entrance and approximately $22cm$ above the tunnel floor. The flat plate was leveled and the flap was inclined at 6° with respect to the plate.

The plate was equipped with a rectangular hole located $24.6cm$ from the model leading edge for the installation/removal of plate inserts. The inserts were $80.6cm$ wide by 55.9 cm long and were also made from aluminum. Five inserts were available for the test. One was used as the baseline (smooth sample) and four were used to mount various samples of receptivity sites. Both the model and inserts were beveled at 45° so that a "V" groove existed around the perimeter of each insert when installed. This alleviated having abrupt steps at the model-insert junctures. The groove has a width of $2.54mm$ and a depth of $1.27mm$. The ability to adjust the insert height was done using set screws on the underside of the model. After careful alignment of the insert, the groove was filled with modeling compound and carefully sculptured to give a smooth transition between the model and insert.

50

2.3 Instrumentation

In this section a brief description of instrumentation used for data acquisition are addressed for completeness. A Power Macintosh 8100/80AV and a Macintosh Quadra 700 were used to communicate with the following instrumentation. The data acquisition routines were written using LabVIEW graphical programming. Refer to Appendix A for details of error analysis where applicable.

A Hewlett-Packard (HP) model E3631A DC power supply was used to control the tunnel speed via the computer. The tunnel temperature and pressures were closely monitored throughout the tests. A General Eastern model 800LC indicator was used to monitor the relative humidity and temperature in the test section. The temperature/humidity indicator uses a bulk resistance type polymer humidity sensor for relative humidity detection and a 100 Ohm platinum resistance thermometer for temperature measurement. Mean static pressures on the test section ceiling were measured using a Pressure System PSI8400 measurement system. A 16-bit scanner digitizer unit and two 32-port $10''$ H_2O differential pressure modules were used as part of the system. Two Datametrics Barocell 10-$Torr$ differential pressure transducers monitored the mean pressures at the test-section entrance and calibration port. The mean absolute pressure in the settling chamber was measured using a 137.9-kN/m^2 Mensor 15000 digital pressure gauge.

The controlled acoustic levels were monitored by a Larson-Davis model 2530 precision condensor microphone which was flush mounted on the test section sidewall. This microphone was connected to a Larson-Davis model 910B preamplifier and model 2200C power supply. Dynamic pressure measurements were also acquired on the test section sidewall using Endevco pressure transducers (models 8506B-2 and 8507C-2) to monitor the wind tunnel disturbance environment as described in Appendix B. A universal amplifier model 7600A by Dynamics Electronic Products was used for signal conditioning.

Hot-wire measurements were obtained using a Dantec Streamline Unit with a constant temperature anemometer module 90C10. Single wire Dantec probes model

55P11 were utilized for all measurements. The sensors were made of $5\mu m$-diameter, platinum-plated tungsten wires with a length-to-diameter ratio of 250. The signal conditioners internal to the anemometer were turned off. Stanford Research Systems model SR650 band-pass filters were used for filtering and amplifying the anemometer output.

For computer retrieval, analog-to-digital (A/D) conversions were done for all transducer measurements that did not provide digital outputs. The mean A/D conversions were done using a 16-bit VXI model E1413B card manufactured by HP. Signal conditioners installed internal to the card made it possible to low-pass filter and adjust the gain for maximum utilization of the A/D processor dynamic range. The high-speed A/D conversions were done using an IOtech ADC488/8SA 16-bit converter with a BNC16 box. A Stanford Research Systems model SR830 DSP lock-in amplifier was used to acquire phase-locked amplitude and relative phase information with respect to a reference signal (TTL output of universal source).

2.4 Test configuration

The wind tunnel, model, and instrumentation used to conduct this experiment were discussed in the previous section. Two factors necessary for receptivity are some form of local streamwise inhomogeneity in the mean flow and an unsteady perturbation field. The surface roughness and acoustic excitation used to facilitate these factors will be discussed.

2.4.1 Surface roughness

In previous experiments, receptivity sites were usually created by applying tape or some other adhesive material to the surface of the model. For the case of non-localized receptivity, this is a very tedious process. Slight misalignment (angular and/or spatial) of the tape can affect the wavenumber spectrum of the roughness. Nonuniformities due to air pockets, adhesive thickness, and application technique may also present problems. For cases where surface roughnesses intersect each other,

it becomes increasingly more difficult since extreme care must be taken to avoid overlapping of the tape in order to preserve the roughness height Δh. For the above reasons, an alternate approach for generating the surface roughness was considered.

Upon careful review, the decision was made to manufacture the receptivity sites with copper-plated circuit boards. The substrate material of the boards was FR-4 fiberglass sheets which is a fire-resistant NEMA grade G-10 phenolic material. The substrate thickness used was nominally $203\mu m$ or $254\mu m$ and the copper thickness ranged from $17.8\mu m$ to $71.1\mu m$. The patterns were generated using a photolithographic process where a high degree of spatial accuracy can be maintained. The spatial accuracy ranged from approximately $\pm25\mu m$ for a copper thickness of $17.8\mu m$ to $\pm100\mu m$ for a copper thickness of $71.1\mu m$. In this process a pattern can be transferred from a photomask to a material layer. First the copper was coated with a layer of light-sensitive material called photoresist. The photomask was then applied to the layer and the photoresist was then exposed to ultraviolet light through the photomask. The exposed regions were then insoluble in a developer solution. A pattern of photoresist was left wherever the mask was transparent. The board was next immersed in a solution of hydrofluoric acid which selectively attacked the copper and not the photoresist pattern or board substrate. The photoresist was then removed by another chemical treatment. This produced a two-layer pattern with the roughness height Δh being equal to the copper plating thickness.

Three types of patterns were considered as shown in Figure 2-4. In the figure, the shaded area represents copper and flow is from top to bottom. The first was a two-dimensional waviness pattern (2-D case) with the wavenumber vector parallel to the stream direction. The second was an oblique waviness pattern (oblique case) where the wavenumber vector makes an angle ψ_w with the stream direction. The third case consisted of two oppositely-oriented oblique waves with $\psi_w = \pm30°$ which will be referred to as the three-dimensional waviness pattern (3-D case). Highly localized disturbances are possible for both the oblique and 3-D roughness patterns as a result of the sharp steps formed by the copper strips at the leading and trailing edges of the samples. To mitigate this effect, the copper strips were feathered down
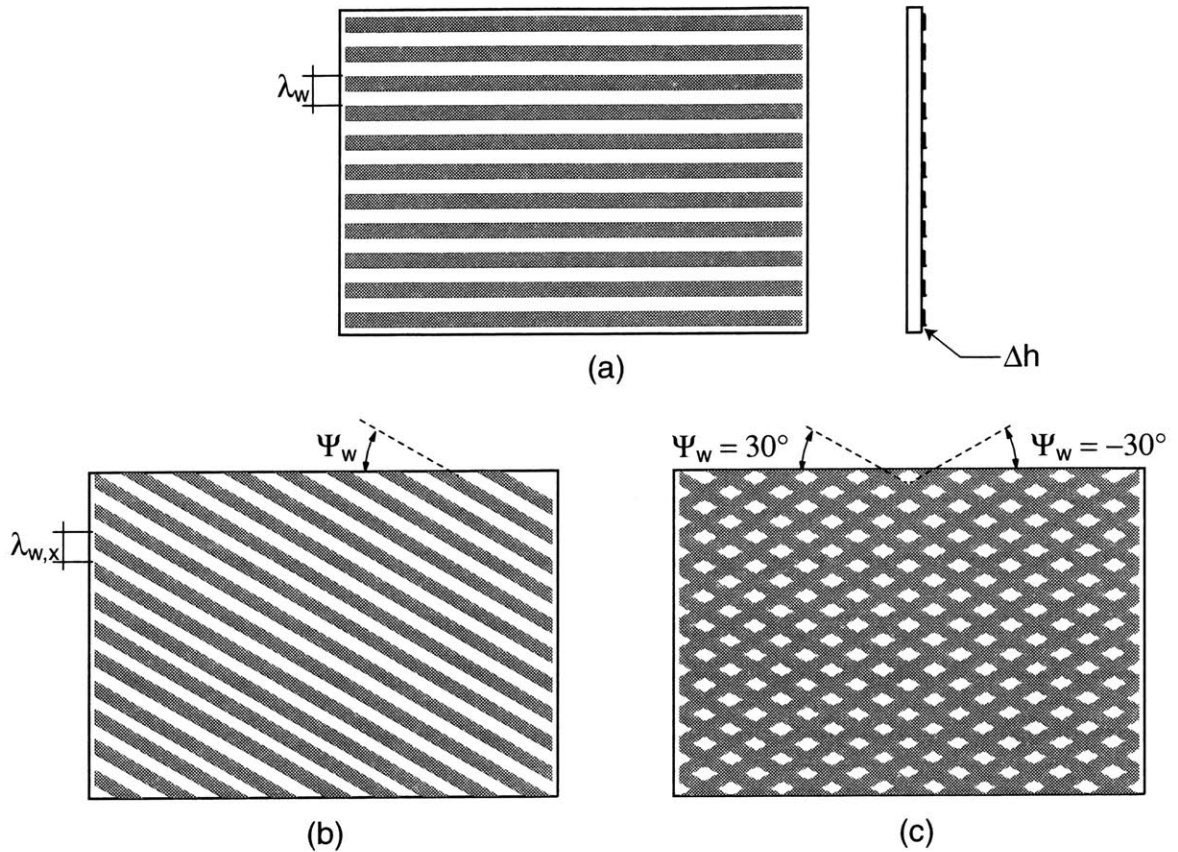
Figure 2-4: The three types of receptivity sites investigated: (a) two dimensional, (b) oblique, and (c) three dimensional. Flow is from top to bottom and shaded areas represent raised regions.

to the substrate material $6.4mm$ from both the leading and trailing edges of the samples. Different roughness heights were considered by using three types of boards with different copper plating thicknesses. The roughness patterns considered in this study are presented in Table 2.1.

2.4.2   Acoustic excitation

The tunnel was equipped with an array of five speakers (Rockford Fosgate RFP-1808 Punch Woofers) as indicated in Figure 2-1 for acoustic excitation. The speakers were located as shown in the figure to minimize unwanted flow disturbances in the test section. Four speakers were flush mounted on the wall upstream of the test section and the other was flush mounted on downstream wall. The speakers were mounted with the cones normal to the flow direction. The backplane of the speakers were

Sample #	Type	$\Delta h(\mu m)$	$\lambda_{w,x}(mm)$	$\psi_w(deg)$
1	2-D	17.8	50.25	0
2	2-D	35.6	50.25	0
3	2-D	71.1	50.25	0
4	2-D	35.6	58.88	0
5	2-D	35.6	53.34	0
6	2-D	35.6	50.80	0
7	2-D	35.6	49.53	0
8	2-D	35.6	48.26	0
9	2-D	35.6	45.72	0
10	oblique	35.6	50.75	15
11	oblique	35.6	52.36	30
12	oblique	35.6	55.48	45
13	oblique	35.6	56.67	32
14	oblique	35.6	54.50	31
15	oblique	35.6	50.27	29
16	oblique	35.6	48.22	28
17	3-D	17.8	52.36	±30
18	3-D	35.6	52.36	±30
19	3-D	71.1	52.36	±30

Table 2.1: Table of roughness samples tested.

sealed in boxes with bleed holes to equilibrate the mean pressures on both sides of the diaphragms. The speakers were 8-Ohm, 203.3-mm-diameter woofers with a frequency range of $30Hz$ to $500Hz$.

The source of the controlled acoustic field was generated by using both channels of a HP model 3245 dual-channel universal source. The universal source has a frequency resolution of $0.001Hz$, a frequency accuracy of ±50ppm and a phase offset resolution of $0.001deg$. The output signals from the source were amplified with a Gemini Triton SA-501 stereo power amplifier. One channel of the source was used to drive the four upstream speakers while the second channel was used for the one downstream speaker. The ability to control the absolute amplitude and relative phase between the two channels of the source made it possible to generate the required acoustic field in the test section.

Chapter 3

Experimental Procedure

3.1 Overview

In this chapter, the different experimental procedures used to produce the final experimental results are discussed. The experiment was conducted with a nominal freestream velocity and temperature of $U_\infty = 11.1 m/s$ and $T = 21°C$. An acoustic wave train was used to temporally excite the flow with frequency, f_o. A single hot-wire probe was utilized to measure the streamwise velocity component U which represents the bulk of the experimental data. Broadband and phase-locked velocity fluctuations were acquired. A cartoon showing the overall experimental setup is given in Figure 3-1. The mean tunnel properties (pressures, temperature and relative humidity) were measured and recorded at each data point.

Linear stability theory was employed to obtain the parameter space (e.g. location of Branch I, T-S wavelength λ_{ts}, frequency f, etc.) of the experiment. The dimensionless frequency of the T-S wave for all cases was $F = 2\pi f \nu/U_\infty^2 = 55 \times 10^{-6}$ which translates to physical forcing frequency of the acoustic field of $f_o = 71 Hz$. Figure 3-2 shows a plot of a neutral stability curve for a Blasius boundary layer with two-dimensional disturbances where the Reynolds number is denoted by R ($R = \sqrt{Re_x}$). The stable and unstable regions are indicated on the stability diagram. A line representing the current experimental frequency along with the roughness location and extent is shown in the figure. The wavenumber of the surface roughness, $k_w = 2\pi/\lambda_w$,
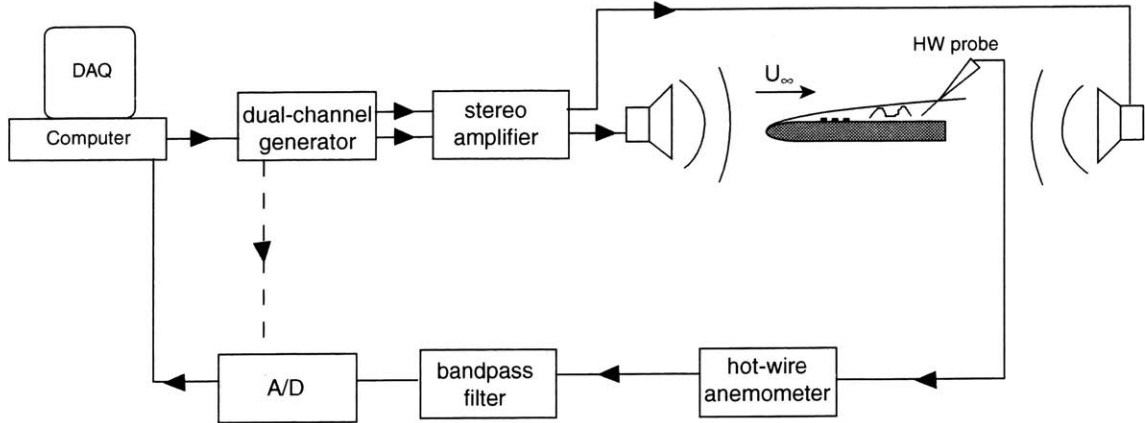
Figure 3-1: Schematic of experimental setup.
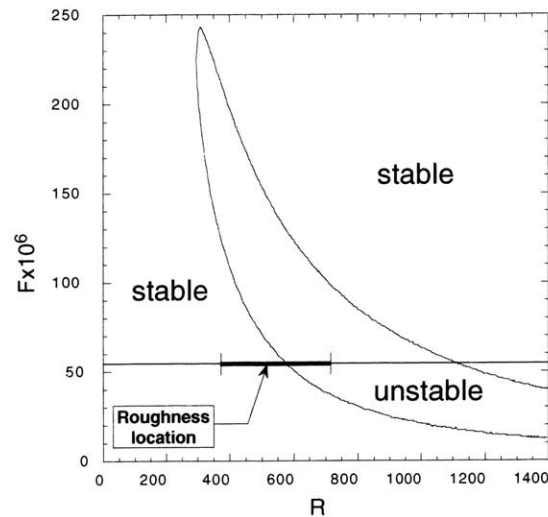
Figure 3-2: Neutral stability curve for a Blasius boundary layer with 2-D disturbances.

was selected such that it matched the T-S wavenumber, k_{ts}, at Branch I to provide a near-resonance condition. Three roughness heights, Δh, and three acoustic forcing levels, $\epsilon = u_{ac}/U_\infty$, were examined for the 2-D and 3-D patterns. The matrix configuration used to combine the roughness heights and forcing levels are given in Table 3.1. Detuning was examined for the 2-D and oblique roughness patterns. This was achieved by maintaining the same forcing frequency, $f_o = 71Hz$, and varying the streamwise wall roughness wavenumber, α_w. While changing the value of α_w for the oblique case, the spanwise wavenumber β_w remained unchanged. As a quick reference to aid the reader, Table 3.2 presents selected streamwise locations, x, and the

58

	Δh_1	$\Delta h_2 = 2\Delta h_1$	$\Delta h_3 = 4\Delta h_1$
ϵ_1	$\epsilon_1 \Delta h_1$	$2\epsilon_1 \Delta h_1$	$4\epsilon_1 \Delta h_1$
$\epsilon_2 \doteq 2\epsilon_1$	$2\epsilon_1 \Delta h_1$	$4\epsilon_1 \Delta h_1$	$8\epsilon_1 \Delta h_1$
$\epsilon_3 \doteq 4\epsilon_1$	$4\epsilon_1 \Delta h_1$	$8\epsilon_1 \Delta h_1$	$16\epsilon_1 \Delta h_1$

Table 3.1: Roughness heights and forcing levels examined ($\Delta h_1 = 17.8 \mu m$, $\epsilon_1 = 7.6 \times 10^{-5}$).

$x\{cm\}$	$x_v\{cm\}$	R
50.80	44.22	571
76.20	69.62	717
101.60	95.02	838
127.00	120.42	943
152.40	145.82	1038
177.80	171.22	1124
203.20	196.62	1205

Table 3.2: Tabulated data of streamwise distance from leading edge x and Reynolds number R. The streamwise distance x_v is measured from the virtual origin x_o (refer to Section 4.1). The Reynolds number is given by $R \approx 85.92 \cdot x_v^{1/2}$ where x_v is in units of centimeters.

corresponding nominal values of Reynolds number, R.

3.2 Pressure gradient assessment

The objective here was to obtain flow on the flat plate with zero streamwise pressure gradient, $dP/dx = 0$, (Blasius flow). This was a tedious process that involved several iterations. Before the model was installed, the floor and ceiling of the test section were leveled by making appropriate adjustments at each station (refer to Section 2.1). The model was then installed and leveled. Because of the sensitive nature of recep-

tivity/stability experiments, it was undesirable to have a separation bubble on the measurement (upper) surface of the model. The goal was to have flow attachment on the upper surface thereby eliminating the possibility of a separation bubble on the measurement surface. Two Preston tubes, one on the upper surface and the other on the lower surface, were carefully attached at the same span location to the model surface approximately $4mm$ downstream of the leading edge. The Preston tubes were connected to a differential pressure transducer to monitor the pressure difference between the upper and lower surfaces. The purpose for installing the Preston tubes was to monitor the flow attachment (stagnation) location near the leading edge. A zero differential pressure reading would indicate flow attachment on the leading edge of the model. A trailing edge flap on the model was used to effectively change the camber of the model and consequently the attachment location. The flap was rotated until the stagnation line was located on the upper surface. This corresponded to a positive pressure since the pressure on the upper surface was measured relative to the lower surface.

Pressures from the static pressure taps along the ceiling were measured using a PSI8400 measurement system. This was used as a first and expeditious attempt to measure dP/dx. The ceiling and/or floor were adjusted one station at a time followed by pressure measurements. After a satisfactory dP/dx was obtained, the final check was made to insure that the attachment line was still located on the upper surface. The Preston tubes were then removed and the area of the mounting locations were re-polished. Next, the mean streamwise velocity using a hot-wire probe was measured along the x direction at various wall-normal heights y. Minor adjustments were then made to the model pitch and/or ceiling location to improve dP/dx. The configuration with the best dU/dx just outside the boundary layer was selected as the final configuration. The velocity measurements were within 1% of the reference velocity U_∞ except for the first $20cm$ of the plate. As an ultimate check, detailed hot-wire boundary-layer profiles were obtained at various locations along the model. The shape factor, $H = \delta^*/\theta$, was computed by numerically integrating the measured velocity profiles and compared against the theoretical Blasius value of $H = 2.59$.

Results will be presented in the next chapter.

3.3   Acoustic field generation

The rms velocity fluctuations induced by the speakers, u_{ac}, were measured in the freestream with a hot-wire probe. This was done to evaluate the character of the acoustic field. Because of the orientation of the speakers, the acoustic waves setup in the test section were assumed to be planar provided f_o was below the cutoff frequency of first cross mode ($\approx 188Hz$). For plane wave excitation, the rms pressure fluctuation is given by

$$p_{ac} = \rho c u_{ac} \qquad (3.1)$$

where the acoustic speed in denoted by c ($c = 344m/s$ at test conditions). The pressure fluctuation can be normalized on a decibel scale using the customary definition of sound pressure level SPL as follows

$$SPL = 20 \cdot \log \left(\frac{p_{ac}}{20\mu Pa} \right). \qquad (3.2)$$

The aim here was to generate a downstream-traveling wave to avoid ambiguities with the selection of an appropriate acoustic forcing level and, in principle, to have an unambiguous shift in the resonant roughness wavenumber to account for finite acoustic speed (see discussion in Section 5.2). However, due to reflective boundaries in the acoustic path, it was not possible to achieve this scenario using one set of speakers, namely the upstream speakers (refer to Section 2.4.2). A standing wave pattern was inevitably generated in the test section using only the upstream speakers. The downstream speaker was then used the generate an out-of-phase upstream traveling acoustic wave with appropriate amplitude to cancel the upstream component due to the reflective boundaries as done by Wiegel & Wlezien [83] and later by Smith [112]. As an illustration, plots of the theoretical amplitude and phase distributions when a downstream- and upstream-traveling wave coexist in the test section are presented in Figure 3-3. Note the differences in rms amplitude and phase variation between a traveling wave ($\epsilon_{up}/\epsilon_{dn} = 0.0$), standing wave ($\epsilon_{up}/\epsilon_{dn} = 1.0$), and combination

61
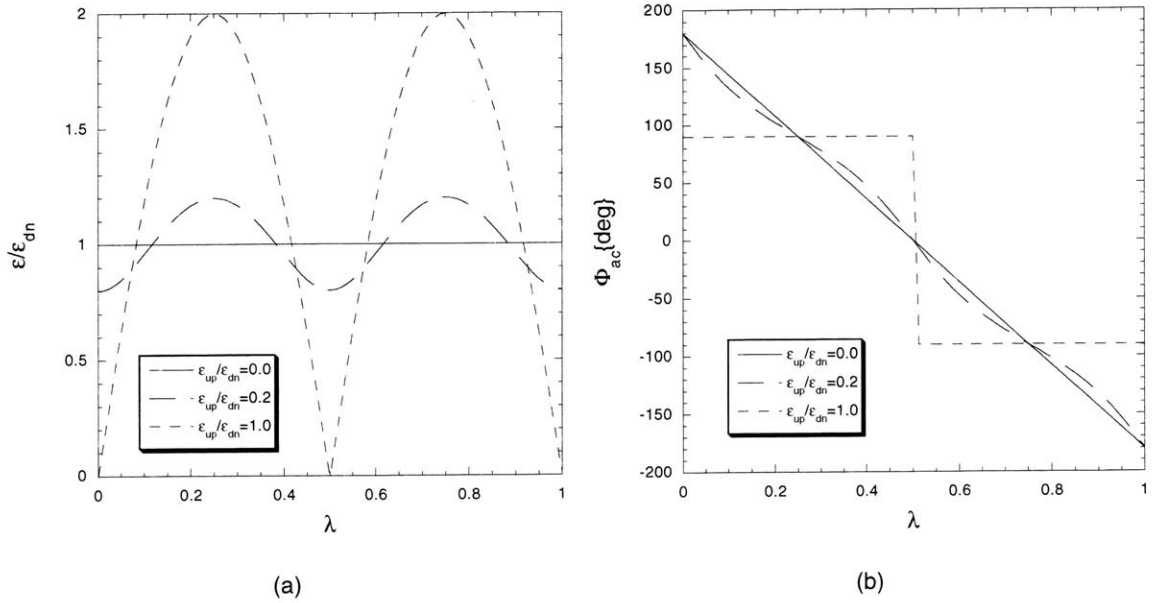
Figure 3-3: Examples of possible (a) amplitude and (b) phase distributions when a downstream- and upstream-traveling wave coexist in test section.

traveling-standing wave ($\epsilon_{up}/\epsilon_{dn} = 0.2$). Here the subscripts "up" and "dn" denote the upstream and downstream components, respectively. For the traveling wave, a constant rms amplitude and linear phase variation with downstream distance x is shown. For a standing wave (upstream- and downstream-traveling wave with equal amplitude), the rms amplitude has a sinusoidal character and the phase jumps 180° at each node. The combination wave amplitude is similar to the standing wave amplitude with an offset and the phase deviates from the linear phase behavior of the traveling wave.

Attempts were made to compute the downstream and upstream components of the wave system setup with only the upstream set of speakers energized. A spatial Fourier transform method [84] was inadequate because of the limited extent of the streamwise traverse ($2.1m$). For the transform method to be valid, measurements over at least one-half wavelength ($\lambda_{ac} = 4.84m$) were required. A two-point method was then developed to compute the downstream and upstream amplitudes of the acoustic wave system in the test section (A_{up} and A_{dn}, respectively). Assuming that the wave system can be decomposed into a single downstream and a single upstream

component, the field in the test section can be expressed using complex variable notation as

$$\hat{F}e^{i\omega t} = |A_{dn}|e^{i(\omega t - kx + \phi_{dn})} + |A_{up}|e^{i(\omega t + kx + \phi_{up})} \tag{3.3}$$

where ω, k, and ϕ denote radian frequency, wave number, and phase angle, respectively. The subscripts "dn" and "up" represent the downstream and upstream traveling wave components. By dropping $e^{i\omega t}$, Equation 3.3 can be rewritten as

$$\hat{F} = A_{dn}e^{-ikx} + A_{up}e^{ikx} \tag{3.4}$$

where $A_{dn} = |A_{dn}|e^{i\phi_{dn}}$ and $A_{up} = |A_{up}|e^{i\phi_{up}}$ are the two unknown complex variables. The complex acoustic field $\hat{F} = |\hat{F}|e^{i\phi_F}$ can then be measured at two streamwise locations and the Equation 3.4 solved for A_{dn} and A_{up}. The downstream speaker can then be set with an amplitude of $|A_{up}|$ and a phase of ($\phi_{up} + 180°$) to eliminate the upstream traveling component. This approach was implemented by first turning on the upstream speakers and taking a streamwise survey in the freestream to measure $\hat{F}$ using the SR830 lock-in amplifier. The two-point method was then applied between the first measurement point and all other subsequent points. The values of A_{dn} and A_{up} were then averaged in the complex plane to obtain space-averaged values. The downstream speaker was then appropriately set and the resulting wave field was then measured. The results obtained using this decomposition technique did not work well over a broad range of x values. The assumption that the wave system can be decomposed into a single downstream traveling wave and a single upstream traveling wave was not realistic near the leading and trailing edges of the model as a result of acoustic scattering. Also, multiple reflective surfaces exist throughout the acoustic path.

A simple approach was employed to generate a planar wave which yielded better results. Two streamwise surveys were taken in the freestream above the model, each at the same spatial coordinates. One survey was taken with only the upstream set of speakers activated and the second survey with only the downstream speakers energized. An arbitrary scale factor and phase shift was applied to the data from the second survey. Applying the method of superposition, the combined wave field with

ϵ	$u_{ac}\{m/s\}$	SPL
ϵ_1	8.44×10^{-4}	84.8
ϵ_2	1.63×10^{-3}	90.5
ϵ_3	3.24×10^{-3}	96.5

Table 3.3: Tabulated data of nominal freestream acoustic forcing levels.

both sets of speakers active was simulated. The scale factor and phase shift were selected to give the desired response, namely, a constant rms amplitude distribution. This was done by minimizing the standard deviation of the rms amplitude values. The selected scale factor was used to scale the input amplitude of the downstream speaker and the phase shift was added to the input phase. Five points in each survey were found to be adequate. After adjusting the universal source for changes in the input signal to the downstream speaker, the wave field was measured for verification. Measured acoustic data will be presented in Section 4.3.

It was observed that the acoustic field varied from day-to-day presumably due to minor changes in the environment, in particular temperature. Also, it was found that the speakers needed a long time to reach a steady state condition and this too may have been responsible for some of the daily variations observed. To combat these difficulties, the speakers were energized 24 hours a day. This was not destructive to the speakers since the power supplied to the speakers was on the order of $1W$. Because of the simplicity of the plane-wave-generation method used, the method was applied or the acoustic field was reverified immediately after every hot-wire calibration. A condensor microphone (Larson-Davis model 2530) was also flush mounted on the sidewall of the test section upstream of the model leading edge to monitor changes in the acoustic field. If substantial changes were observed, the acoustic field was regenerated. The nominal values of the acoustic forcing levels in the form of ϵ, u_{ac}, and SPL are given in Table 3.3.

3.4 Mean-flow measurements

The mean flow measurements were sampled using a VXI model HP1413B card as discussed in Section 2.3 except for the digital-output Mensor gauge used to measure the settling chamber pressure. The lowpass filters on the card were set to $2Hz$. To obtain the mean values, a total of 256 samples were taken at a rate of $16.67Hz$. Direct measurements of the temperature, T, and relative humidity, ϕ, were obtained with the sensor located at the exit of the test section. Two pressure rings and a downstream pressure tap on the test section ceiling were used to monitor the tunnel velocity. One ring with four pressure taps (one on each wall) at the same streamwise position was located in the settling chamber. The other ring with two pressure taps (one on each sidewall) was located at the entrance of the test section. One of the pressure taps on the test-section ceiling (refer to Section 2.1) was used to monitor the tunnel velocity. The ceiling tap used was located downstream of the leading edge of the model at $x = 55.4cm$. The pressure measured in the settling chamber, P_{sc}, was used as the reference pressure for all differential pressure measurements. Fifty readings were averaged over a period of approximately $15.3sec$ to obtain the mean absolute pressure in the settling chamber.

Because of the sensitivity of the flow stability characteristics to the base flow, a high degree of accuracy is desirable for the mean flow properties. A detailed error analysis was conducted for the measured flow variables and is presented in AppendixA. The air in the tunnel inevitably contains a significant amount of moisture. As a result, humidity corrections were applied to the calculated values of density, ρ, and viscosity, μ, which in turn affects the Reynolds number, R. For the density corrections [113], an ideal gas model for the mixture of air and water vapor was assumed. Upon applying the law of partial pressures and the definition of relative humidity $\phi = P_v/P_{sat}$, the following expression was obtained

$$\rho = \rho_a \left[\frac{P - 0.3781\phi P_{sat}}{P} \right] \qquad (3.5)$$

where the dry air density ρ_a is given by

$$\rho_a = \frac{P}{R_a T} \tag{3.6}$$

and the saturation vapor pressure P_{sat} at the mixture temperature T is

$$P_{sat} = e^{a+b/T}. \tag{3.7}$$

Here P, P_v, and R_a denote the absolute pressure of the mixture, the partial pressure of the water vapor and the ideal gas constant for dry air, respectively. Equation 3.7 is essentially Clapeyron equation relating the saturation pressure and temperature for water vapor with a and b constants for a temperature range of $2 < T < 39°C$.

The humidity corrections applied to the viscosity are discussed here. The subscripts "v" and "a" that follow denote water vapor and dry air properties, respectively. Sutherland's viscosity formula [114] was used for the dry air viscosity

$$\mu_a = 1.458 \frac{T^{3/2}}{T + 110.33} \times 10^{-6} \ \{Pa \cdot s\} \tag{3.8}$$

with an error less than $\pm 2\%$ in the range $167 < T < 1900K$. An empirical equation for the viscosity of water vapor [115] approved by the special committee of the International Association for the Properties of Steam in 1975 was used,

$$\mu_v = 10^{-6}\sqrt{T} \Big/ \left(\sum_{k=0}^{3} a_k (T/T_0)^{-k} \right) \ \{Pa \cdot s\} \tag{3.9}$$

where the a_k's and T_0 are constants for temperature $273 < T < 1000K$. For the temperature range of interest, uncertainties in μ_v are approximately $\pm 2\%$. Refer to Reference [115] for numerical values of coefficients. Derived from kinetic theory, Wilke's equation [116] was used to compute the viscosity of the moist air

$$\mu = \frac{\mu_v}{\left[1 + \left(\frac{P_a}{P_v}\right) \cdot \frac{\left[1 + \left(\frac{\mu_v}{\mu_a}\right)^{1/2} \left(\frac{M_v}{M_a}\right)^{1/4} \right]^2}{\left[8\left(1 + \frac{M_v}{M_a}\right) \right]^{1/2}} \right]} + \frac{\mu_a}{\left[1 + \left(\frac{P_v}{P_a}\right) \cdot \frac{\left[1 + \left(\frac{\mu_a}{\mu_v}\right)^{1/2} \left(\frac{M_a}{M_v}\right)^{1/4} \right]^2}{\left[8\left(1 + \frac{M_a}{M_v}\right) \right]^{1/2}} \right]} \tag{3.10}$$

where M is the molecular weight and the ratio of mole fraction was replace by the ratio of partial pressures assuming ideal gas. The above relations, Equations 3.5 to 3.10, were used to get an *accurate* representation of the fluid properties of interest.

66

Percent differences between the dry and moist air properties of approximately 1% and 2% were obtained on very humid days for the density and viscosity, respectively.

To avoid the intrusion of pitot-static probes, static pressure taps were used to calculate the tunnel velocities. The total pressure P_T in the tunnel was first estimated by applying Bernoulli's equation and Mass conservation equation between the settling chamber and test-section entrance. The assumption that the settling chamber pressure P_{sc} essentially equals P_T was not employed. The following expression assuming incompressible flow was obtained, namely,

$$P_T = P_e + \frac{P_{sc} - P_e}{1 - \left(\frac{A_e}{A_{sc}}\right)^2} \tag{3.11}$$

where A denotes cross-sectional area and the subscripts "sc" and "e" refer to settling chamber and test-section entrance locations, respectively. To verify velocity measurements made with the static taps, a pitot-static probe manufactured by United Sensor was installed for comparison. The probe was installed at the same streamwise position as the ceiling tap located $x = 55.4cm$ downstream of the leading edge of the model and approximately $y = 14.0cm$ above the model surface. The tunnel velocity was varied between $0.5 < U_\infty < 13m/s$ and both sets of measurements were taken simultaneously. Velocity measurements were taken while increasing and decreasing tunnel speed to account for hysteresis effect. Figure 3-4 shows a plot of the absolute percent difference of the velocities versus tunnel velocity. The maximum percent differences realized were well within the experimental uncertainty of the measurements (refer to Appendix A).

3.5   Hot-wire measurements

This section documents the procedures taken to acquire the hot-wire data to be discussed in subsequent sections. The types of hot-wire measurements obtained will also be addressed.
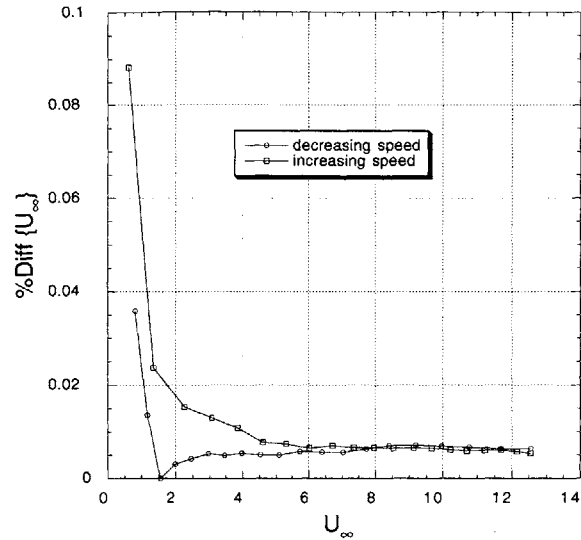
Figure 3-4: Plot of percent difference between tunnel velocities measured using static pressure tabs and pitot-static probe versus tunnel speed.

3.5.1 Calibration procedure and analysis

The tunnel was typically turned on for at least a half hour to achieve thermal equilibrium before any data was acquired. The hot-wire probe was then positioned at the calibration location – $x = 55.4cm$, $y = 14.0cm$, and at the spanwise centerline – where x was the distance from the model leading edge and y the distance from the model surface. The static pressure tap used to measure the tunnel velocity was located on the tunnel ceiling above the probe. The calibration was usually conducted over a freestream velocity range of $1 < U_\infty < 13m/s$. Twenty velocity points were typically acquired with variable velocity increments. The velocity increments were set such that the value of the increments decreased with decreasing tunnel velocity. This was desirable since the wire sensitivity, dE/dU, increases with decreasing velocity. The velocity was set by a voltage source via the computer and allowed to settle for a specified time period between successive data points. The time to perform a calibration was minimized by experimentally obtaining an optimum settling time between data points. The optimum settling time was obtained by determining the minimum time needed to avoid hysteresis. Calibrations were done by first operating the tunnel at the maximum velocity then methodically decreasing the tunnel velocity until the

minimum was reached. During calibration, the anemometer voltage, E, static-tap velocity, U_∞, and other mean flow properties were acquired by lowpass filtering at $2Hz$ and time-averaging 256 samples taken at a rate of $16.67Hz$.

Before the actual hot-wire calibration was performed, the anemometer was first configured with the wire exposed to the maximum velocity. A constant-temperature anemometer was configured to use a $1 : 20$ bridge configuration. The wire resistive overheat ratio, $\tau_r = r_{hw}/r_{cw}$, was set by first measuring the cold wire resistance, r_{cw}, and then adjusting the internal high precision decade resistance to obtain the desired heated resistance, r_{hw}. An overheat ratio of $\tau_r = 1.8$ was used throughout the experiment. The next step was to determine the frequency response of the system (probe + anemometer). This was done by applying an electronic disturbance signal at the top of the anemometer bridge, square-wave test [117]. The anemometer response was then viewed on an oscilloscope. To obtain a proper square-wave response, the gain was adjusted to compensate for wire probe frequency roll off and the cable was trimmed by varying the bridge reactance. A system bandwidth of approximately $40kHz$ was achieved throughout the study.

The acquired calibration data was used to obtain a functional relationship between the mean static-tap velocity U_∞ and wire voltage E. A fourth-order polynomial fit was found to work well for the calibration, namely,

$$U = \sum_{n=0}^{4} a_n E^n \tag{3.12}$$

where the a_n's are the calibration coefficients. A plot of a typical calibration curve along with the least-squares fit is given in Figure 3-5. If the mean square errors of the calibration fits were greater than $10^{-3}\{m/s\}^2$, the calibration was repeated. The hot wires were typically re-calibrated after four hours of continuous operation or sooner if random calibration checks revealed errors between the static-tap velocity and wire velocity to be larger than about $\pm 1.5\%$.

The tunnel was enclosed in a temperature controlled environment; as a result, temperature drifts in the tunnel flow were nominally less than $\pm 1°C$ throughout the day after thermal equilibrium was achieved. A linear temperature correction [118]
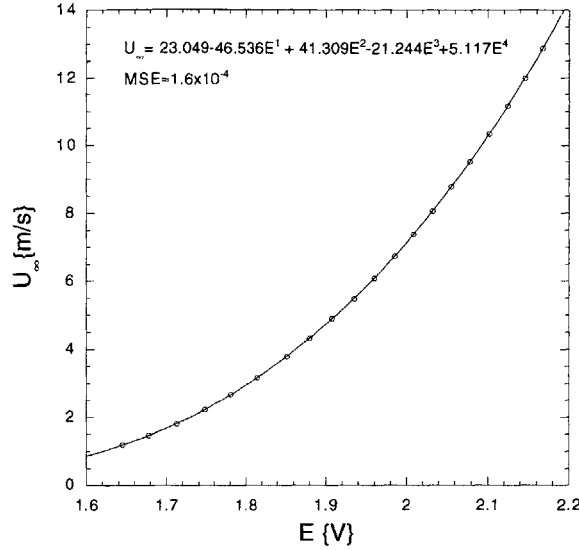
Figure 3-5: Typical hot-wire calibration curve with calibration coefficients and mean square error.

was found to be an adequate form of temperature compensation for this test. The linear correction formula can be expressed as

$$E_c = E \left[\frac{T_w - T_{cal}}{T_w - T} \right]^{1/2} \tag{3.13}$$

where E_c is the corrected output voltage, T_w is the average wire temperature, T_{cal} is average calibration temperature, and T is the air temperature. Upon substituting the linear temperature-resistance relationship for the wire, the above expression simplifies to

$$E_c = E \left[1 - \frac{\alpha}{\tau_r - 1}(T_w - T) \right]^{-1/2} \tag{3.14}$$

where α is the temperature coefficient of the wire sensor. A value of $\alpha = 0.0036/^\circ C$ was used for the platinum-coated tungsten wires.

For subsequent dynamic hot-wire measurements, the hot-wire signal E was divided into two components, a mean and fluctuating component, to take full advantage of the A/D's dynamic ranges. The acquisition of the mean component was discussed above. The fluctuating component $e(t)$ was obtained by AC coupling and amplifying the signal using a band-pass filter/amplifier (SR650). The instantaneous hot-wire signal $E(t)$ was then obtained by summing the mean component of E and the fluctuating component $e(t)$. The corrected voltage signal $E_c(t)$ was then obtained using

Equation 3.14 which was then substituted into Equation 3.12 to obtain the instantaneous wire velocity $U(t)$. The resulting mean velocity U and root-mean-square (rms) velocity u were obtained by using this direct approach. Because the largest measured frequencies of $U(t)$ were always less than 2% of the tuned bandwidth of the anemometer system $(40kHz)$, phase corrections were not implemented.

The acquisition of narrow-band phase-locked data was an integral part of the experiments. Two approaches were utilized to obtain this type of data. The first approach used a lock-in amplifier (SR830) where the TTL signal from channel one of the universal source was used as the reference signal. The time constant and slope of the internal filters were typically set to $3s$ and $24dB/oct$, respectively, in order to reduce unwanted noise near the reference frequency. A total of 256 samples taken at a rate of $16Hz$ were time averaged to get the output rms signal and phase relative to the reference signal. In addition to setting the $-3dB$ point of the filter, the time constant is also a measure of the system's response to changes in the input signal. For the current test, it was observed that a settling time of approximately 8 time constants were necessary to get steady output results. In certain situations, time constants as large as $10s$ were recommended requiring a settling time of approximately $80s$ before acquiring the data. For this reason, the SR830 was utilized sparingly.

The second approach involved simultaneous broadband acquisition of the anemometer output and reference signal (sinusoidal output from channel one of the universal source). Unless otherwise stated, 40960 points were sampled at a rate of $1kHz$ on each channel and the anemometer output was band-pass filtered between $2Hz$ and $400Hz$. Typical gain amplifications were in the range of $40dB$ to $80dB$. The instantaneous velocity $U(t)$ and reference signal V_{ref} data were post processed to get the desired narrow-band phase-locked results. Linear time series analysis [119, 120] was applied to obtain auto spectral densities, $S_u(f)$ and $S_{ref}(f)$, and the cross spectral density $S_{u,ref}(f)$ between the hot-wire data and reference signal. The records were broken into blocks of 2048 points and a Hanning window was applied to each data block. Fifty percent overlapping of data windows was employed which resulted in 39 data windows for ensemble averaging. This provided excellent convergence for this

study. The coherence function,

$$\gamma(f) = \frac{|S_{u,ref}(f)|^2}{S_u(f) \cdot S_{ref}(f)},\qquad (3.15)$$

was used to measure the linear relation between the velocity and reference signal at the frequency f_o of V_{ref}. For cases where there was a strong correlation, $\gamma(f_o) \approx 1$, the rms amplitude was computed by integrating the $S_u(f)$ in a $2Hz$ bandwidth around f_o and the relative phase by computing phase angle of $S_{u,ref}(f)$ at f_o. Both approaches for obtaining phase-locked data were consistent, but the simultaneous sampling approach was more expeditious when broadband data were also of interest.

3.5.2 Freestream measurements

Freestream turbulent intensities u/U_∞ for a bandwidth of $0.1 < f < 400Hz$ were measured at different freestream locations using a hot-wire probe. A larger number of points were sampled for these measurements (81920 or 204800) to increase the frequency resolution of the spectral data. The corresponding number of points per block was 4096 or 8192. These measurements were necessary to evaluate the freestream flow quality, spectral content and rms value. The acoustic field generated by the speakers was also measured in the freestream to quantify the forcing levels and characteristics of the wave.

3.5.3 Boundary-layer measurements

Hot-wire measurements were acquired in the boundary layer to estimate the transition Reynolds number, $Re_{tr} = \rho U_\infty x_{tr}/\mu$, on the plate and to infer the quality of flow in the tunnel. These measurements consisted of 81920 points sampled at a rate of $2kHz$ and band-pass filtered from $2Hz$ to $800Hz$. The probe was positioned at a fixed location in the boundary layer near the wall at $x = 177.8cm$ and $y \approx 1.3mm$. The tunnel velocity was slowly increased until the transition location swept by the probe. This was repeated by slowly decreasing the tunnel velocity to look at hysteresis effects. Both the mean and rms fluctuating velocity were then used to estimate the value of

Re_{tr}. As the boundary layer changes in character from laminar to turbulent flow, the mean profile in the near-wall region becomes fuller and a marked increase in U/U_∞ was observed. Similarly, a marked increase in the rms velocity fluctuation u/U_∞ was also observed. Results are presented in Section 4.2.

Short streamwise surveys at a fixed y-location were obtained in the boundary layer at a wall-normal location near the maximum of the T-S wave amplitude. Approximately 76 points were obtained over a streamwise extent of approximately $1.5\lambda_{ts}$ ($76mm$). These measurements were used to compute the kinematic characteristics of the T-S waves and limited receptivity coefficients.

Complete and partial boundary-layer profiles were taken extensively. The wall-normal distance of the probe to the model surface was known only approximately. The partial boundary-layer measurements typically started at $U/U_\infty \leq 0.5$ and ended near the surface. A fixed step size of $\Delta y = 0.1mm$ was typically used for the partial profiles. The partial profiles were taken to include the maximum of the T-S wave amplitude. The complete boundary-layer profiles were taken to obtain mean velocity boundary-layer profiles and full T-S eigenfunction profiles. The complete profiles started in the freestream and ended near the surface. Initially a fixed step size of $\Delta y_o = 0.5mm$ was employed until a value of $U/U_\infty = 0.995$ was obtained. At that point a variable step size that decreased quadratically with the approximate distance from the surface was utilized. After a minimum step size was reached $\Delta y = 0.2\Delta y_o$, this fixed value was used for the remaining points in the profile. Laminar profiles were terminated by setting a value of the minimum velocity, typically $U/U_\infty = 0.1$. The y positions were determined by linearly extrapolating to $U/U_\infty = 0$ to get the wall location. The values of velocity used to extrapolate to the wall were in the range $0.25 < U/U_\infty < 0.35$. Values very near to the wall were not considered because of possible near-wall effects like blockage and thermal conduction. In some instances, highly transitional and/or turbulent profiles were measured and the above termination and wall-location procedures were not adequate. For these cases, a fouling tip on the probe holder support (refer to Figure 2-2) was used to locate the surface at the given x location. The probe was moved until the fouling tip made contact with the model

73

surface. A cathetometer was then used to measure the distance from the probe tip to the model surface. Boundary-layer surveys were then made knowing the location of the probe relative to the model surface. Both the extrapolation and fouling-tip procedures yielded very similar results which served as validation of the extrapolation approach.

3.6 Data reduction

3.6.1 T-S wave decomposition

In this section, a brief description which outlines the data reduction procedures utilized to decompose the measured disturbance field (amplitude and phase) is addressed. The current study employed a continuous wave train for the acoustic excitation. As a result, the measured rms narrow-band velocities $u_t e^{i\phi_t}$ included the Stokes wave response $u_s e^{i\phi_s}$, the T-S response $u_{ts} e^{i\phi_{ts}}$, and any other extraneous response (e.g. probe vibration) all at the same frequency f_o. Recent works [46, 48, 86, 121] have exploited the use of modulated acoustic bursts which simplifies the decomposition procedure. The differences in phase speeds of the T-S wave and Stokes wave result in separate signals in the time domain.

A Stokes/acoustic wave is present whenever an oscillating velocity disturbance exists in the freestream. The theoretical solution for a Stokes wave is given by Panton [122]. For the continuous wave train, several decomposition approaches have been investigated by Wlezien *et al.* [44, 33]. They found that consistent estimates of the T-S modes are achieved when the Stokes wave was directly estimated from the measured profiles. The various decomposition approaches exploit the fact that a large mismatch in the length scales exist between the Stokes wave and T-S wave. The ratio of the length scales for the current study was approximately 95 : 1, i.e. the Stokes wavelength being two orders of magnitude larger than the T-S wavelength.

One such approach is to make short streamwise surveys that cover approximately one T-S wavelength at a constant height in the boundary layer (see Wlezien [33]
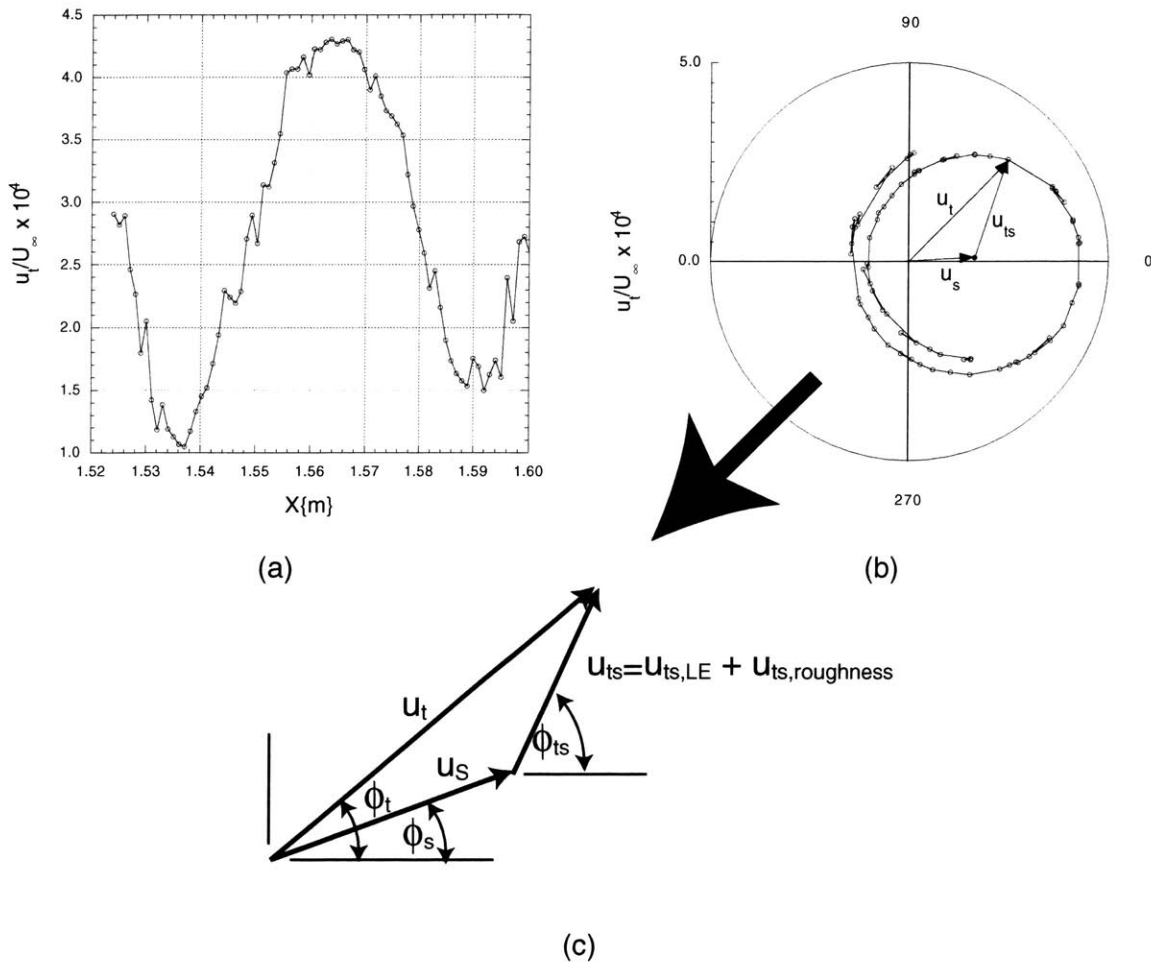
Figure 3-6: Example of decomposition method obtained from short streamwise surveys. Part (c) shows a vector diagram depicting Equation 3.16 used to extract T-S wave from measured disturbance field.

and Saric *et al.* [46]). Over one T-S wavelength, the phase of the Stokes wave (and for that matter any probe vibration) is for all practical purposes constant. The measured response $u_t e^{i\phi_t}$ can then be plotted on the polar complex plane. Since the T-S amplitude does not vary significantly over one T-S wavelength, the centroids (Stokes wave + vibration) and the average radii (T-S amplitudes) of the off-centered spirals can be computed over one T-S wavelength. The T-S wave measured here includes receptivity contributions from all possible sources, the leading edge and roughness sites. Such surveys were obtained in the current study at the location of lower maxima of the T-S mode shapes. Figure 3-6 shows a schematic with actual

data that outlines the steps discussed above. The streamwise amplitude plot shown in part (a) of the figure is modulated and illustrates the interference between the Stokes and T-S waves. The complex polar plot in part(b) indicates that both waves were of the same order of magnitude. The vector diagram in part (c) depicts the type of calculations necessary to extract the T-S wave. Using complex variables notation, the T-S wave amplitude and phase were expressed as

$$u_{ts}e^{i\phi_{ts}} = u_t e^{i\phi_t} - u_s e^{i\phi_s}.$$

(3.16)

Equation 3.16 was solved to obtain the T-S wave results. Because the T-S wave is a traveling wave, a linear relationship exists between the phase ϕ_{ts} and x. Linear regression was employed to compute the streamwise T-S wavenumber, $\alpha_{ts} = d\phi_{ts}/dx$, which was used to obtain some wave kinematic results (e.g. $\lambda_{ts} = 2\pi/k_{ts}$, $c_{ph} = 2\pi f_o/k_{ts}$, etc.).

Most of the disturbance measurements were acquired by making wall-normal surveys, complete and partial boundary-layer profiles, at selected streamwise locations. The approach taken here to extract the T-S wave component is a slight variation from the earlier methods used [33, 46]. No direct attempts were made in this study to measure or isolate the Stokes wave. Instead, the focus here was to get a measurement of the receptivity due solely to the surface roughness. Two sets of wall-normal disturbance profiles were obtained at the same streamwise locations and with the same acoustic forcing levels. One set was taken with a smooth plate and is denoted with "ss" subscripts for smooth surface conditions. A second set of disturbance profiles was obtained with roughness sites in place and the subscript "rs" denotes this condition. The disturbance measurements obtained on the smooth surface, $u_{ss}e^{i\phi_{ss}}$, include components of the Stokes wave, T-S wave due to leading-edge receptivity, and extraneous disturbances. The disturbances acquired with receptivity sites, $u_{rs}e^{i\phi_{rs}}$, include the same components measured on the smooth surface in addition to the T-S wave component due to the controlled roughness. This is shown graphically in Figure 3-7. This method was implemented by always taking a reference measurement in the freestream acoustic field ($y \approx 12.7cm$) as the first data point in each

76
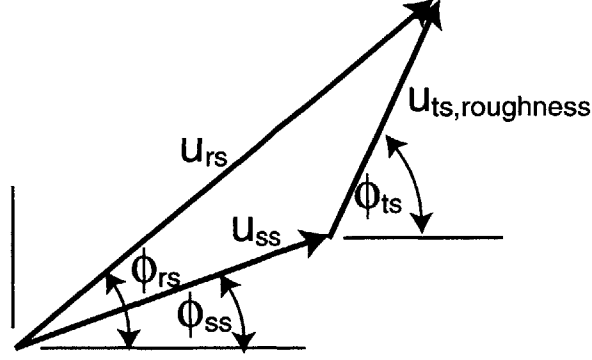
Figure 3-7: Graphical representation of decomposition method used for wall-normal surveys.

wall-normal profile. A phase correction was then applied to the smooth surface data as necessary by examining the phase difference between the corresponding reference measurements. The smooth-surface disturbance profile was then linearly interpolated to the wall-normal coordinates of the rough-surface disturbance data. The T-S wave component due to surface roughness was obtained using the following expression

$$u_{ts}e^{i\phi_{ts}} = u_{rs}e^{i\phi_{rs}} - u_{ss}e^{i\phi_{ss}}. \tag{3.17}$$

Here the T-S component includes receptivity due to acoustic scattering at the roughness sites of (1) the freestream acoustic field and (2) the leading-edge generated T-S wave. The receptivity due to the scattering of the leading-edge generated T-S wave was assumed negligibly small. This was supported by leading-edge receptivity measurements in the present experiment and measurements by Wlezien *et al.* [44] for a 24 : 1 elliptic leading egde, both of which indicated small T-S responses. Excellent results were obtained using this method.

3.6.2 Computation of receptivity coefficient

Linear stability results presented here were computed using a computer code by Malik [123] which incorporates quasi-parallel spatial stability theory. These results were used to facilitate the computation of the receptivity coefficients. The receptivity coefficients, C, presented here were all referenced to the Branch I location and are defined

as

$$C = \frac{u_{ts,I}}{u_{ac}} \tag{3.18}$$

where $u_{ts,I}$ is the maximum rms T-S amplitude at Branch I and u_{ac} is the rms freestream acoustic velocity fluctuation. Measurements of u_{ts} were made downstream of Branch I to take advantage of the linear amplification region for improved signal-to-noise ratios. The values of $u_{ts,I}$ were obtained by applying LST results (Equation 1.2) to the measured values of u_{ts} so that the receptivity coefficients were computed using

$$C = \frac{u_{ts}e^{-N}}{u_{ac}}. \tag{3.19}$$

Chapter 4

Results and Discussions: Mean Flow

Receptivity experiments are very sensitive to the state of the mean flow and environmental disturbances. As a result, great care must be taken to document the flow and environmental conditions to avoid ambiguous results as discussed by Nishioka & Morkovin [31] and Saric [111].

4.1 Boundary-layer characterization

As discussed in Section 3.2, global pressure measurements were first used to characterize the base flow. Streamwise hot-wire surveys where taken along the smooth plate to infer the pressure-gradient distribution. Figure 4-1 shows a plot of the streamwise velocity distribution at three wall-normal locations. The mean velocity U was normalized by the static-tap velocity U_∞ used to calibrate the hot-wire at $x = 55.4cm$. The pressure recovery region near the leading edge of the model is evident in the figure. Excellent agreement between the U/U_∞ measurements at the different y-locations was observed except for the pressure recovery region as expected and the region downstream of $x = 1.7m$. A slight adverse pressure gradient downstream of $x = 1.6m$ was observed particularly for the two larger y-locations. The normalized velocities from Branch I location to the end of the survey region ($0.5 < x < 2.03m$)
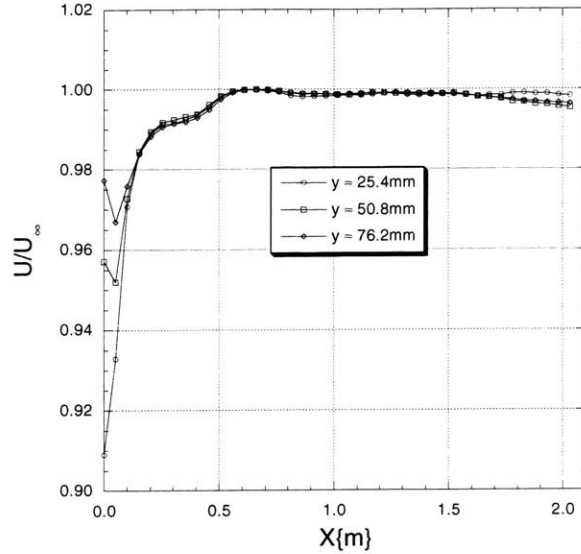
Figure 4-1: Freestream velocity measurements along model surface.

were within 0.25% of U_∞ for $y \approx 25.4mm$. The velocities along the plate insert location for roughness placement ($24.6 < x < 80.8cm$) were all within 1% of U_∞.

The leading edge of the model, $x = 0$, does not correspond to the origin of the boundary-layer flow. This is due in part to the finite thickness of the leading edge and the pressure recovery region generated downstream of the leading edge. For the properly configured model, the boundary layer developed into a nominally zero-pressure-gradient boundary layer downstream of the recovery region. For proper comparisons with theory, a new reference origin was defined, x_o, which is usually referred to as the virtual origin. The streamwise locations referenced to this origin are denoted by x_v. The virtual origin location was computed by first acquiring detailed boundary-layer velocity profiles on the smooth model every $254mm$ starting at $x = 508mm$. The profiles were numerically integrated to obtain the displacement thicknesses, δ^*. Since the displacement thickness is theoretically proportional to the $x^{1/2}$, a linear-regression curve fit was applied for δ^{*2} versus x. The linear curve fit was used to extrapolate upstream to a zero displacement thickness ($\delta^{*2} = 0$) and the corresponding x value was used as the virtual origin. A plot of δ^{*2} versus x obtained from the measured profiles is shown in Figure 4-2. Note that values of δ^* upstream

80
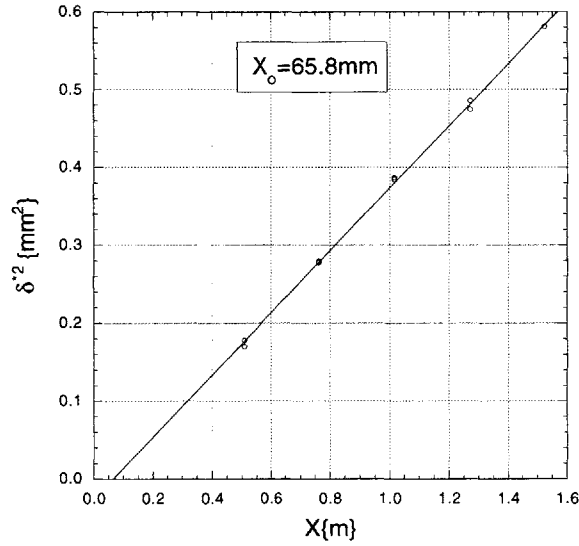
Figure 4-2: Displacement thickness versus streamwise position along with linear regression fit for location of virtual origin.

of $x = 0.5m$ were omitted from the linear fit since these results were obtained in the pressure recovery region and reliable boundary-layer measurements proved difficult in thin boundary layers. Values of δ^* downstream of $x = 1.6m$ were also omitted due to the slightly adverse pressure gradient region. The value of the virtual origin obtained was $x_o = 65.8mm$.

A more stringent test to characterize the boundary-layer flow was performed. The shape factor $H = \delta^*/\theta$ was computed where θ is the integral momentum thickness. Figure 4-3 shows a plot of the streamwise distribution of the shape factor. The theoretical Blasius value of $H = 2.59$ is also presented in the figure. The average value of the experimental shape factor was $\bar{H} = 2.60$ and all experimental values were within $\pm 1.5\%$ of $\bar{H}$. The presence of a slight adverse pressure gradient for $x > 1.6$ was evident from the marginally large values of shape factor evident in the figure. Finally, a plot of the measured normalize velocity profiles and the theoretical Blasius profile are presented in Figure 4-4. The streamwise distance relative to the virtual origin $x_v = x - x_o$ was used to compute the normalized wall-normal coordinate $\eta = (y/x_v) \cdot Re_x^{1/2}$. Excellent agreement was observed between the measured profiles and the Blasius profile using the virtual origin obtained.

81
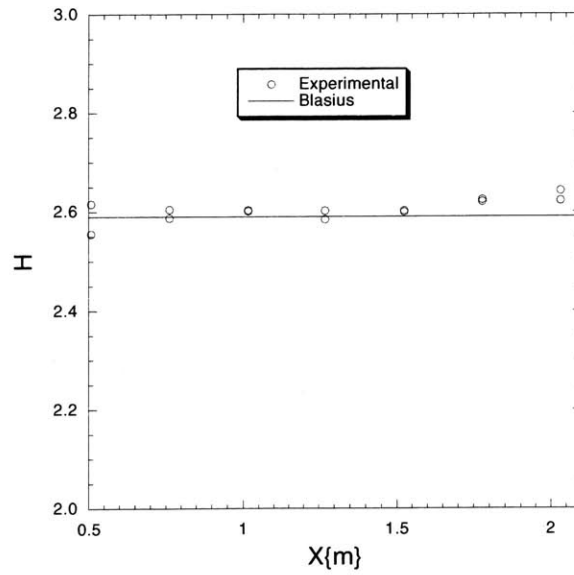
Figure 4-3: Streamwise distribution of experimental shape factors.
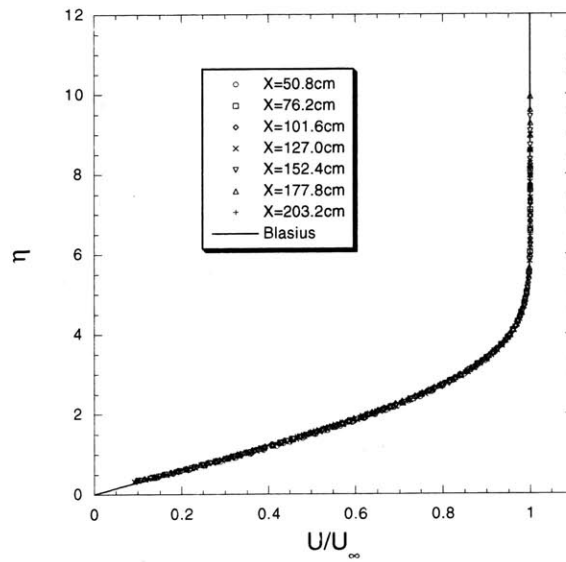
Figure 4-4: Normalized velocity profiles at selected streamwise locations.

All of the measurements presented above were obtained along the spanwise cen-terline $z = 0$ without the spanwise traverse installed. The two-dimensionality of the base flow was examined by making boundary-layer measurements at various span-wise locations utilizing the spanwise traverse from $z = -1.5cm$ to $z = 8.6cm$. These results were compared with the results obtained along the spanwise centerline. Ex-cellent agreement was observed between both sets of mean boundary-layer profiles validating the two-dimensionality of the base flow within the sidewall contamination region (see Figure 2-3). The excellent agreement also demonstrated that the pressure footprint near the model surface resulting from the presence of the spanwise traverse was minimal as per the design.

4.2   Freestream characteristics

Turbulent intensity measurements u/U_∞, where u is the rms value of velocity fluctu-ations, were obtained in the freestream using a single hot-wire probe. The value of u/U_∞, referred to throughout this document as the turbulent intensity, is believed to also include background acoustic disturbances (see Appendix B). Measurements were not acquired to separate the turbulent and acoustical components. The anemometer signals were band-pass filtered between $0.1Hz$ and $400Hz$ and sampled at a rate of $1kHz$. The freestream signals were typically amplified by $80dB$ before being sampled. Figure 4-5 presents some turbulent intensity data obtained with the model installed in the test section. The streamwise distribution shown in part (a) of the figure was obtained at $y \approx 12.7cm$ above the model surface. Values of $u/U_\infty \approx 0.1\%$ were mea-sured over the entire streamwise survey region. Data obtained from a wall-normal survey upstream of the model leading edge ($x = -2.54cm$) is given in part (b) of the figure. A fifty percent increase in the value of the turbulent intensity was seen im-mediately upstream of the leading edge of the model. This was due to an interaction between the flow field and model as it was not seen in measurements taken with the model absent.
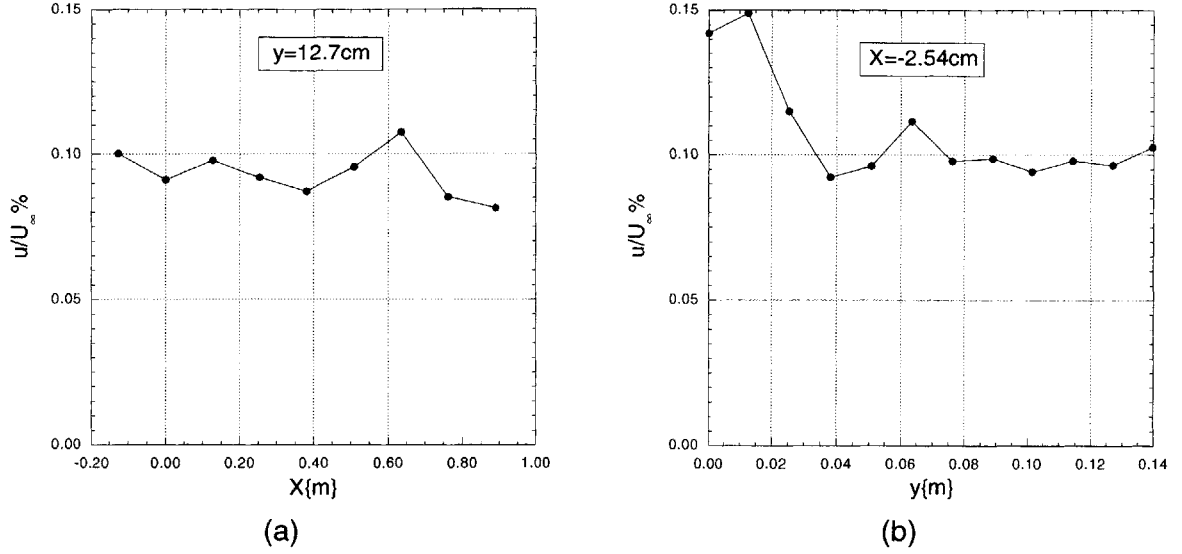
Figure 4-5: Measured turbulent intensities (a) streamwise and (b) wall-normal distributions ($0.1 < f < 400Hz$).

More important than the magnitude of the freestream turbulent intensity, the power spectral density of the freestream disturbances provided relevant information of the frequency content of the disturbance environment. Figure 4-6 shows a typical power spectral density of the freestream environment along with a line indicating the $-5/3$ power law ($S_u \propto f^{-5/3}$). The ordinate in the figure is

$$\left(\frac{u}{U_\infty}\right)^2 = 10 \cdot \log \frac{S_u}{U_\infty^2} \tag{4.1}$$

where S_u is the power spectral density of the fluctuating freestream velocity. Some unavoidable electronic noise is observed in the spectrum due in part to extremely low signal levels. There is fairly good agreement between the $-5/3$ line and spectra supporting the hypothesis that the freestream disturbances were composed predominantly of decaying turbulence. Most of the freestream energy was contained at very low frequencies, below $1Hz$. Energy within a given frequency band was obtained by integrating the spectrum $S_u(f)$ across the frequency band. Approximately 93% of the broadband energy was contained between $0.1Hz$ and $1Hz$. This illustrates the importance of specifying the frequency range when quoting turbulent levels.

Dynamic pressure measurements were obtained from four pressure transducers flush mounted on the test section sidewalls (refer to Appendix B). The separation
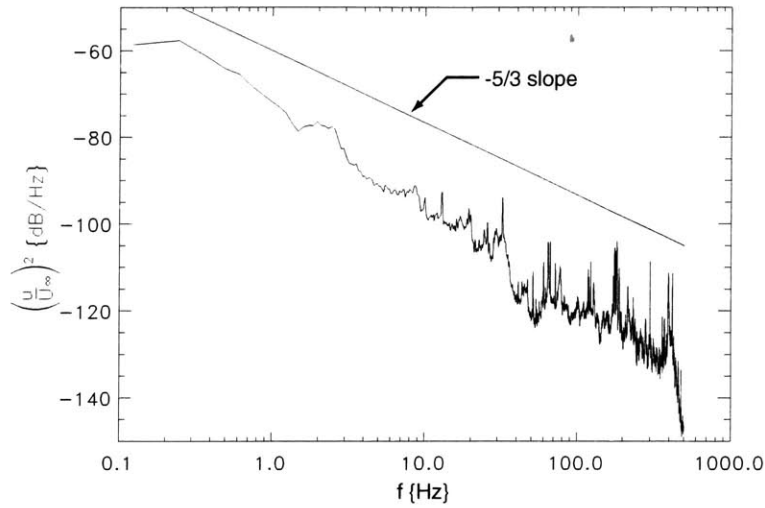
Figure 4-6: Freestream velocity spectra at $x = 25.4cm$, $y = 2.54cm$, and $z = 0$.

distances were small enough that pressure fluctuations due to acoustical and vortical disturbances would possibly be present in the cross correlations. The coherence function between various sensors indicated strong correlations for frequencies less than $40Hz$, at a frequency of $f \approx 220Hz$ associated with the rotor-stator interaction, and at discrete electronic-noise frequencies. These results confirm the absence of coherent disturbances in the freestream environment near the designed forcing field of the experiment ($f_o = 71Hz$) which can distort the interpretation of the results. These low-frequency coherent disturbances ($f < 40Hz$) are not considered dangerous since T-S amplification at these lower frequencies are postponed to larger Reynolds number values.

As a final check of the flow quality, the transition Reynolds number Re_{tr} was measured on the smooth plate. This was done by placing the hot-wire probe at a fixed location in the boundary layer and slowly sweeping through the tunnel speed range. The data obtained in this fashion are presented in Figure 4-7. Straight line fairings were drawn between the laminar data and transitional data. The intersections of the faired lines were taken as the onset of transition. The transition Reynolds number obtained from the normalized mean velocity was marginally larger than the value obtained from the normalized rms fluctuating velocity as expected. The average

85
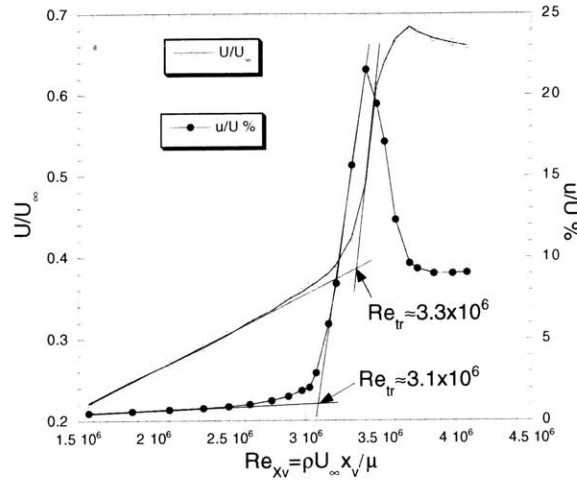
Figure 4-7: Measured transition Reynolds number on smooth plate with probe located at $x = 1.78m$, $y \approx 1.3mm$, and $z = 0$.

value of the transition Reynolds number is approximately $Re_{tr} = 3.2 \times 10^6$ indicating low freestream turbulent levels and a smooth model surface (for comparison, refer to data of Re_{tr} versus freestream turbulence cited in White [114]). A similar test was conducted on the plate with a two-dimensional roughness sample installed ($\Delta h = 71.1\mu m$). A 25% reduction in the value of transition Reynolds number was obtained with this configuration.

4.3   Acoustic-field characterization

The controlled acoustic field was measured in the freestream above the model surface. The data are shown in Figure 4-8 for both the amplitude (a) and phase (b) streamwise distributions. Data of the acoustic field with only the upstream speakers activated and the field with only the downstream speakers activated are also presented for completeness. The data of the generated acoustic field indicate some anomaly near the leading edge of the model due to acoustic scattering. In the vicinity of the insert region ($24.6 < x < 80.8cm$), the variation of the acoustic amplitude was small. The phase distribution in part (b) of the figure indicate a predominantly downstream-traveling wave. Note that a phase line with the theoretical slope is included in the
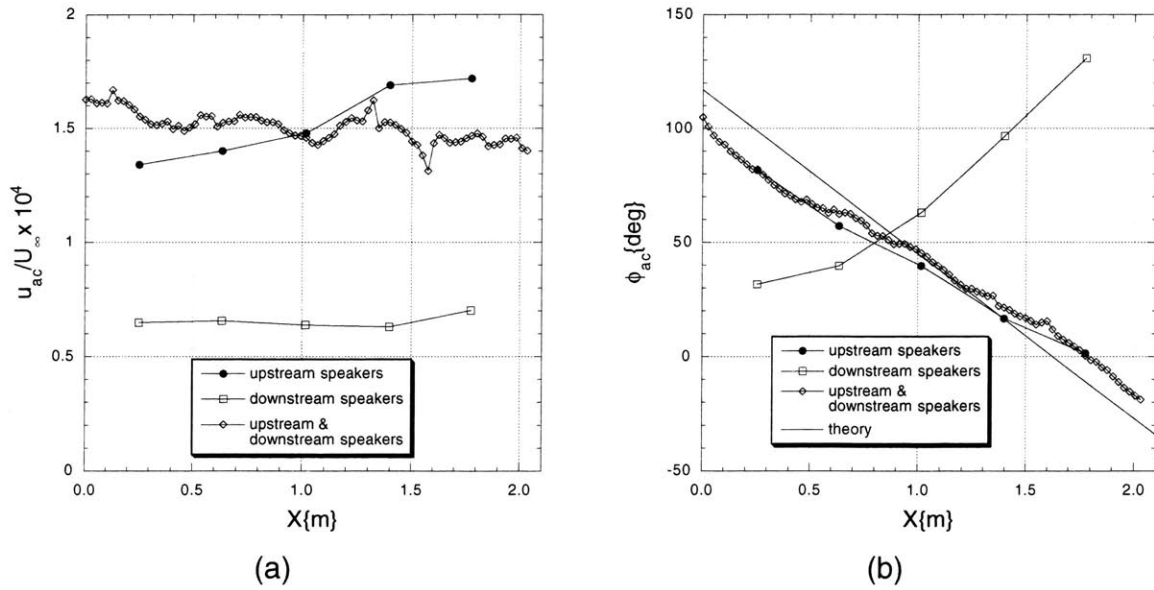
Figure 4-8: Measured freestream acoustic field generated in test section.

plot as a reference. Values of the acoustic amplitudes, u_{ac}, used for normalization in upcoming chapters are the average values measured over the plate insert. Streamwise measurements of the acoustic field were taken at various wall-normal locations and spanwise locations to verify the planar structure of the acoustic field.

4.4 Summary

Normalized streamwise velocity measurements just outside the boundary layer, $y \approx 25.4mm$, revealed deviations of less than 0.25% of U_∞ from $x = 0.5m$ to $x = 2.03m$. Characterization of the mean boundary layer indicated an average value of the shape factor to be $\bar{H} = 2.6 \pm 1.5\%$, compared to the theoretical Blasius value of $H = 2.59$. Excellent agreement was obtained between the theoretical Blasius profile and the measured normalized velocity profiles along the entire length of the measurement surface using the experimentally acquired virtual origin, $x_o = 65.8mm$.

The tunnel freestream flow quality was assessed by first measuring the turbulent intensity in the test section. Measured turbulent levels of $u/U_\infty \approx 0.1\%$ were acquired for $0.1 < f < 400Hz$. The most significant contribution to the turbulent intensity

was for frequencies below $1Hz$, about 93% of the broadband energy. The spectra were found to decay as a $-5/3$ power law, supporting the hypothesis that the freestream disturbances were composed predominantly of decaying turbulence. Coherent disturbances measured in the freestream were comprised primarily of low-frequency disturbances ($f < 40Hz$) not considered detrimental to this experiment. Transition was measured on the model at elevated tunnel speeds. A value of $Re_{tr} \approx 3.2 \times 10^6$ was measured indicating low freestream turbulent levels and a smooth model surface.

The controlled acoustic field was characterized by performing streamwise and wall-normal surveys in the freestream above the model surface. The acoustic field was found to have a planar structure and the amplitude and phase distributions indicated a predominantly downstream-traveling wave.

Chapter 5

Results and Discussions: Two-Dimensional Disturbances

In this chapter, results are presented and discussed for the fluctuating velocity disturbances measured with two-dimensional surface waviness (refer to Figure 2-4(a)). A previous acoustic receptivity experiment was conducted with two-dimensional surface waviness by Wiegel and Wlezien [83] (see discussion in Section 1.1.3). Characteristics of the measured T-S waves are compared with linear stability theory results where applicable. Experimental and theoretical receptivity coefficients are compared when available. A plot of nondimensional spatial growth rates, α_i^*, versus Reynolds number for a two-dimensional T-S wave was presented in Figure 1-2. The data were computed using LST [123] and nondimensionalized using the length scale δ_r ($\delta_r = x/R$).

5.1 Influence of acoustic forcing level and roughness height

The influence of acoustic forcing level, u_{ac} (or $\epsilon = u_{ac}/U_\infty$), and roughness height, Δh, were examined by conducting measurements using the matrix arrangement shown in Table 3.1. At the location of Branch I ($x_I = 53cm$) , the Reynolds number was $R_I = 585$ ($R = \sqrt{\rho U_\infty x_v/\mu}$). The reader is reminded to refer to Table 3.2 for tabulated data
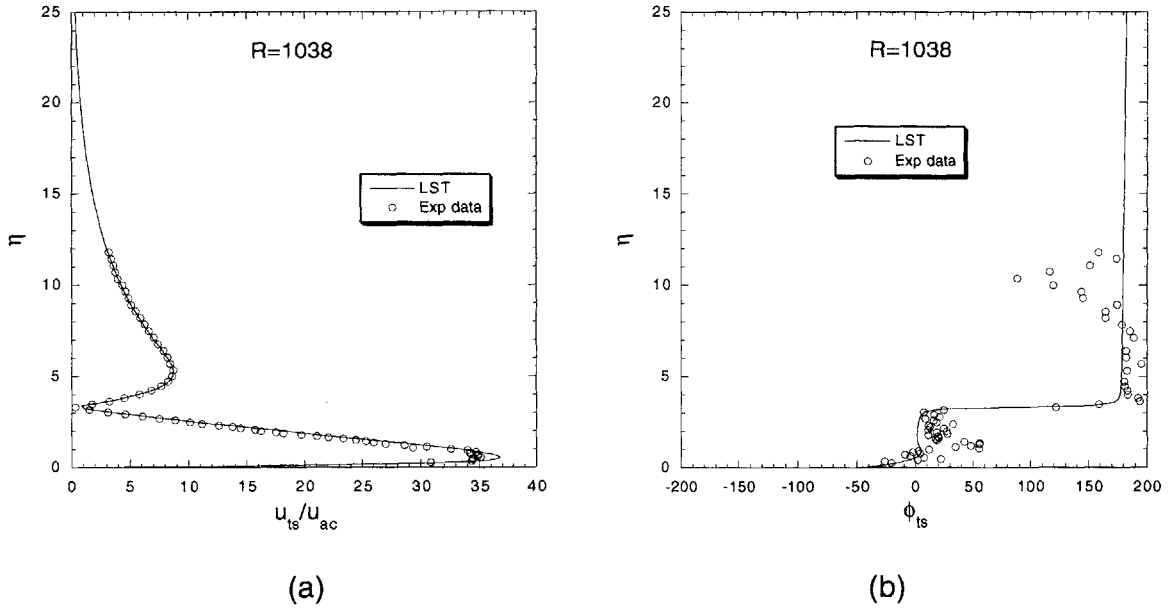
Figure 5-1: Comparison of a typical (a) amplitude and (b) phase of a measured T-S wave and a computed O-S eigenfunction (ϵ_3, Δh_3).

of streamwise location, x, versus Reynolds number, R. The largest roughness height, Δh_3, had a non-dimensional height of $\Delta h_3/\delta_I^* = 0.05$ and a roughness Reynolds number of $Re_{\Delta h} = 47$. Therefore, all roughness heights considered were well within the roughness Reynolds number range of a *hydraulically smooth* surface [114]. The T-S wavenumber $\alpha_{ts,I}$ at Branch I ($\alpha_{ts,I} = \alpha_{ts,r}$, where $\alpha_{ts,r}$ is the real component of the T-S wavenumber) was computed using LST and the corresponding T-S wavelength was $\lambda_{ts,I} = 50.245mm$. Measurements were obtained over a range of Reynolds numbers, $570 < R < 1205$ ($50.8 < x < 203.2cm$), that extended just beyond the location of Branch II ($R_{II} = 1129$).

The results presented in this section were obtained for the condition where the wavelength of the wall roughness λ_w matched that of the T-S wave at Branch I, the *near-resonance* condition. Here, the term near-resonance describes the condition when $\alpha_w = \alpha_{ts,I}$ which does not account for the finite speed of the freestream acoustic wave, i.e. $\alpha_{ac} \neq 0$. Samples $1-3$ (refer to Table 2.1) were used as the roughness sites where $\lambda_w = 50.25mm$. Example plots showing comparisons between the measured and theoretical T-S amplitude and phase profiles are shown in Figure 5-1 for $R = 1038$
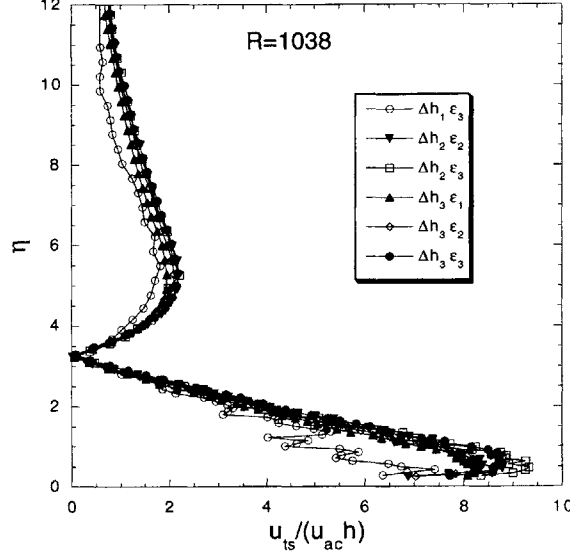
Figure 5-2: Normalized T-S amplitude profiles for various values of u_{ac} and Δh.

$(x = 152.4cm)$. The theoretical amplitude was scaled to match the experimental amplitude at the outer peak location near the boundary-layer edge $(\eta \approx 5)$. Excellent agreement is observed between the experimental and theoretical profiles validating the T-S decomposition approach. Some scatter is observed in the phase data but there is overall agreement with the theoretical trend. The $180°$ phase shift at $\eta \approx 2\delta^*$ is evident in the plots.

Measurements of T-S amplitudes at locations just downstream of Branch I indicated a virtually linear response of u_{ts} with both u_{ac} and Δh. Data are shown in Figure 5-2 at $R = 1038$ for various values of u_{ac} and Δh. The rms T-S amplitude u_{ts} was normalized by u_{ac} and h where h is the step height normalized by the smallest step height $(h = \Delta h_k / \Delta h_1$ where $k = 1, 2,$ or $3)$. The linear behavior is evident from the figure and indicate linear receptivity for all acoustic and wall forcing levels considered. Data depicting the streamwise evolution of the T-S eigenfunctions are shown in Figure 5-3 along with the LST results for the forcing product $\epsilon_2 \cdot \Delta h_3$. The LST results were again normalized to match the experimental amplitudes at the outer peak. Agreement between LST and measurements is good except for the profile at $R = 1205$ where nonlinear effects were apparent in the near-wall region. This profile was downstream of Branch II $(R_{II} = 1129)$ in a region of linear decay. Linear decay
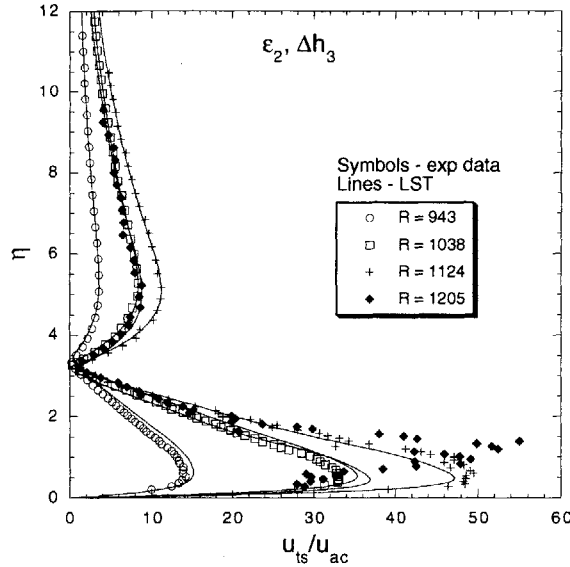
Figure 5-3: Streamwise evolution of T-S eigenfunctions for $\epsilon_2 \cdot \Delta h_3$.

was observed in the outer region of the boundary layer but not in the near-wall region. A decrease in the value of the coherence function, $\gamma(f_o)$, between the T-S wave and the input signal used for the acoustic forcing was observed indicating a loss of linearity. Other data (not shown) indicate that the evolution of nonlinear effects become evident at the same streamwise location for a given value of the forcing product, $\epsilon \cdot \Delta h$, independent of the individual values of ϵ or Δh.

The streamwise amplitude distribution of the measured T-S eigenfunctions were compared to the amplification predicted by LST. Figure 5-4(a) shows a plot of LST predicted N-factor ($N = \ln(u_{ts}/u_{ts,I})$) versus Reynolds number and the experimentally measured T-S amplitudes for a condition where nonlinear effects were not evident ($\epsilon_2 \cdot \Delta h_2$). The data were obtained from measured eigenfunction profiles taken at selected streamwise locations. Here the experimental amplitudes ($\ln(u_{ts}/u_{ac})$) were shifted for comparison with the LST N-factors. The filled symbols in the plot represent the outer maxima (local) of u_{ts} and the open symbols represent the inner maxima (global). Excellent agreement between the measured and LST data is evident except for the large values of u_{ts} measured at the lower peak for $R = 717$ just downstream of Branch I (in a region over the wavy surface). The large values of u_{ts} measured in the near-wall region just downstream of Branch I ($R_I = 585$, $x_I = 53cm$) may
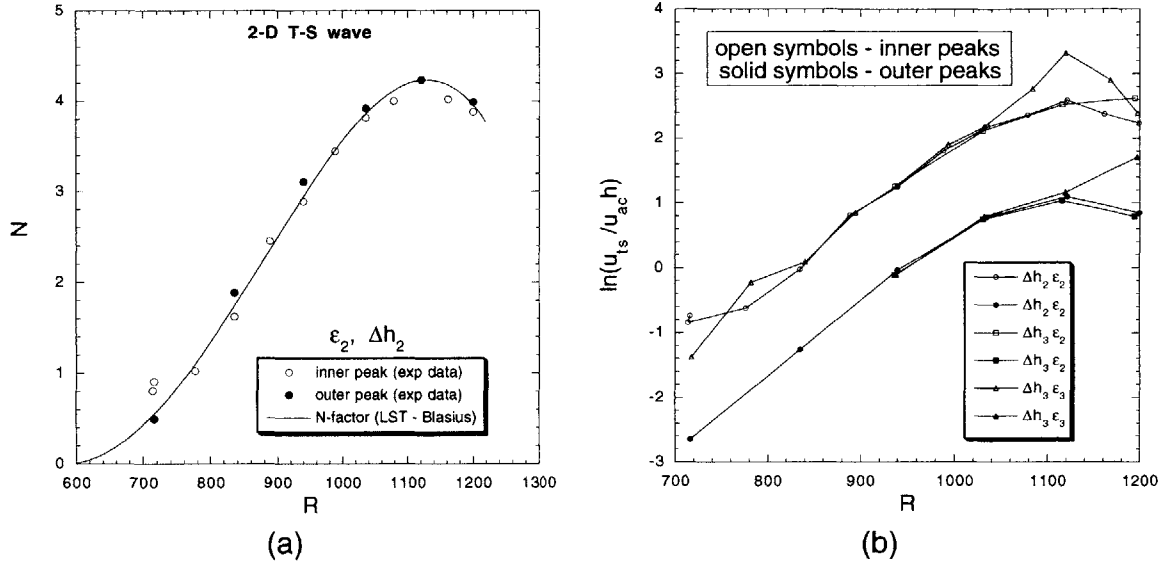
Figure 5-4: Streamwise amplification data for two-dimensional disturbances.

partly be explained by the non-monotonic increase of the total instability response resulting from the localized peak (overshoot) in the receptivity region due to the external forcing [85, 24]. The location of the upper branch (Branch II) is in excellent agreement with LST. The data also demonstrate that consistent amplification curves are obtainable by tracking either the inner or outer peaks, provided the response is linear. This is important since LST is required to backtrack the effective Branch I amplitudes in an accurate fashion.

Figure 5-4(b) shows a similar plot for various values of u_{ac} and Δh. Again, the solid symbols represent data of the lower peak and the open symbols data of the upper peak. Nonlinear effects are evident from the amplification curves for the forcing products of $\epsilon_2 \cdot \Delta h_3$ and $\epsilon_3 \cdot \Delta h_3$. For the case of $\epsilon_2 \cdot \Delta h_3$, nonlinear effects are apparent only in the near-wall region and first become discernible when $u_{ts}/U_\infty > 0.8\%$ at $R \approx 1120$ (just upstream of Branch II, $R_{II} = 1129$). For the largest forcing product ($\epsilon_3 \cdot \Delta h_3$), nonlinearity is evident in both the near-wall and outer regions of the boundary layer. The nonlinearity was observed first near the surface and eventually spread throughout the shear layer due to the interaction of normal vorticity which is driven by the mean shear (see Cohen, Breuer, & Haritonidis [100]). Nonlinearity was first observed for

93
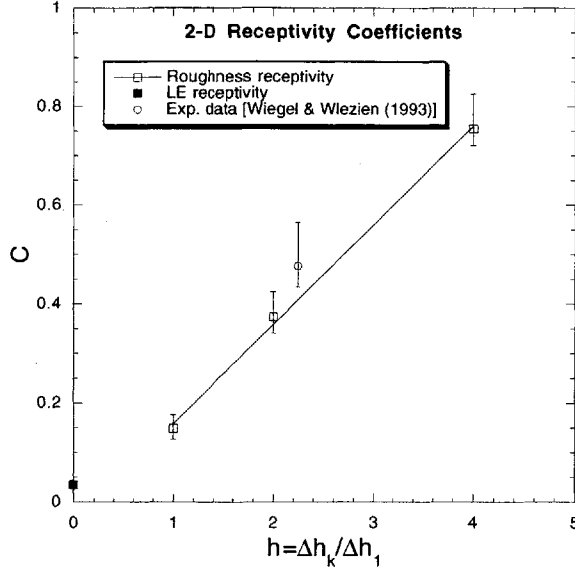
Figure 5-5: Nonlocalized receptivity coefficients from present experiment ($F = 55 \times 10^{-6}$) and past experiment ($F \approx 46 \times 10^{-6}$) as a function of wall roughness height for 2-D waviness.

$u_{ts}/U_\infty > 1.0\%$ at $R \approx 1034$ ($R < R_{II}$).

The measured amplification data were first compared to LST amplification results to validate the linear response of u_{ts} with respect to u_{ac} and Δh before being used to compute receptivity coefficients. Receptivity coefficients C referenced to Branch I were computed utilizing Equation 3.19. The additional stipulations that all values of u_{ts} employed were obtained downstream of Branch I and the roughness surface and upstream of Branch II were also implemented. Figure 5-5 shows a plot of the experimental receptivity coefficients versus the step height normalized by Δh_1. Data from the experiment of Wiegel and Wlezien [83] for a different nondimensional frequency ($F \approx 46 \times 10^{-6}$) are also included. The symbols in the plot represent mean values and the error bars represent the maximum plus/minus deviations observed in the measurements for all values of u_{ac}. The line in the plot is a linear regression fit for the current roughness receptivity data. The leading-edge receptivity coefficient for the smooth surface ($h = 0$) was calculated using data obtained in short streamwise surveys. The roughness receptivity coefficients were obtained from measured T-S eigenfunctions. The small values of the leading-edge receptivity coefficients ($C \approx 0.035$) support the decomposition assumption discussed in Section 3.6.1. Good

94
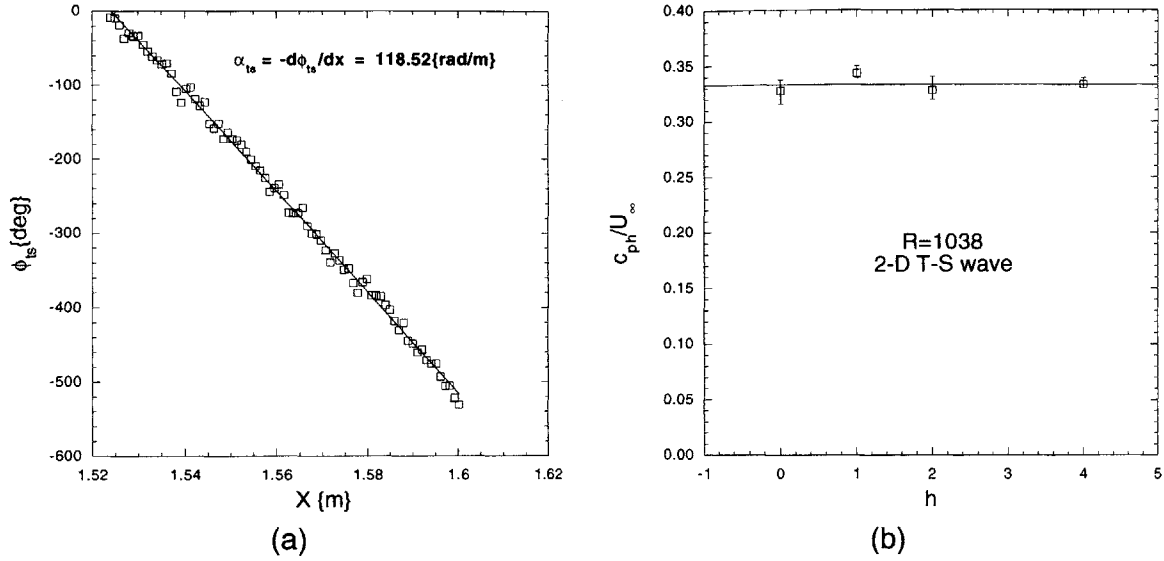
Figure 5-6: Kinematics of T-S waves at $R = 1038$: (a) T-S phase versus x and (b) T-S phase speed versus step height.

agreement is observed between the present and previous [83] experimental receptivity coefficients. Comparisons with theoretical receptivity coefficients will be made in the next section.

T-S wave kinematics were inferred from data obtained with short streamwise surveys. A typical plot of the T-S phase ϕ_{ts} versus streamwise distance is illustrated in Figure 5-6(a). The line in the plot is the linear fit of the data with slope $\alpha_{ts} = -d\phi_{ts}/dx$. The T-S wave phase speeds c_{ph} ($c_{ph} = 2\pi f_o/\alpha_{ts}$) for the various step heights are presented in Figure 5-6(b) where the line represents the mean phase speed ($\bar{c}_{ph}/U_\infty = 0.33$) for all values of u_{ac} and Δh considered. The phase speed computed from LST at $R = 1038$ is $c_{ph}/U_\infty = 0.33$. Excellent agreement is again observed between the measured and LST wave kinematics.

5.2 The effect of detuning

In this section, results are presented for the so-called *detuned* conditions. Detuning is referred to as the condition when there is a mismatch between the wavelengths of the wall roughness and the O-S mode ($\lambda_w \neq \lambda_{ts}$) for a given disturbance frequency.

95
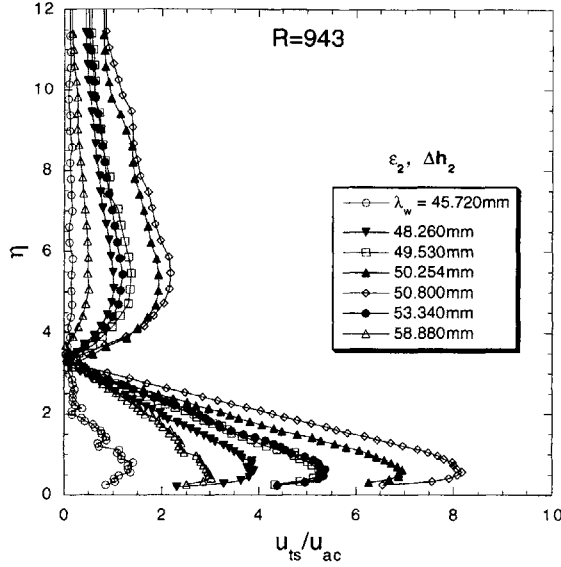
Figure 5-7: Measured T-S eigenfunctions at $R = 943$ for different values of wall-roughness wavelength.

The energy transfer from the forced disturbance becomes less efficient as the degree of detuning is increased. As a measure of the detuning, the detuning parameter σ is defined as

$$\sigma = \frac{\alpha_w - \alpha_{ts,I}}{\alpha_{ts,I}}. \tag{5.1}$$

In previous studies (e.g. Wiegel and Wlezien [83]), detuning was generally examined by varying U_∞ which consequently varied $\alpha_{ts,I}$. This was done because of the difficulty in making changes to α_w (see Section 2.4.1). Because of the type of receptivity sites used in the current study, the detuning parameter was varied by changing α_w.

Detuning data were obtained using samples 2 and $4 - 9$ (refer to Table 2.1) and were all obtained with the forcing product $\epsilon_2 \cdot \Delta h_2$. T-S amplitude profiles for the various roughness samples are presented in Figure 5-7 for $R = 943$. The effect of detuning is clearly evident by the variation in the boundary-layer response u_{ts} with changing wall roughness wavenumber. Note that the maximum response was not obtained for the near-resonance condition $\alpha_w = \alpha_{ts,I}$ (i.e. $\lambda_w = 50.25mm$). The receptivity theory assumes incompressible flow (infinite acoustic wave speed) which gives the above resonance condition. To account for a finite acoustic wave speed, one has to take into consideration the wavenumber of the freestream acoustic wave, α_{ac}, as

2-D Receptivity Coefficients (ε_2, Δh_2)

□ Experimental Data (C_{max}=0.427)
▲ Theory [Choudhari (1993)] (C_{max}=0.461)
— Theory [Crouch (1992)] (C_{max}=0.472)

C/C_{max}

σ' {%}
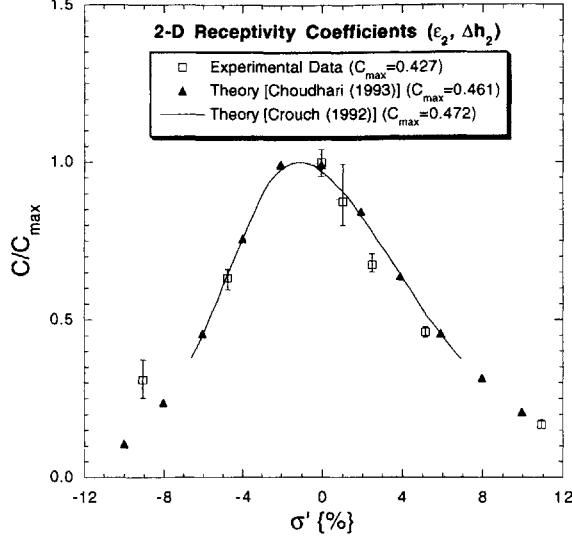
Figure 5-8: Measured ($F = 55 \times 10^{-6}$) and theoretical ($F = 55 \times 10^{-6}$ and $F = 56 \times 10^{-6}$) receptivity coefficients versus the detuning parameter.

conjectured by Wiegel [84]. For the present experiment, care was taken to acoustically excite the freestream with a downstream-traveling wave. Choudhari & Streett [29] addressed the finite wave speed effect and showed that a resonance condition exists when $\alpha_w = \alpha_{ts,I} - \alpha_{ac}$ which corresponds to a wall wavelength of $\lambda_w = 50.77mm$. The eigenfunctions in Figure 5-7 indicate a maximum response for $\lambda_w = 50.80mm$ which is in excellent agreement with theory.

Receptivity coefficients were computed using the detuned eigenfunctions at several streamwise locations. Measured receptivity coefficients and theoretical receptivity results of Choudhari [24] and Crouch [85] are presented in Figure 5-8 for various values of the detuning parameter σ'. The roughness height used to compute the theoretical receptivity coefficients [24, 85] for single-mode waviness was the first Fourier coefficient of the square wave pattern with height Δh, namely the mode corresponding to the fundamental wavenumber, α_w, with amplitude $\Delta h/\pi$. The detuning parameter σ' shifts the values of σ in Equation 5.1 to account for the finite acoustic wave speed. The detuning parameters are related by $\sigma' = \sigma + \alpha_{ac}/\alpha_{ts,I}$ where $\alpha_{ac}/\alpha_{ts,I} = 1.04\%$ for the present setup. Wiegel and Wlezien [83] applied a similar correction to their receptivity measurements. Good agreement is observed between the theoretical and experimental data. A maximum percent difference of 10% was obtained between the

maximum of the measured and theoretical receptivity coefficients, C_{max}.

5.3 Broadband disturbance evolution

In this section, data describing the evolution of the boundary-layer disturbance field are presented. Broadband rms fluctuating velocities, u, measured for three distinct acoustic forcing levels are presented in Figure 5-9. These velocity measurements were band-pass filtered at $2 < f < 400Hz$. The profiles in part (a) of the figure were obtained with the smooth model surface and with no controlled acoustic forcing (baseline setup). The rms velocity profiles resemble those of Klebanoff modes as measured by Klebanoff [54], Kendall [57, 58], and Westin *et al.* [60]. The maximum rms fluctuations occur near the midpoint of the boundary-layer thickness ($\eta \sim 2.3$). The rate of increase of the maximum rms velocity at each streamwise station is small for these low-freestream turbulent intensity levels. Data for an intermediate forcing level ($\epsilon_2 \cdot \Delta h_2$) where the flow remained laminar is given in part (b) of the figure. In the early stages ($x < 127cm$, $R < 943$), the rms profiles are indistinguishable from the profiles shown in part (a) of the figure. For measurements taken further downstream, the contributions from the T-S wave become dominant in the near-wall region and near the boundary-layer edge due the dual-lope shape of the T-S eigenfunctions. Near the midpoint of the boundary layer, the rms velocities are still consistent with those shown in part (a) for the baseline. As shown using parabolized stability theory by Herbert and Lin [124], the T-S waves and these low-frequency Klebanoff modes appear to exist independently but both may contribute to the intensity at a given frequency. The data shown in part (c) of the figure correspond to a forcing product of $\epsilon_3 \cdot \Delta h_3$ where nonlinear effects and consequent breakdown occurred. Increases of one to two orders of magnitude are observed in the maximum values of u for the streamwise distances shown, $127 < x < 203.2cm$ ($943 < R < 1205$).

The spectral content of these broadband disturbances is of interest. Power spectral densities of the fluctuating streamwise velocity, S_u, corresponding to data presented in Figure 5-9 are shown in Figure 5-10. The spectra are shown for data obtained at
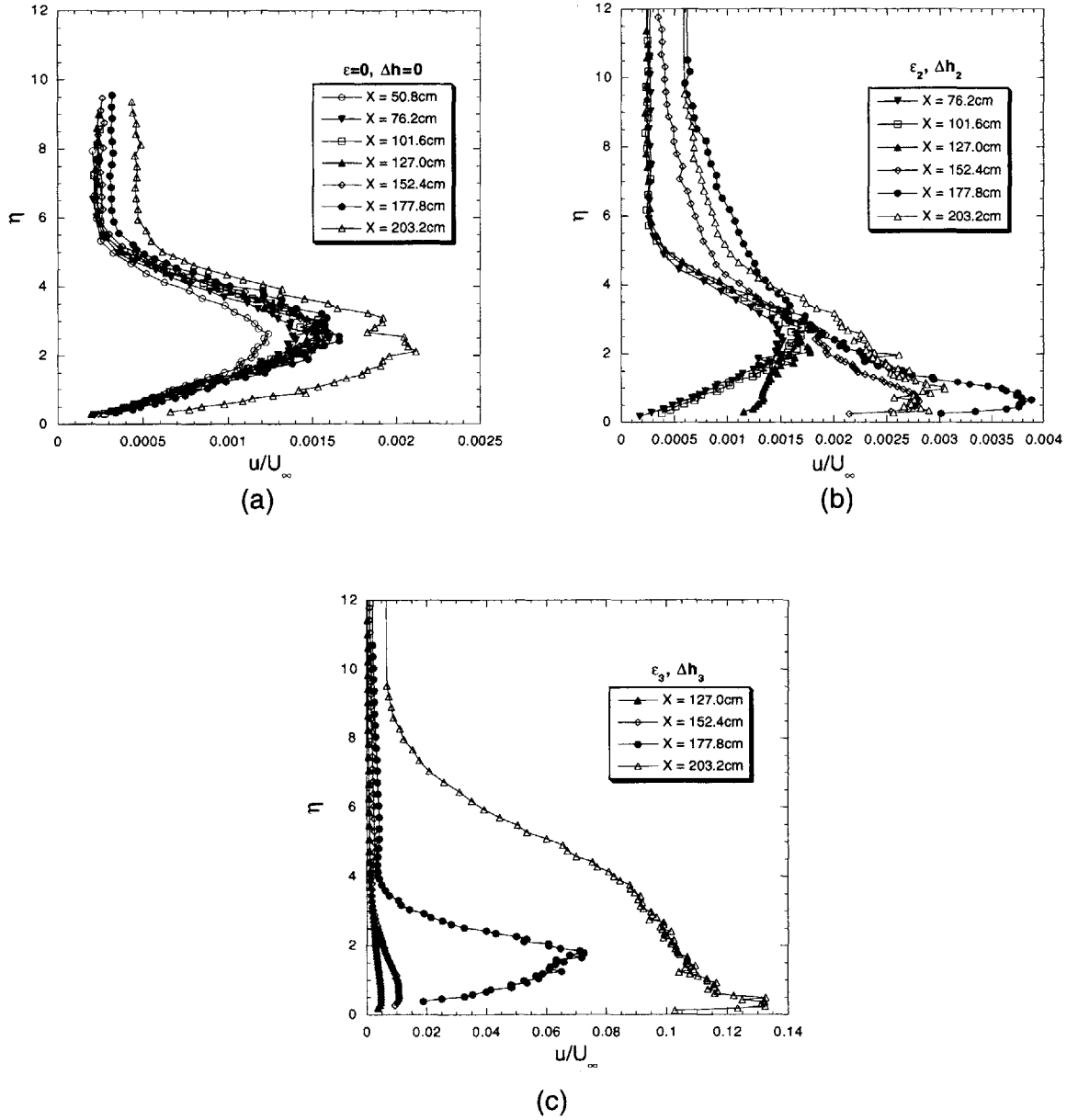
Figure 5-9: Measured broadband rms fluctuating velocity for forcing combination of (a) zero ($\epsilon = 0$, $\Delta h = 0$), (b) $\epsilon_2 \cdot \Delta h_2$, and (c) $\epsilon_3 \cdot \Delta h_3$.
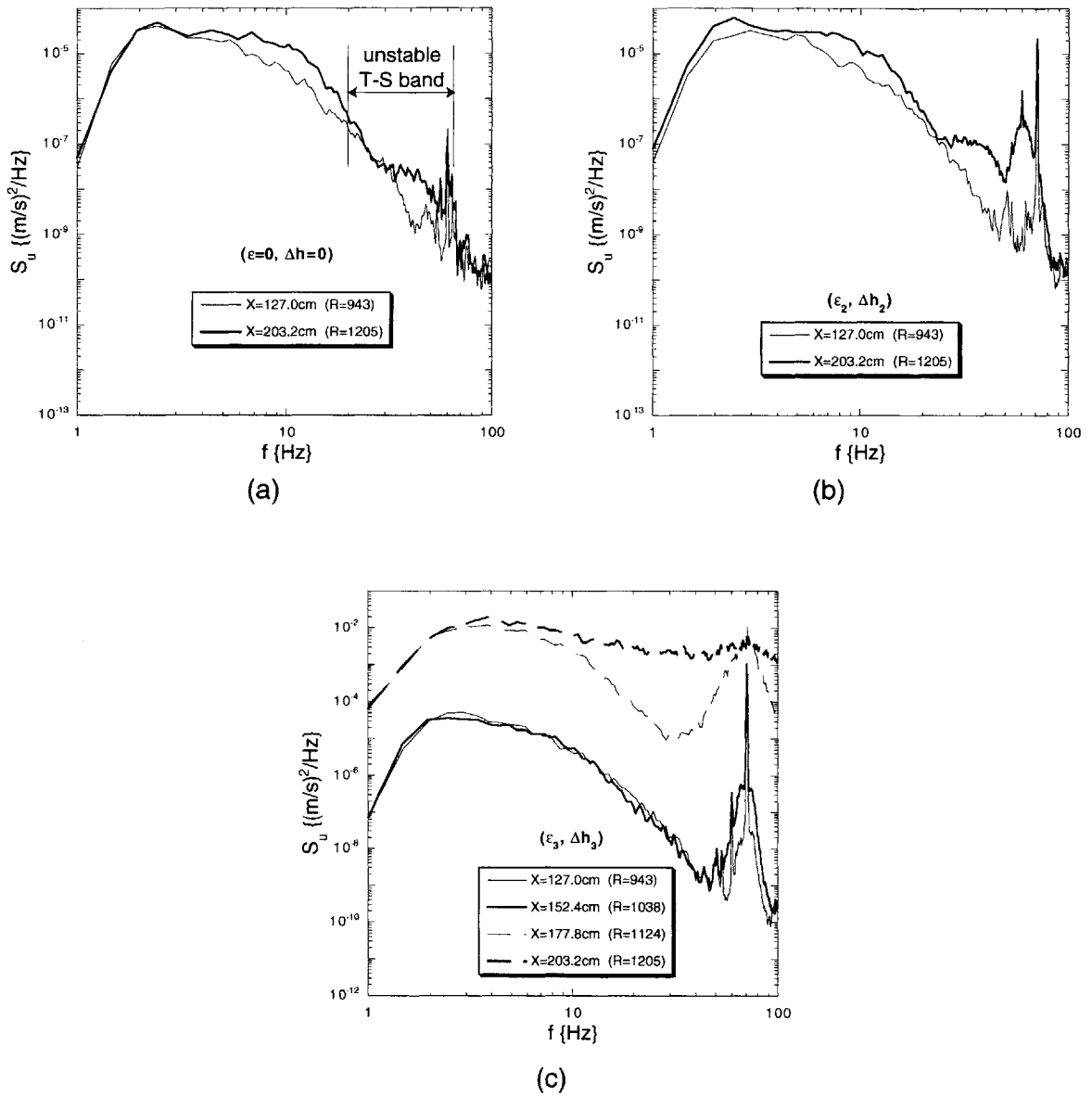
Figure 5-10: Spectra of fluctuating velocity near $\eta \approx 2.3$ for forcing product of (a) zero ($\epsilon = 0$, $\Delta h = 0$), (b) $\epsilon_2 \cdot \Delta h_2$, and (c) $\epsilon_3 \cdot \Delta h_3$.
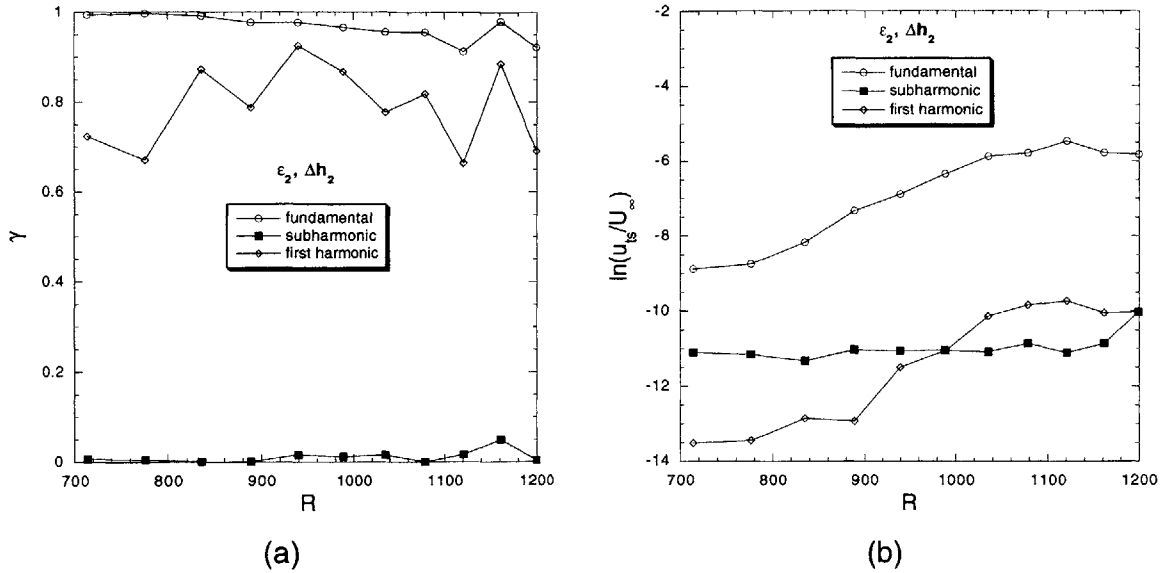
Figure 5-11: Data showing the fundamental, subharmonic, and first harmonic (a) coherence functions and (b) growth curves for $\epsilon_2 \cdot \Delta h_2$.

$\eta \approx 2.3$. The spectra shown in part (a) for the smooth model surface without acoustic forcing consist predominately of low-frequency energy, a characteristic of Klebanoff modes. Note that the spikes at $f = 60Hz$ in the spectra are a consequence of electronic noise. Modest amplification at frequencies ($f < 20Hz$) below the unstable O-S modes is observed for $x = 203.2cm$ ($R = 1205$). Amplification is also observed in the unstable band of O-S modes (see figure) for $R = 1205$. The controlled acoustic forcing is clearly evident in the spectra in part (b) of the figure. Modest amplification is again observed in the damped O-S band and significantly more amplification in the unstable band. The spectra for the largest forcing product are presented in part (c) of the figure. Significant amplification is evident in the damped T-S band due to nonlinear effects present in the transitioning boundary layer. The presence of a subharmonic mode ($f_o/2$) is not evident but spectral broadening with increasing values of Reynolds number is observed.

To investigate the coherent nature of the boundary-layer disturbance field, particular consideration was given to disturbances at the fundamental (f_o), subharmonic ($f_o/2$), and first harmonic ($2f_o$) frequencies. Figure 5-11(a) shows coherence data (between the designated instability wave and the input signal used for the acoustic

101

forcing) at the three frequencies of interest for a forcing product of $\epsilon_2 \cdot \Delta h_2$. The data were all obtained near the lower peak of the T-S wave amplitude. Significant values of coherence, γ, were obtained at the fundamental and harmonic frequencies; however, negligible coherence was observed for the subharmonic band. The data in Figure 5-11(b) are amplification curves for the data shown in part (a). The amplification of the harmonic disturbance essentially mirrors the amplification of the fundamental. As a result, the harmonic disturbance was believed to be driven by the fundamental and a result of a nonlinear self-interaction. No amplification was obtained at the subharmonic frequency. A similar set of plots is shown in Figure 5-12 for the largest forcing product, $\epsilon_3 \cdot \Delta h_3$. A sharp roll off in coherence of the fundamental and harmonic disturbances are evident for $x > 152.4cm$ ($R > 1038$) indicating the onset of significantly nonlinear behavior leading to turbulence. This is in agreement with results inferred from the amplification curves in Figure 5-4(b). Again, negligible coherence was observed at the subharmonic frequency. Referring to part (b) of the figure, it is evident from the amplification curves that the harmonic disturbance grew at rate different from that of fundamental, indicating a strong nonlinear interaction at the harmonic frequency. The growth seen at the subharmonic frequency was not due to phase-locked amplification, but a result of broadening of the spectra indicative of the breakdown process. The transition Reynolds number for this scenario was $Re_{tr} \approx 1.2 \times 10^6$ which is approximately one-third of the baseline Re_{tr} ($\approx 3.2 \times 10^6$).

Finally, broadband spectra for the intermediate and largest forcing levels are presented in Figure 5-13 for a range of streamwise locations ($76.2 < x < 203.2cm$ or $717 < R < 1205$) at wall-normal locations corresponding to the maximum of u_{ts}. For the intermediate forcing level ($\epsilon_2 \cdot \Delta h_2$) in part (a) of the figure, the energy and associated growth at the fundamental forcing frequency ($f_o = 71Hz$) and its first harmonic are clearly evident. The energy at $f = 120Hz$ is associated with electronic noise as evident from the constant streamwise amplitude. Amplification of broadband energy centered about $f \approx 60Hz$ presumably a result of the *natural* tunnel disturbance environment is discernible in the spectra for $x > 127.0cm$ ($R > 943$). Broadband amplification is also evident about $f \approx 130Hz$ for $x > 152.4cm$ ($R > 1038$). This
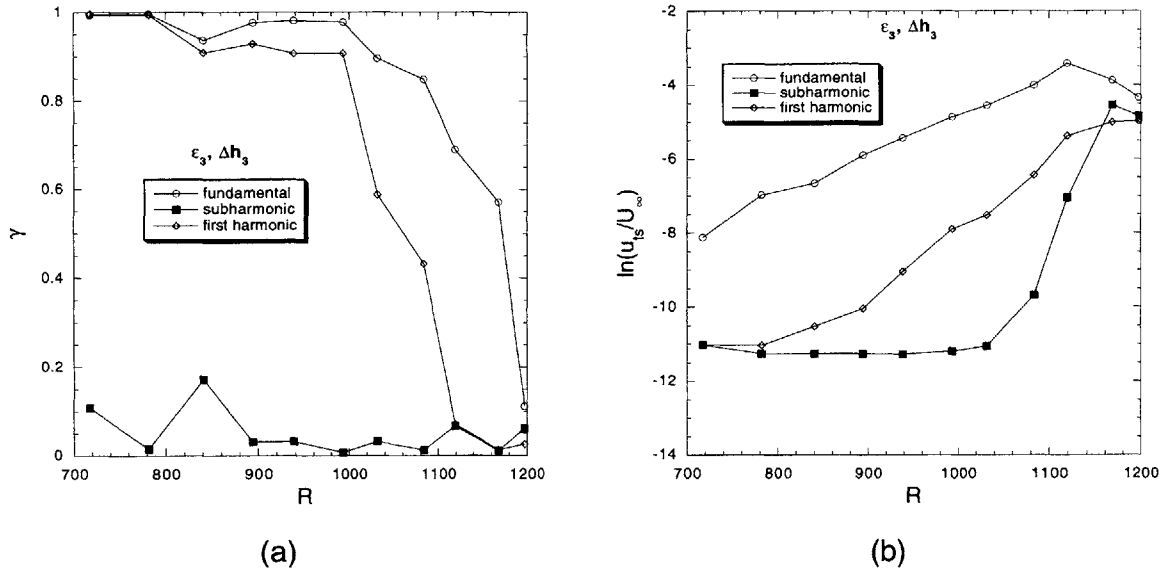
Figure 5-12: Data showing the fundamental, subharmonic, and first harmonic (a) coherence functions and (b) growth curves for $\epsilon_3 \cdot \Delta h_3$.

latter broadband energy is possibly an interaction between the forced T-S wave and the naturally occurring broadband T-S field. The situation was quite different for the largest forcing combination in part (b) of the figure. The presence of significant energy at the fundamental and higher harmonic frequencies is clearly discernible at the onset of nonlinearity ($x > 152.4cm$ or $R > 1038$). The harmonic bands broaden until a developed turbulent spectrum was obtained. Broadband amplification in the unstable O-S band of frequencies as seen for the intermediate forcing level above was not discernible in the present spectra. Similar harmonic-dominated spectra were obtained in the experiment of Breuer et al. [71]. This type of breakdown from laminar to turbulent flow in indicative of a K-type breakdown as obtained by the classical results of Klebanoff et al. [6, 7]. The selectivity of the single-frequency T-S wave, imposed by the controlled acoustic forcing and receptivity sites, created a dominant primary T-S wave with amplitudes much larger than other two- and three-dimensional modes resulting from background disturbances. The primary mode at the fundamental frequency dominated the breakdown process and resulting nonlinear interactions produced harmonics as is evident in the disturbance spectral evolution (see Figure 5-13(b)).

103
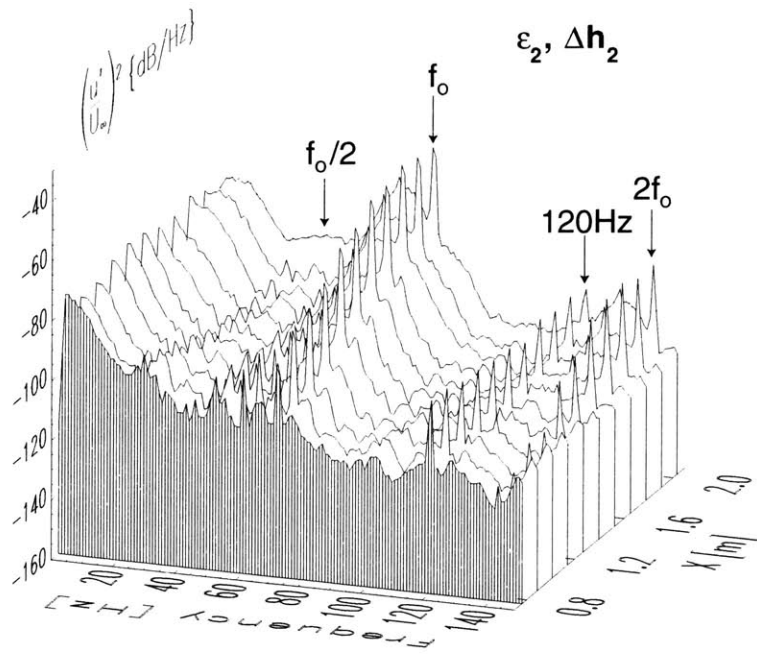
(a)
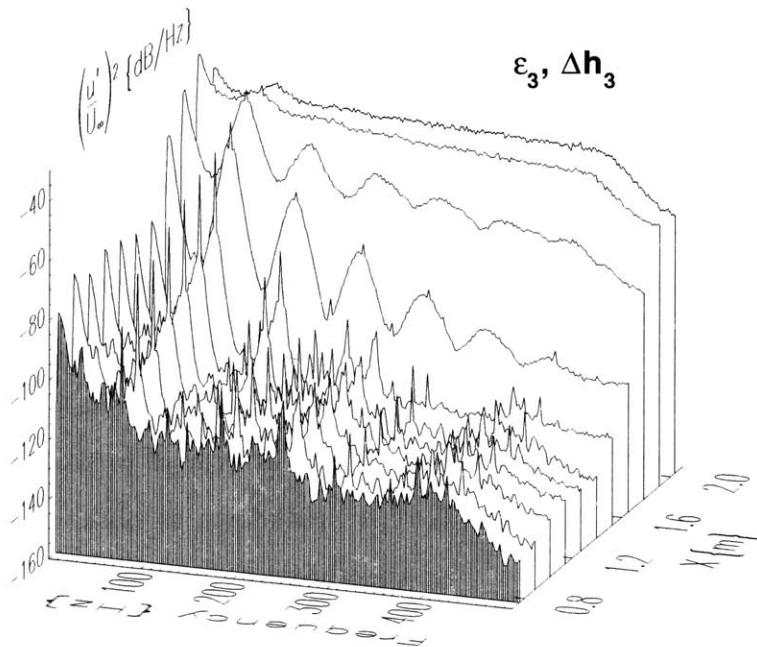
(b)

Figure 5-13: Spectra of streamwise velocity taken at $u_{ts,max}$ over a range streamwise locations for (a) $\epsilon_2 \cdot \Delta h_2$ and (b) $\epsilon_3 \cdot \Delta h_3$. The subharmonic, fundamental, and first harmonic frequencies (along with 120-Hz electronic noise) are denoted in part (a) of the figure.

5.4 Summary

Acoustic receptivity of a Blasius boundary layer under the influence of a steady wall perturbation produced by two-dimensional surface waviness (non-localized) was examined. Good agreement was observed between the measured and theoretical O-S eigenfunctions. For all combinations of $\epsilon \cdot \Delta h$ examined, the receptivity was found to be a linear function of $\epsilon \cdot \Delta h$. Excellent agreement was obtained between the measured amplification and LST amplification for cases where nonlinear effects were not observed. Good agreement between present and past [83] experimental receptivity coefficients was observed. Detuning of the resonance condition was performed by varying the wall roughness wavelength. Excellent agreement was obtained between the measured and theoretical receptivity coefficients under detuned conditions. Measured wave kinematics were in excellent agreement with LST results.

Streamwise development of the boundary-layer disturbances indicated that nonlinear effects first became apparent in the near-wall region for $u_{ts}/U_\infty \approx 1\%$ before eventually spreading throughout the shear layer. The coherence function between the forcing input and boundary-layer response decreased with an increase in nonlinear effects. Nonlinear effects became evident for a given value of the forcing product, $\epsilon \cdot \Delta h$, independent of the individual values of ϵ or Δh. Low-frequency Klebanoff modes were measured in the broadband spectra and appeared to exist independent of the T-S waves. For the largest forcing product, laminar-to-turbulent transition was observed. The breakdown was characterized by nonlinear coupling of the fundamental frequency in the form of higher harmonics, reminiscent of K-type breakdown.

Chapter 6

Results and Discussions: Oblique Disturbances

In this chapter, results are presented and discussed for the fluctuating velocity disturbances measured with oblique surface waviness (refer to Figure 2-4(b)). The author is only aware of one other experiment that considered oblique surface roughness–Zhou *et al.* [69] (see discussion in Section 1.1.3). That study was conducted for localized oblique receptivity where a single strip of tape was inclined at angles up to $\psi_w = 45°$. They inferred from their measurements at a fixed streamwise location that receptivity was reduced with increased oblique angle. They did not consider the reduced linear growth rates associated with increased obliqueness from LST. Calculations done by Crouch & Bertolotti [79] for non-localized receptivity indicated increased receptivity with increased obliqueness. This part of the study will attempt to experimentally verify the theoretical results of Crouch & Bertolotti. Characteristics of the measured T-S waves are compared with linear stability theory results where applicable. Experimental and theoretical receptivity coefficients are compared when available. All measurements in this chapter were obtained for an intermediate forcing product, namely $\epsilon_2 \cdot \Delta h_2$ (refer to Table 3.1).

ψ_{ts}\{deg\}	R_I	R_{II}	$\lambda_{ts,I,x}$\{mm\}
0	585	1129	50.245
15	583	1111	50.791
30	578	1054	52.393
45	574	949	55.519

Table 6.1: Tabulated data of lower and upper branch Reynolds numbers and streamwise T-S wavelength at Branch I for disturbance wave angle ψ_{ts} obtained from LST.

6.1 Influence of obliqueness

To investigate the influence of T-S wave obliqueness on receptivity, samples 2 and 10–12 (refer to Table 2.1) were used to generate the oblique T-S waves by the application of oblique waviness ($0 \leq \psi_w \leq 45°$). The roughness wavenumbers were selected to create a near-resonance condition at Branch I ($k_w \approx k_{ts}$) for all values of ψ_w considered. Table 6.1 tabulates the lower and upper branch Reynolds numbers and the streamwise T-S wavelength, $\lambda_{ts,I,x}$ ($= 2\pi/\alpha_{ts,I}$), at Branch I for the oblique roughnesses tested. Measured and LST T-S amplitudes at two streamwise locations, $x = 127cm$ and $152.4cm$, are presented in Figure 6-1 for the various oblique roughness angles. The LST results were normalized to match the experimental amplitudes at the maximum of u_{ts} for these profiles. Note that the outer peaks of the measured T-S profiles were underpredicted by LST. This may be due in part to nonparallel effects not accounted for in LST since nonparallelism becomes more important for three-dimensional disturbances (see Bertolotti [125]). Nevertheless, the salient features of the eigenfunction profiles were captured by LST. The appearance of a dual peak structure in the near-wall region that straddles the critical layer ($\eta \approx 1$) was observed in the oblique eigenfunctions. For two-dimensional disturbances, a single peak in the near-wall region below the critical layer was evident. As the disturbances became oblique, some residual of this peak remained with a smaller amplitude below the critical layer, and an apparent upward shift of the global maximum to a wall-
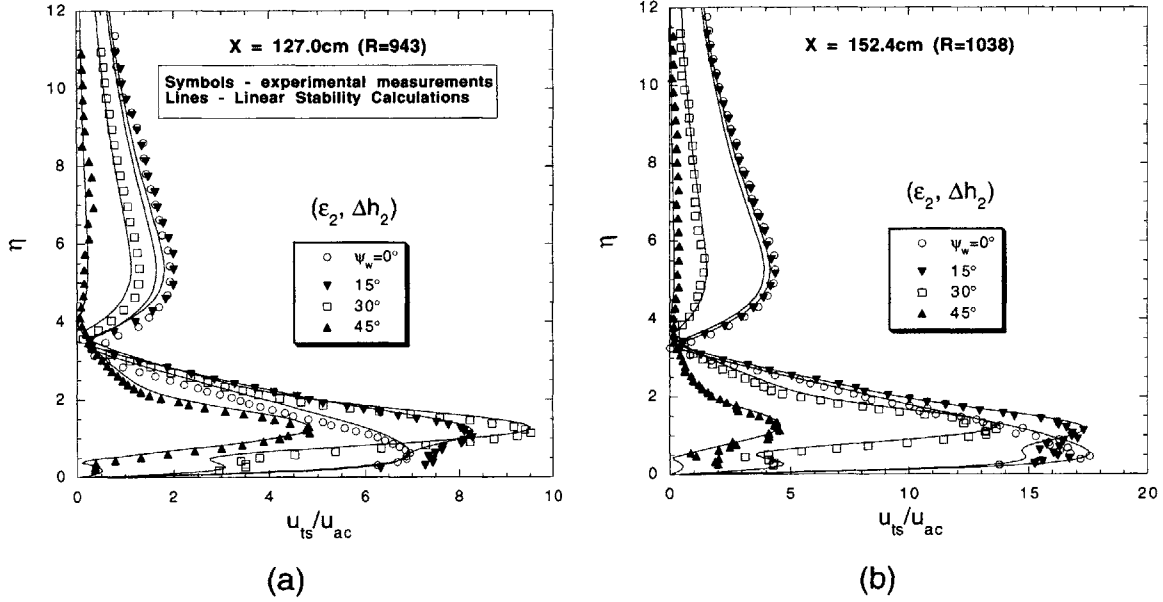
Figure 6-1: T-S amplitude profiles for various values of ψ_w at (a) $R = 943$ and (b) $R = 1038$.

normal location above the critical layer was observed. The amplitude of the apparent residual peak reduced with increased obliqueness. An upward shift of the wall-normal location of the 180° phase jump was also evident.

Figure 6-2 shows a plot of N-factor versus Reynolds number along with the experimentally measured maximum T-S amplitudes. The experimental amplitudes $(\ln(u_{ts}/u_{ac}))$ were shifted for comparison with LST. Excellent agreement was observed between the measured and LST amplification curves for small oblique angles. The agreement became less attractive for the larger oblique angles, particularly near the location of Branch II. Again, this may be a result of nonparallel effects not captured by LST.

Receptivity coefficients were calculated using the same stipulations as in Section 5.1. Figure 6-3 shows a plot of measured receptivity coefficients ($F = 55 \times 10^{-6}$) versus the roughness oblique angle along with theoretical data ($F = 56 \times 10^{-6}$) by Crouch & Bertolotti [79]. The agreement between the measured and theoretical data is good, thereby providing experimental evidence of increased receptivity with increased wave obliqueness. The error bars in the plot denote the maximum plus/minus deviation from the mean receptivity values denoted by the symbols. The
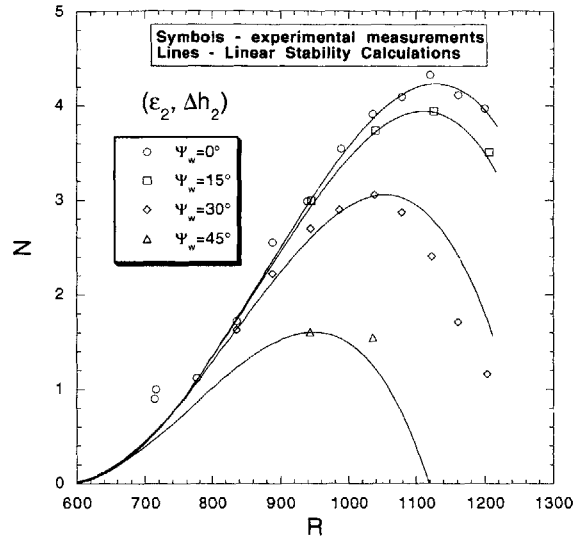
Figure 6-2: Streamwise amplification data for various values of ψ_w.
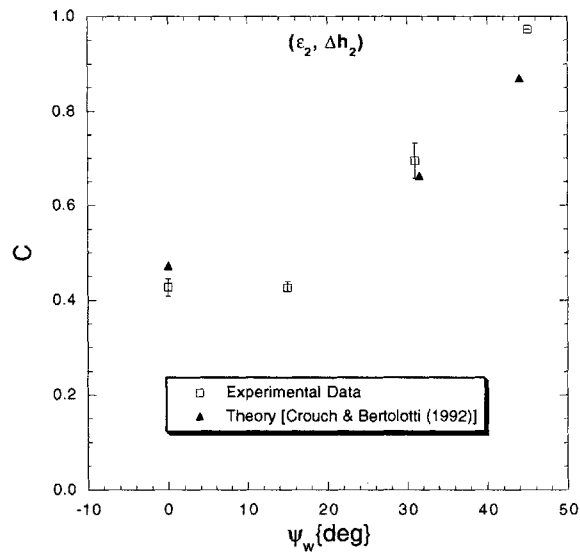
Figure 6-3: Measured ($F = 55 \times 10^{-6}$) and theoretical ($F = 56 \times 10^{-6}$) receptivity coefficients as a function of oblique roughness wave angle ψ_w.
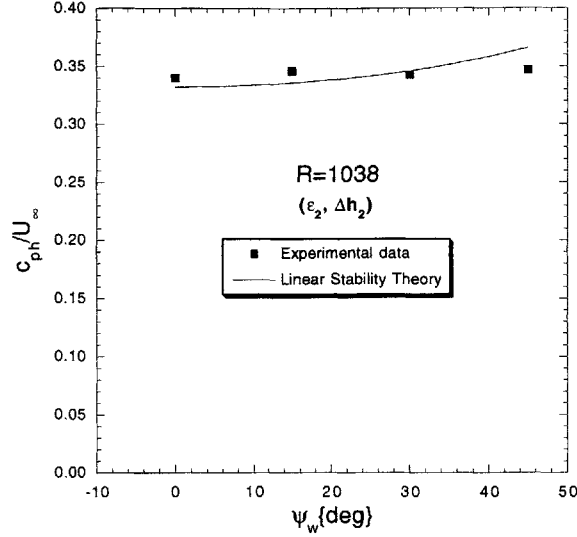
Figure 6-4: T-S wave phase speed, c_{ph}/U_∞, versus roughness oblique angle ψ_w.

confidence level for the value of the experimental receptivity coefficient at $\psi_w = 45°$ is not very high since only one data point was used to obtain the value of C. This may be one explanation for the large difference observed there along with the fact that the mode-interaction theory used to compute the theoretical values of C degrades with three-dimensionality which is largely attributable to nonparallel effects [79]. T-S wave kinematics were inferred for the oblique waviness following the same procedure as was done for the two-dimensional waviness. A plot of the T-S wave phase speed for varying roughness oblique angles is shown in Figure 6-4. The phase speed from LST is denoted by the line in the figure. The overall agreement between the measured and LST c_{ph}/U_∞ is within the experimental uncertainty of the measurements.

6.2   The effect of detuning

Results are presented here for the detuned condition of an oblique wave ($\psi_{ts} = 30°$). As in the two-dimensional case, detuning was achieved by varying the streamwise wall roughness wavenumber α_w while maintaining a fixed spanwise wavenumber β_w ($\beta_w = \beta_{ts,I}$). This resulted in an incremental change of the roughness oblique angle ψ_w for each value of α_w selected. Samples 11 and 13 − 16 (refer to Table 2.1) were

111
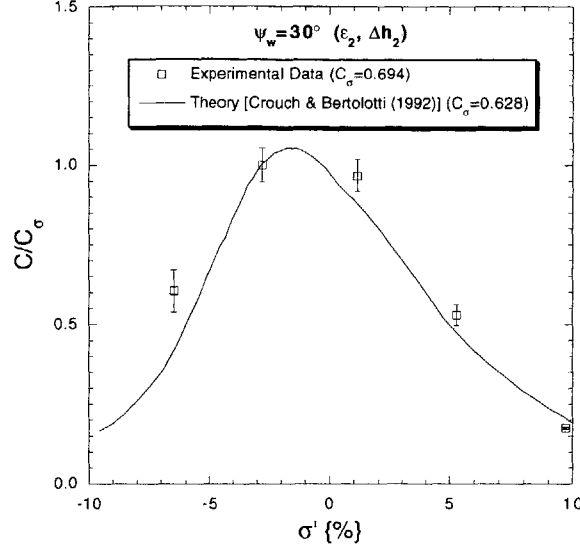
Figure 6-5: The effect of detuning on measured ($F = 55 \times 10^{-6}$) and theoretical ($F = 56 \times 10^{-6}$) oblique receptivity coefficients for $\psi_{ts} = 30°$.

used as receptivity sites for this portion of the experiment.

The issue of a finite wave speed was again addressed. The resonant condition for a downstream-traveling freestream acoustic wave is given as $(\alpha_w, \beta_w) = (\alpha_{ts,I} - \alpha_{ac}, \beta_{ts,I})$ [29] since $\beta_{ac} = 0$ here. The value of the streamwise T-S wavelength at Branch I computed using LST is $\lambda_{ts,I,x} = 52.393mm$. Using the same definition of the detuning parameter σ defined in Equation 5.1 and the shifted detuning parameter $\sigma' = \sigma + \alpha_{ac}/\alpha_{ts,I}$ where $\alpha_{ac}/\alpha_{ts,I} = 1.08\%$, the experimental effect of detuning on the receptivity coefficient was then compared to incompressible theoretical predictions. Figure 6-5 shows a plot of the measured receptivity along with theoretical calculations by Crouch and Bertolotti [79]. The measured receptivity coefficients are normalized by C_σ, the maximum measured value corresponding to $\sigma' \approx -2.8$. The theoretical coefficients are normalized by the theoretical value of C at the same σ', which is not the maximum theoretical coefficient. Good agreement is again obtained between the measured and theoretical values. A maximum percent difference of less than 10% was obtained between the measured maximum and the corresponding theoretical value of the receptivity coefficients, C_σ.

112
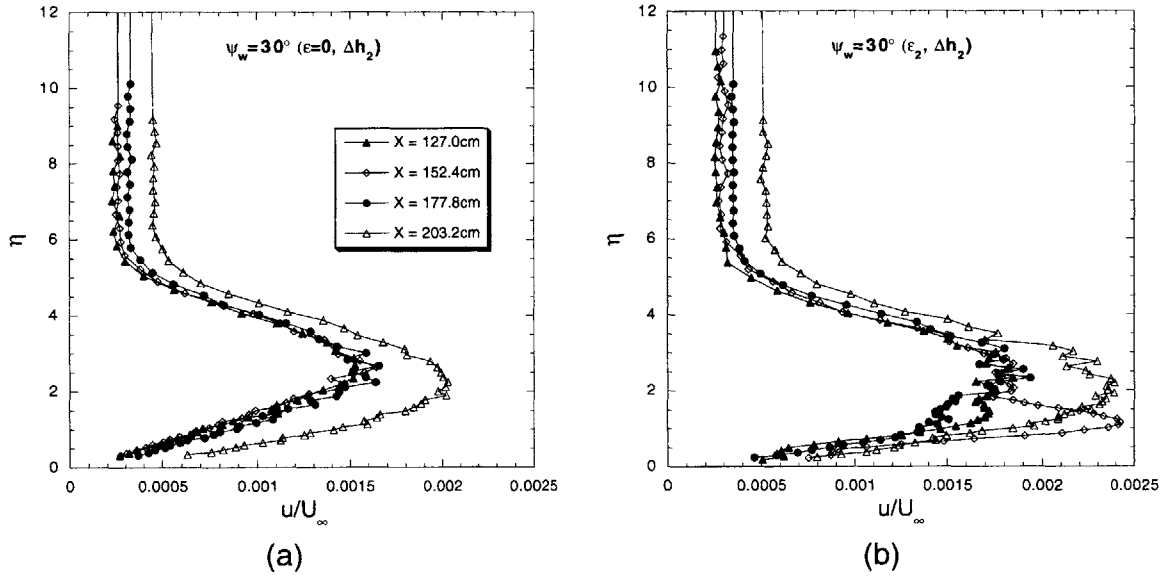
Figure 6-6: Measured broadband rms fluctuating velocity with $\psi_w = 30°$ for (a) $\epsilon = 0$ and Δh_2 and (b) $\epsilon_2 \cdot \Delta h_2$.

6.3 Broadband disturbance evolution

The evolution of oblique boundary-layer disturbances with respect to broadband and phase-locked data was investigated. The findings were similar to those for the two-dimensional disturbances with intermediate forcing, $\epsilon_2 \cdot \Delta h_2$. As a representative case, all data presented in this section were obtained with wall-roughness oblique angles of $\psi_w = 30°$. Broadband rms fluctuating velocity data obtained with and without controlled acoustic forcing are presented in Figure 6-6. The rms velocity profiles in part (a) of the figure again resemble those of Klebanoff modes. Note the remarkable similarity between the profiles in Figure 6-6(a) with no acoustic forcing and step height Δh_2 and those for the baseline setup in Figure 5-9(a). Again, very little amplification was observed in the range of streamwise locations shown except at the last station, $x = 203.2cm$ ($R = 1205$), for $\epsilon = 0$ and Δh_2. The rms velocity profile for $\epsilon_2 \cdot \Delta h_2$ in part (b) of the figure appear to have a broader lobe. This was due primarily to the contribution of energy in the excited T-S wave at the larger wall-normal location associated with the upward shift of the maximum of u_{ts}. As for the two-dimensional disturbance case, both the T-S wave and Klebanoff low-frequency mode appear to exist independently.
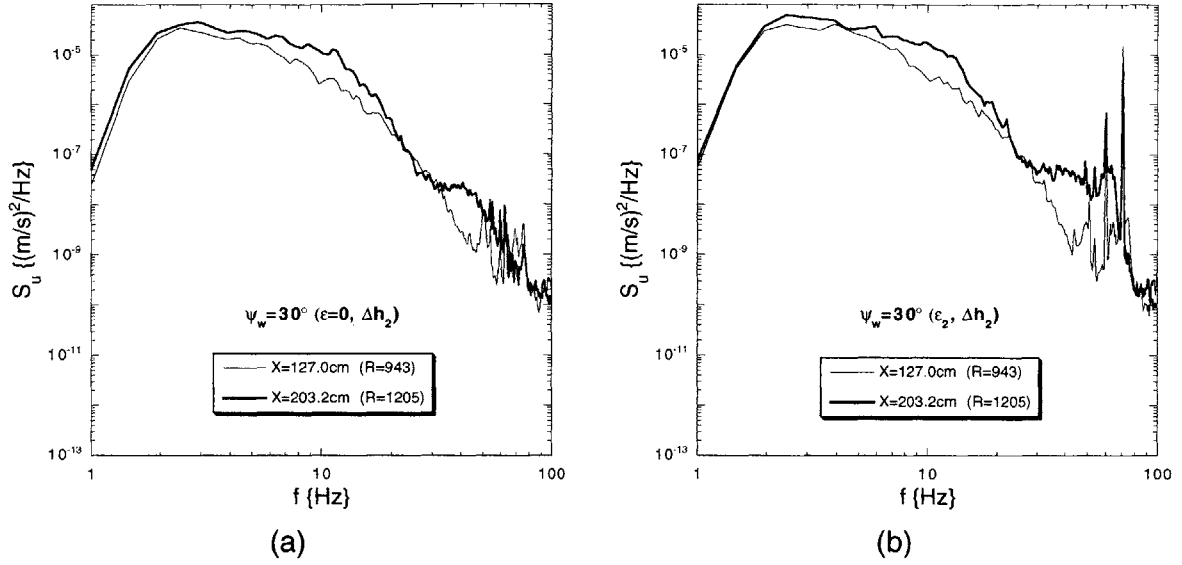
Figure 6-7: Spectra of fluctuating velocity with $\psi_w = 30°$ near $\eta \approx 2.3$ for (a) $\epsilon = 0$ and Δh_2 and (b) $\epsilon_2 \cdot \Delta h_2$.

The power spectral densities corresponding to data in the Figure 6-6 are presented in Figure 6-7. The spectral data shown were acquired at $\eta \approx 2.3$. Again, the spectra in Figures 6-7(a) and (b) show a striking resemblance to those shown in Figures 5-10(a) and (b). Modest amplification is observed for frequencies below the unstable O-S modes for $x = 203.2cm$ ($R = 1205$). Amplification is also evident in the unstable O-S band.

The coherent nature of the boundary-layer disturbance field was investigated by tracking the disturbances at the fundamental (f_o), subharmonic ($f_o/2$), and first harmonic ($2f_o$) frequencies as done previously. Figure 6-8(a) shows coherence data obtained at the wall-normal locations corresponding to the maximum u_{rms} for the three frequencies of interest. Measurable values of γ, the coherence function, were only obtained at the fundamental and first harmonic frequencies. The corresponding amplitude curves are shown in Figure 6-8(b). The amplitude curve of the harmonic tracks (mirrors) the curve of the fundamental implying a relatively weak nonlinear self-interaction. No significant amplification was obtained at the subharmonic frequency. The results acquired here were very similar to those obtain for two-dimensional waviness with the intermediate forcing product, $\epsilon_2 \cdot \Delta h_2$, as discussed in Section 5.3.
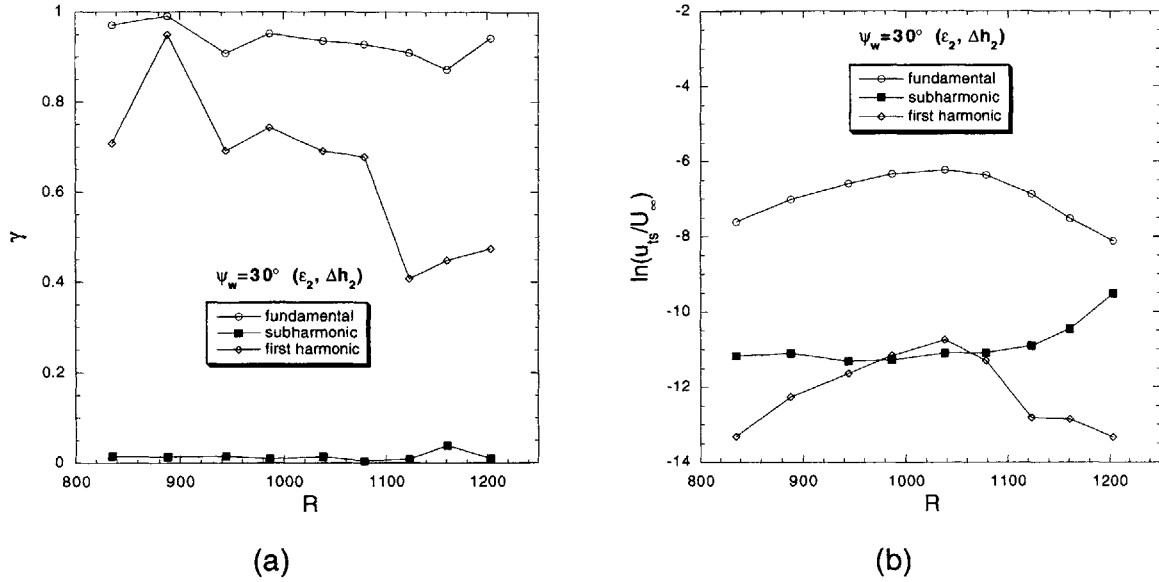
Figure 6-8: Streamwise distribution of the measured (a) coherence function, γ (between the measured disturbance velocity and input forcing signal), and (b) disturbance velocity amplitude, $\ln(u_{ts}/U_\infty)$, for the fundamental (f_o), subharmonic $(f_o/2)$, and first harmonic $(2f_o)$ frequencies with $\psi_w = 30^\circ$ for $\epsilon_2 \cdot \Delta h_2$. Measurements acquired at $U/U_\infty \approx 0.39$ which corresponds to $y/\delta \approx 0.24$ for the undisturbed profile.

Broadband spectra for the rms velocity data presented in Figure 6-8 are given in Figure 6-9. The energy bands associated with the fundamental and first harmonic frequencies are clearly evident in the figure along with the electronic noise at $f = 120Hz$. Amplification of broadband energy centered about $f \approx 60Hz$, similar to the intermediate forcing case for two-dimensional waviness, is discernible in the spectra for $x > 127.0cm$ $(R > 943)$ but at smaller amplitudes. The broadband amplification about $f \approx 130Hz$ realized for the two-dimensional case is not evident in the spectra. This is believed to be due to the reduced energy amplitudes of both the forced T-S wave and the naturally occurring broadband T-S field.

6.4   Summary

Acoustic receptivity of a Blasius boundary layer under the influence of a steady wall perturbation produced by oblique surface waviness (non-localized) was examined. Measurements were obtained for a single forcing combination, $\epsilon_2 \cdot \Delta h_2$. Excellent
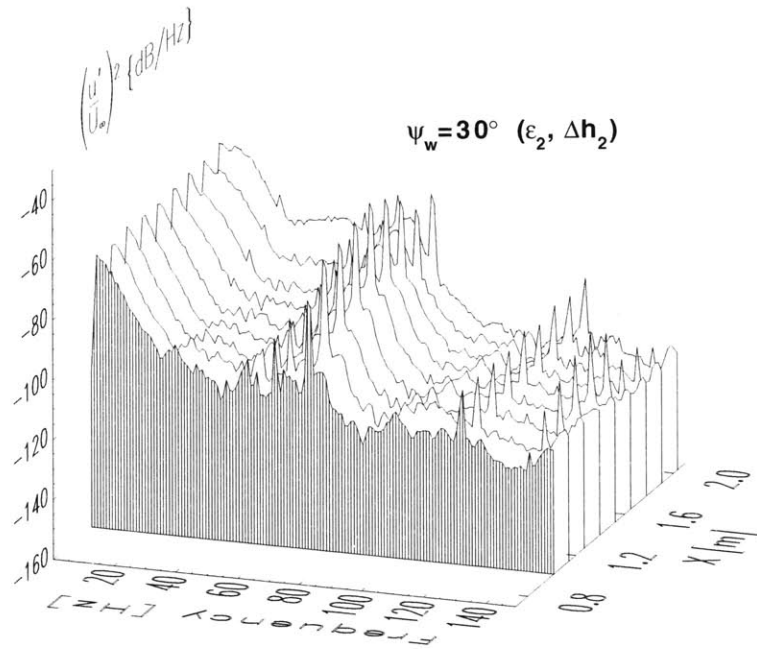
Figure 6-9: Spectra of streamwise velocity taken at $u_{ts,max}$ $(U/U_\infty \approx 0.39)$ over a range of streamwise locations with $\psi_w = 30°$ for $\epsilon_2 \cdot \Delta h_2$.

qualitative agreement was observed between the measured and theoretical O-S eigenfunctions. A fundamental difference was observed between the two-dimensional and oblique T-S amplitudes in both measurements and LST results. An upward shift of the maximum of the T-S amplitude with T-S wave obliqueness was observed. An apparent dual peak structure in the near-wall region that straddles the critical layer was evident in the oblique O-S eigenfunctions. Good agreement was observed between the measured and LST amplification curves. The agreement degraded with increasing obliqueness of the T-S wave particularly near Branch II, presumably due to nonparallel effects not captured by LST. Good agreement was observed between the measured and theoretical receptivity coefficients as a function of oblique wave angle. The data provided experimental evidence of increased receptivity with increased wave obliqueness. Detuning was examined for an oblique wave with $\psi_{ts} = 30°$ by varying the streamwise wall roughness wavenumber. Excellent comparison with theory was observed. Comparison of the measured wave kinematics and LST results was good.

116

Significant nonlinear effects were not observed in the streamwise development of the boundary-layer disturbances examined. Disturbances resembling low-frequency Klebanoff modes were measured. The broadband disturbance evolution showed a remarkable (qualitative) similarity to the evolution of the two-dimensional disturbance with the same forcing product, $\epsilon_2 \cdot \Delta h_2$. The major differences between the evolution of the oblique and two-dimensional waves were the reduced amplifications and the upstream movement of the location of Branch II for the oblique wave.

Chapter 7

Results and Discussions: Three-Dimensional Disturbances (Oblique Transition)

Unlike the previous two chapters where emphasis was placed on the measurement of receptivity coefficients, this chapter addresses a transition mechanism involving a pair of oblique O-S modes $(f, \pm \beta)$ in the frequency/spanwise-wavenumber space (see discussion in Section 1.1.4). Oblique transition was initiated by generating a pair of oppositely-oriented oblique O-S modes with the use of non-localized three-dimensional (3-D) surface waviness patterns $(\alpha_w, \pm \beta_w) = (\alpha_{ts,I}, \pm \beta_{ts,I})$ depicted in Figure 2-4(c). Results presented in this chapter were obtained using samples $17 - 19$ (refer to Table 2.1) where the oblique roughness angles were $\psi_w = \pm 30°$. The influence of acoustic forcing level, u_{ac}, and roughness height, Δh, on oblique transition was examined by conducting measurements using the matrix arrangement shown in Table 3.1. A detailed view of the 3-D pattern along with coordinate description is shown in Figure 7-1. The freestream flow is in the direction of x denoted in the figure. The origin of the spanwise coordinate z was taken as the tunnel centerline. Because the centerlines of the tunnel and roughness patterns did not coincide, a new normalized spanwise coordinate ζ was introduced with an offset $(15.2mm)$. The spanwise coordinate was defined as $\zeta = (z + 15.2)/\lambda_{w,z}$ where z is in units of millime-

119
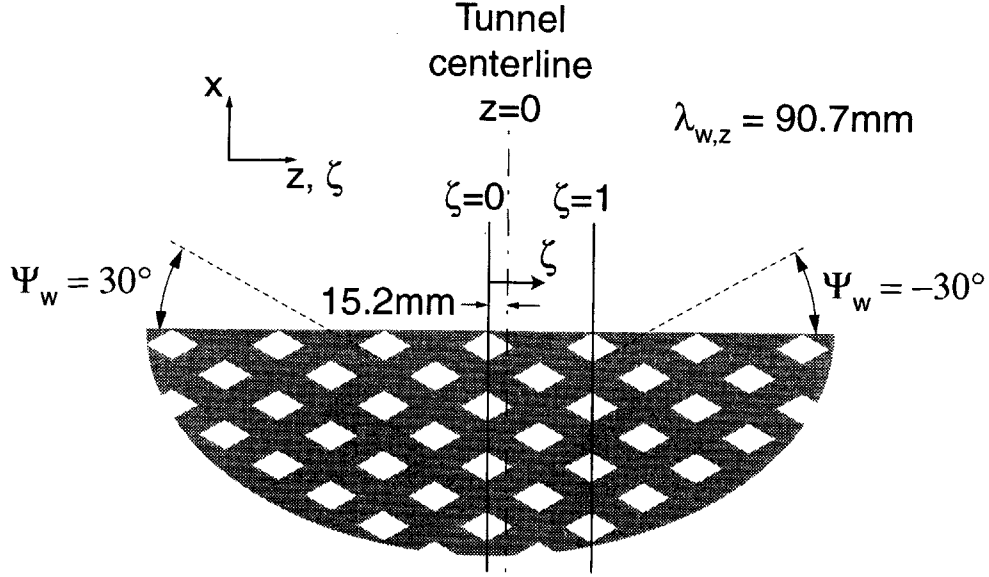
Figure 7-1: Detailed view of three-dimensional surface roughness pattern (flow from bottom to top).

ters and $\lambda_{w,z}$ is the spanwise wavenumber of the roughness ($\lambda_{w,z} = 90.7mm$). This gives a value of $\zeta = 1$ for one spanwise wavelength. Branch I of the primary waves, $(f/f_o, \pm\beta/\beta_w) = (1, \pm1)$, was located near the streamwise midpoint of the surface roughness. To generate the pair of oblique O-S waves, a downstream-traveling acoustic wave was utilized in addition to the wall roughness to enhance the receptivity mechanism.

7.1 Peak-valley structure of disturbance field

Streamwise velocity measurements were acquired along the spanwise direction near the wall-normal locations corresponding to the maximum amplitude of the 3-D disturbance eigenfunction. The spanwise traverses typically extended approximately one spanwise wavelength of the wall roughness ($\lambda_{w,z} = 90.7mm$). Spanwise profiles of the narrow-band rms streamwise disturbance velocity, u_t, were acquired for a freestream acoustic level of ϵ_2 on the smooth model surface, $\Delta h = 0$. These measurements were obtained to characterize the background spanwise disturbance environment which is a function of the damping screens in the tunnel. Plots showing the spanwise distri-
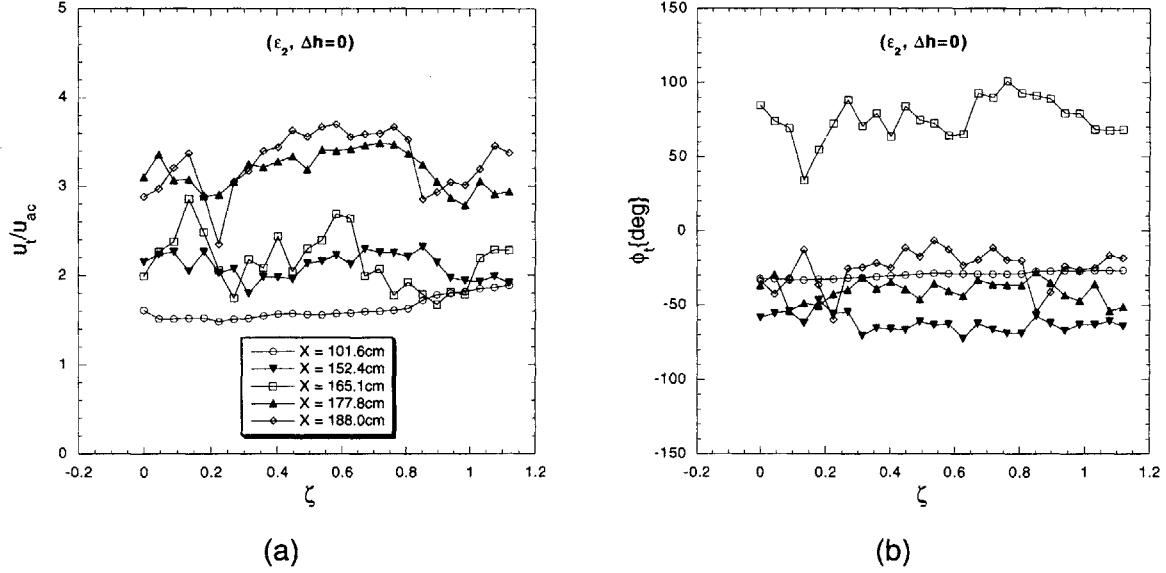
Figure 7-2: Root-mean-square narrow-band velocity at f_o, (a) amplitude and (b) phase, measured along spanwise coordinate ζ at various streamwise locations for a forcing combination of zero (ϵ_2, $\Delta h = 0$). Measurements acquired at a wall-normal location corresponding to $U/U_\infty \approx 0.40$.

bution of u_t and ϕ_t, the disturbance phase angle, are presented in Figure 7-2. The profiles were taken at a wall-normal location near the maximum of u_t over a streamwise distance of $101.6 < x < 188.0cm$ ($838 < R < 1157$). The reader is reminded to refer to Table 3.2 for tabulated data of x versus R. No significant structures in the spanwise u_t distribution were observed as is evident in part (a) of the figure. Similarly, spanwise variations in ϕ_t were not evident as indicated in part (b) of the figure. The results demonstrate a relatively two-dimensional disturbance field at f_o over the limited spanwise extent of the measurements.

Results with the 3-D surface roughness will first be presented for a scenario where laminar breakdown was not observed. The forcing combination used to obtain these results was $\epsilon_3 \cdot \Delta h_1$. Figure 7-3 shows a plot of mean streamwise velocity data versus the spanwise location, acquired at a wall-normal location near the maximum of u_t. The mean flow structure was very similar to the classical work of Klebanoff et al. [7]. The location of the peaks and valleys resulting from the streaks are indicated in the figure. The peaks and valleys are defined as regions corresponding to U deficits (maximum u_t) and U surpluses (minimum u_t), respectively. The distorted base flow
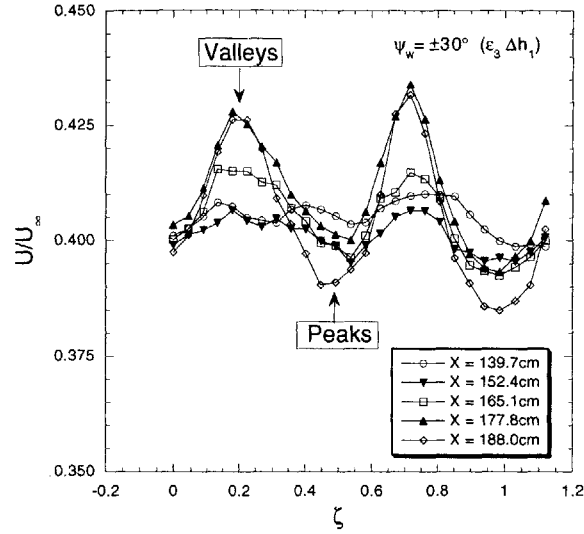
Figure 7-3: Mean streamwise velocity measured along spanwise coordinate ζ at various streamwise locations for $\epsilon_3 \cdot \Delta h_1$. Measurements were acquired at $U/U_\infty \approx 0.40$ for $\zeta = 0$ corresponding to $y/\delta \approx 0.25$ for the undisturbed profiles.

resulted from the streaky structures believed to be produced by the *lift-up* effect of the stationary vortex system $(f/f_o, \pm\beta/\beta_w) = (0, \pm 2)$ induced by the nonlinear interaction of the primary modes $(1, \pm 1)$. The amplitude of the mean flow distortion was seen to increase with downstream location. Data for the disturbance amplitude and phase at f_o corresponding to this configuration are presented in Figure 7-4. The peaks and valleys are again indicated in part (a) of the figure. The spanwise extent of the peaks were larger than that for the valleys. The valleys became narrower with downstream distance. A $180°$ phase shift in the disturbance phase ϕ_t was observed between adjacent peaks as seen in part (b) of the figure.

Measurements were also obtained using a larger forcing combination $(\epsilon_3 \cdot \Delta h_3)$ for a scenario where laminar breakdown occurred. A plot of the mean streamwise velocity is given in Figure 7-5. Significant three dimensionality associated with low- and high-speed streaks was observed compared to the results in Figure 7-3. The mean velocity increased by as much as 75% in the valley regions. As before for the case with $\epsilon_3 \cdot \Delta h_1$, the mean flow distortions were biased to higher velocities. The corresponding narrow-band disturbance velocity amplitudes are presented in Figure 7-6. For $x \leq 133.4cm$ ($R \leq 968$), the spanwise distribution of u_t was consistent with results obtained for

122

(a)

(b)
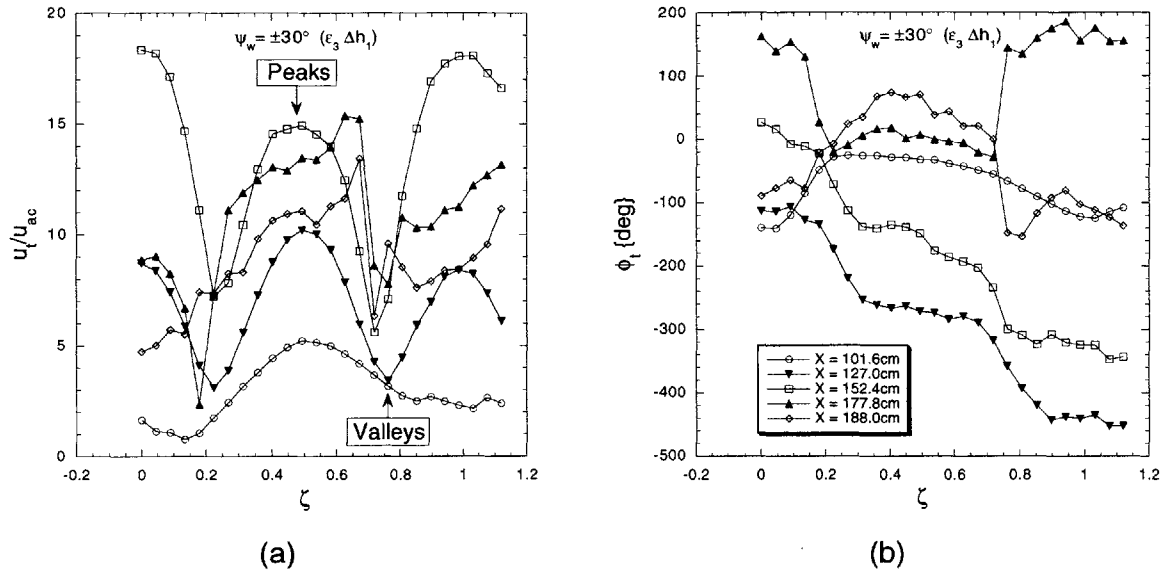
Figure 7-4: Root-mean-square narrow-band velocity at f_o, (a) amplitude and (b) phase, measured along spanwise coordinate ζ at various streamwise locations for $\epsilon_3 \cdot \Delta h_1$. Measurements acquired at $y/\delta \approx 0.25$ for the undisturbed profiles.
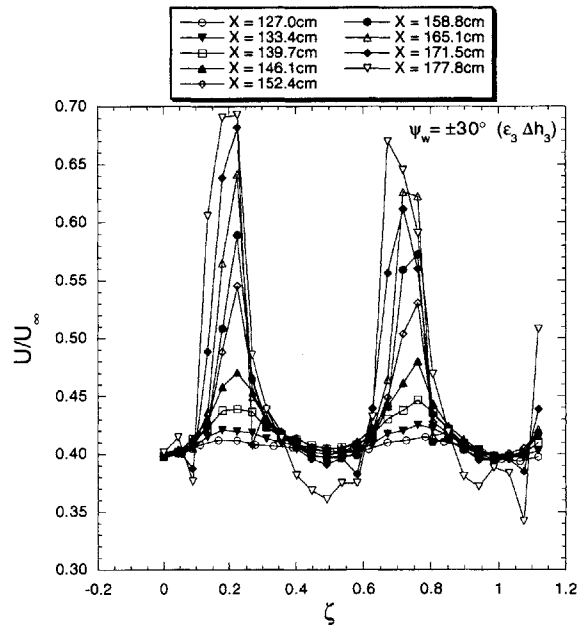
Figure 7-5: Mean streamwise velocity measured along spanwise coordinate ζ at various streamwise locations for $\epsilon_3 \cdot \Delta h_3$. Measurements were acquired at $U/U_\infty \approx 0.40$ for $\zeta = 0$ which corresponds to $y/\delta \approx 0.25 - 0.29$ for the undisturbed profiles.
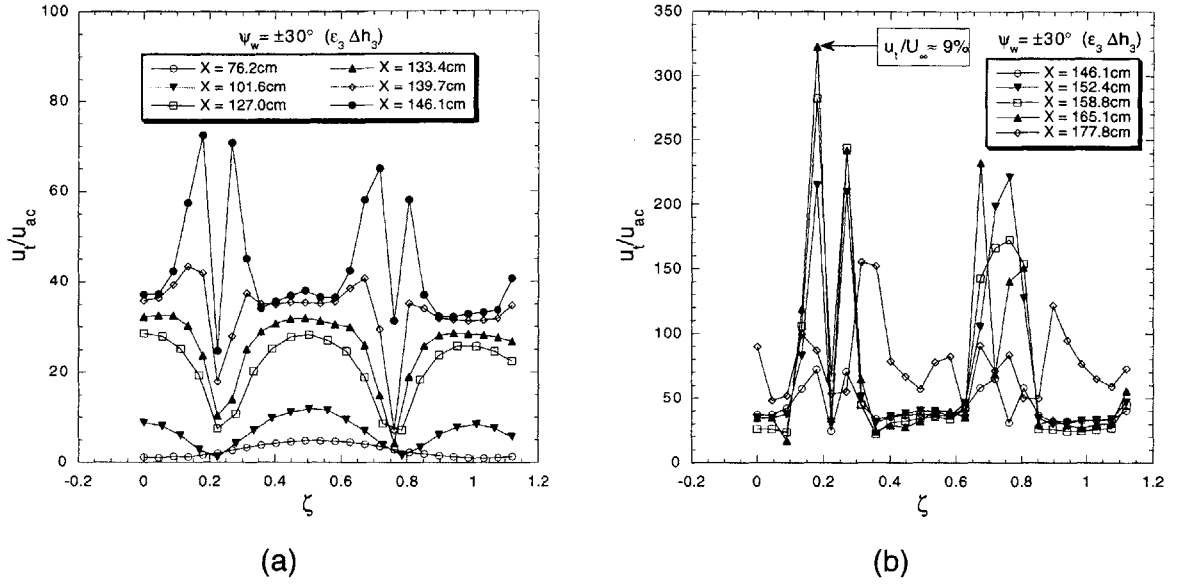
Figure 7-6: Root-mean-square narrow-band velocity at f_o measured along spanwise coordinate ζ at various streamwise locations for $\epsilon_3 \cdot \Delta h_3$. Measurements were acquired at $U/U_\infty \approx 0.40$ for $\zeta = 0$ which corresponds to $y/\delta \approx 0.25 - 0.29$ for the undisturbed profiles.

$\epsilon_3 \cdot \Delta h_1$ (refer to Figure 7-4(a)). The spanwise disturbance distribution took on a different character at $x = 139.7cm$ ($R = 991$). An upwelling of u_t on both sides of the peaks was observed. Explosive growths in the value of u_t at these spanwise locations were realized with streamwise distance as evident in parts (a) and (b) of the figure. Velocity fluctuations as large as $u_t/U_\infty \approx 9\%$ were measured in these surveys. Similar observations regarding the phase shift of 180° were evident in ϕ_t between adjacent peaks for this configuration (not shown) relative to the configuration for $\epsilon_3 \cdot \Delta h_1$ (refer to Figure 7-4(b)). To understand the origin of this instability, closely-spaced measurements were acquired over approximated half the spanwise wavelength. Data are presented in Figure 7-7 for $x = 146.1cm$ ($R = 1015$). In part (a) of the figure, the measured mean velocity data and a corresponding polynomial regression curve fit are presented. The regression fit gives a good representation of the measured data except near the end points. The regression fit was computed to facilitate the calculation of the mean spanwise velocity gradient $dU/d\zeta$. The spanwise distributions of the fluctuating velocity and absolute spanwise gradient are presented in part (b) of the figure. The spanwise locations of the maximum value of $|dU/d\zeta|$ coincide with the

124
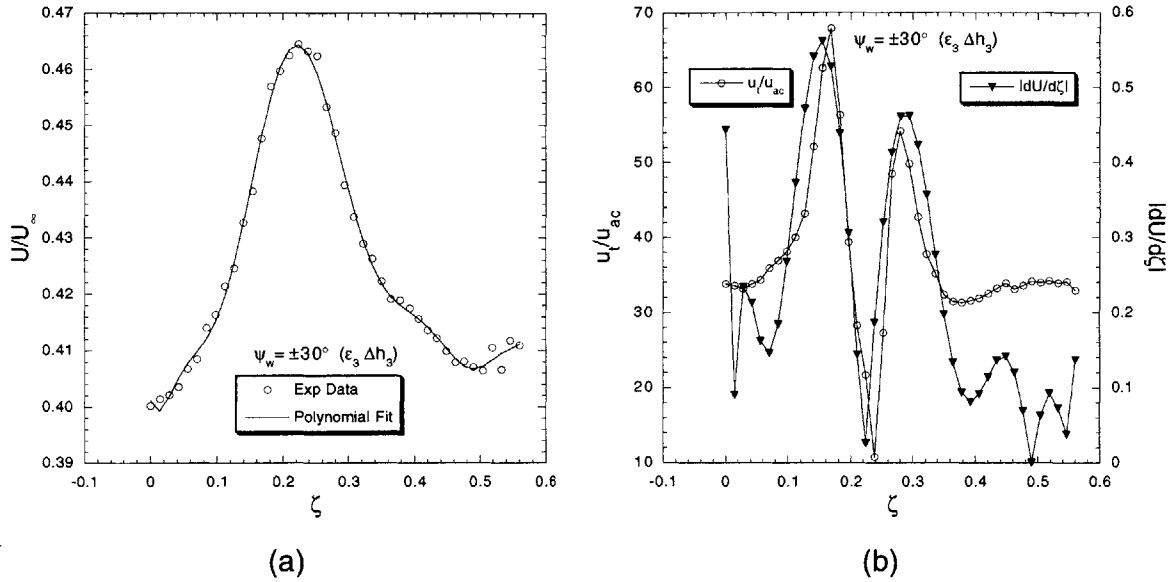
Figure 7-7: Detailed spanwise distribution of the measured (a) mean velocity and (b) rms narrow-band velocity at $x = 146.1cm$ ($R = 1015$) for $\epsilon_3 \cdot \Delta h_3$. A curve of the polynomial regression fit to the measured data and its derivative are also included in the plots. Data obtained at $y/\delta \approx 0.26$ for the undisturbed profiles.

locations of large velocity fluctuations. The magnitude of u_t also scales with $|dU/d\zeta|$. This explosive instability appeared to be driven by the mean spanwise gradient $dU/d\zeta$. Similar finding were reported by Elofsson & Alfredsson [105] for oblique transition in plane Poiseuille flow.

Power spectral densities at three spanwise locations are presented in Figure 7-8 corresponding to the data presented in Figure 7-7. The locations $\zeta = 0$ and $\zeta = 0.25$ correspond to a peak location and valley location, respectively. The location $\zeta = 0.17$ represents a location of strong spanwise mean shear. All the spectra were dominated by the energy at the forcing frequency f_o and higher harmonics. One notable feature is the appearance of energy in the subharmonic frequency band not observed for the laminar breakdown with 2-D roughness (refer to Figure 5-13(b)). More on the observed energy in the subharmonic frequency band will be addressed later in this chapter in Section 7.2. For the spectra at the peak location ($\zeta = 0$), the energy bands at the fundamental and higher-harmonic frequencies are narrower than the corresponding bands for the valley location. In contrast, the spectra results (not shown) obtained upstream of the observed upwelling of u_t in the spanwise profile

125
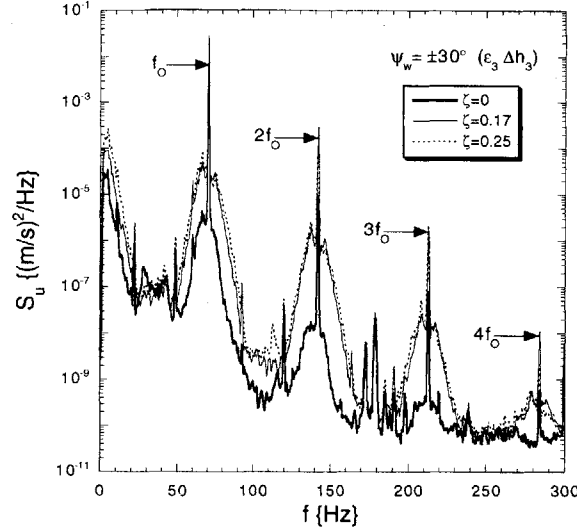
Figure 7-8: Power spectral density of the fluctuating streamwise velocity at $x = 146.1cm$ ($R = 1015$) for three spanwise locations ($\zeta = 0$, 0.17, and 0.25). Data obtained at $y/\delta \approx 0.26$ for the undisturbed profiles.

($x \leq 133.4cm$ or $R \leq 968$) indicated broader energy bands at the fundamental and harmonic frequencies for the peaks locations. The largest broadband rms velocity was shifted from the peak locations for x distances upstream of the upwelling in the u_t spanwise profiles to spanwise locations corresponding to maximum spanwise mean shear further downstream.

Distortion to the base flow was also examined with wall-normal measurements of the streamwise velocity field at spanwise locations corresponding to peaks and valleys. Mean velocity measurements acquired under the influence of acoustic forcing and/or wall roughness were used to compute a velocity deficit, $\delta(U/U_\infty)$, relative to the unperturbed flow (smooth surface without acoustic forcing). The velocity deficit is defined as $\delta(U/U_\infty) = U_p/U_\infty - U_{ref}/U_\infty$ where U_p and U_{ref} denote the perturbed and unperturbed (reference) velocities, respectively. The reference velocity profiles were first linearly interpolated to the wall-normal coordinate, η, of the perturbed profiles before the subtraction was performed. The U_{ref} profiles were obtained along the tunnel centerline at the desired streamwise locations (refer to profiles in Figure 4-4). Profiles of the velocity deficit for various forcing combinations and spanwise locations are presented in Figure 7-9. The measurements shown were all acquired at
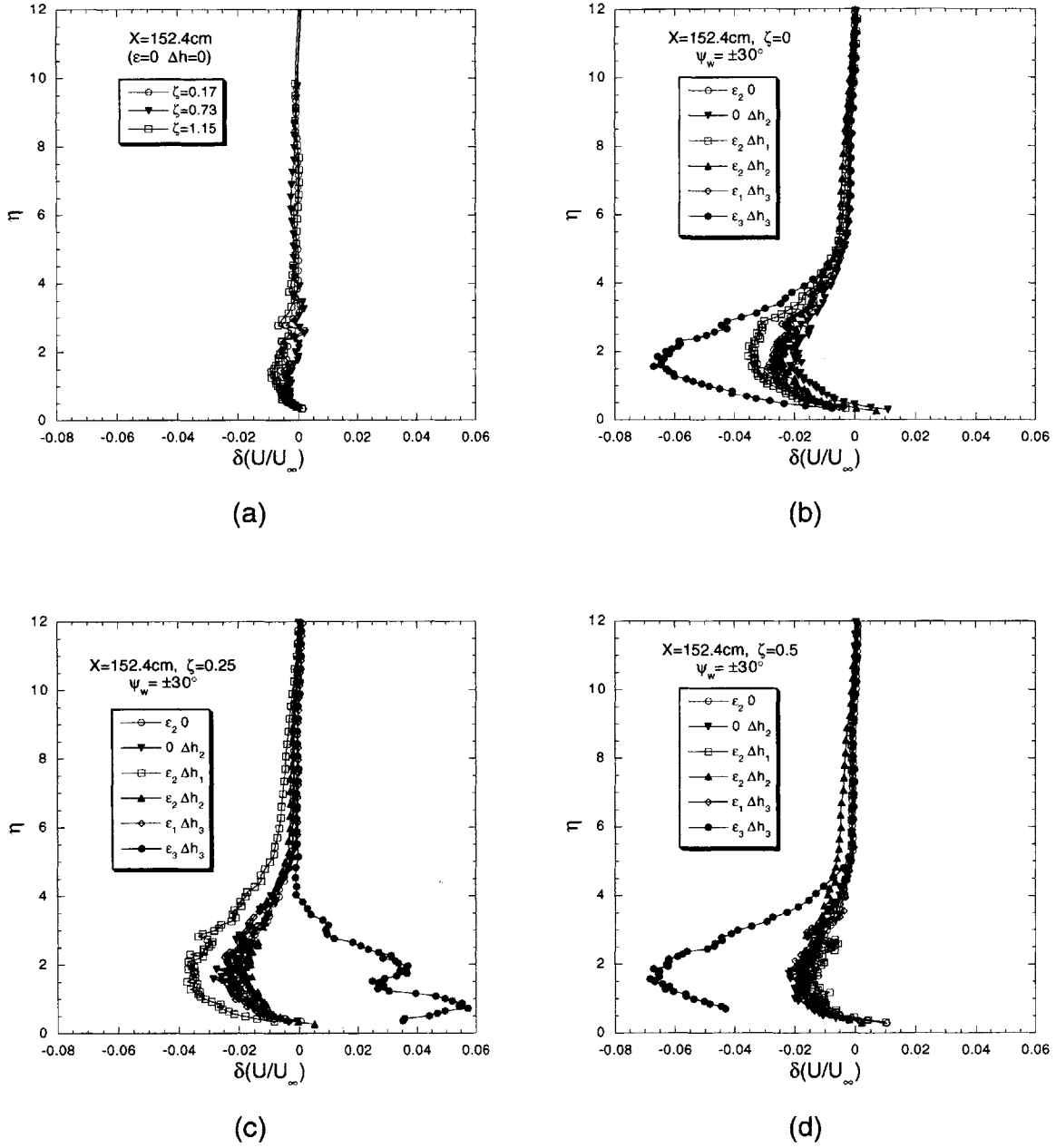
Figure 7-9: Wall-normal profiles of the velocity deficit for various forcing combinations acquired at $x = 152.4cm$ ($R = 1038$) and selected spanwise locations.

$x = 152.4cm$ ($R = 1038$). Results on the smooth plate with no controlled forcing ($\epsilon = 0$, $\Delta h = 0$) are presented in part (a) of the figure for three spanwise locations over a range of approximately one spanwise wavelength. The velocity deficits were all within 1% of the U_∞. The velocity deficits in parts (b) of the figure were obtained at a peak location ($\zeta = 0$). Measurable velocity deficits were observed for all forcing combinations even for cases where either the acoustic forcing level, ϵ, or the roughness height, Δh, was zero. Velocity deficits as large as 7% of U_∞ were detected at $\eta \approx 1.7$ for the largest forcing combination ($\epsilon_3 \cdot \Delta h_3$). For forcing combinations that did not lead to breakdown, velocity deficits were typically less than 3% of U_∞. For the valley region shown in Figure 7-9(c), velocity deficits were again observed for all forcing combinations that did not lead to laminar breakdown. However, for the largest forcing combination that culminated into breakdown, a velocity surplus of approximately 6% was realized at a wall-normal location of $\eta \approx 0.7$. Velocity surpluses as large as 25% of U_∞ were measured for streamwise distances of $x = 188.0cm$ (data not shown). The profiles in part (d) of the figure correspond to another peak location at a spanwise distance of $\lambda_{w,z}/2$ from the data shown in part (b). Similar trends in the velocity deficits at the peak locations were observed as expected. The velocity-deficit profiles of the perturbed boundary layer suggest a tendency towards wall-normal inflectional velocity profiles, $U(\eta)$, except for the velocity profiles acquired in the valley regions downstream of the onset of laminar breakdown.

Three-dimensional disturbance eigenfunctions were obtained from the wall-normal measurements of the streamwise velocity. Example plots of the amplitude and phase of the measured eigenfunction are shown in Figure 7-10 along with the measured and computed oblique O-S eigenfunction for $\psi_w = 30°$ at $x = 127cm$ ($R = 943$). The spanwise location of the measured 3-D disturbance profile was obtained at $\zeta = 0$, the point of intersection of the oblique wall waviness. The data presented in the figure were all obtained with the same forcing product, $\epsilon_2 \cdot \Delta h_2$. Note that the 3-D eigenfunction presented here represent the phase-locked velocity fluctuation at f_o for all values of the spanwise wavenumber β. The O-S and 3-D amplitude eigenfunctions in Figure 7-10(a) show remarkable qualitative agreement. The maximum amplitude of

128
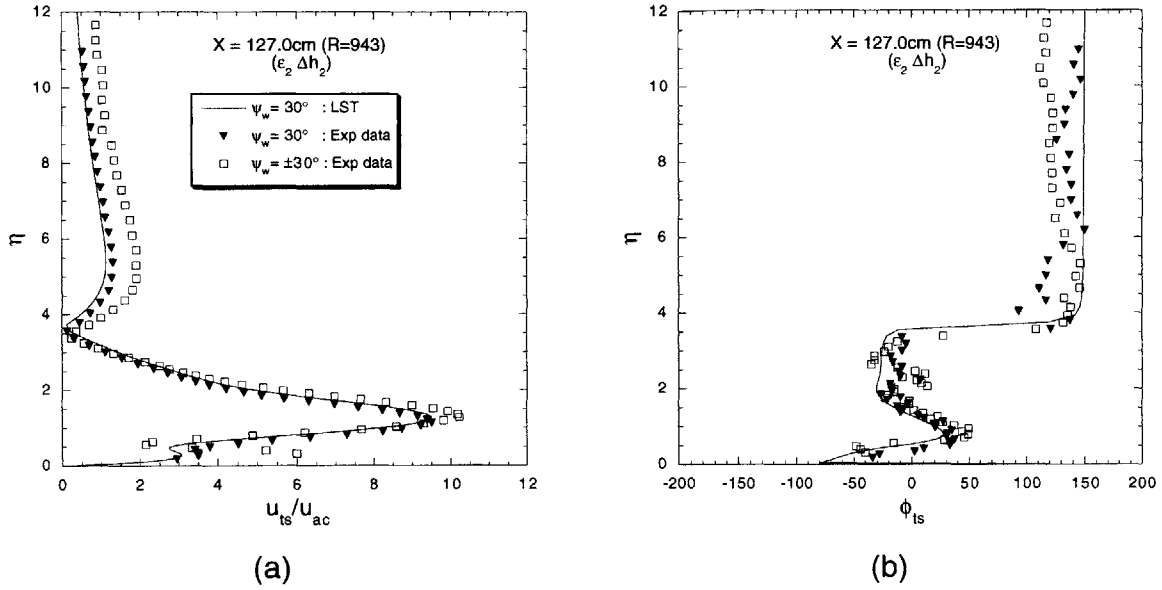
Figure 7-10: Comparison of measured eigenfunctions, (a) amplitude and (b) phase, for oblique and 3-D surface roughness (3-D eigenfunction acquired along $\zeta = 0$). The computed O-S eigenfunction for the oblique wave is also shown.

the 3-D eigenfunction is approximated 15% larger than the maximum for the oblique O-S mode. This larger value of the maximum amplitude was possibly due to the contributions from other spanwise modal components. The phases of both measured eigenfunctions and LST results are in excellent agreement as depicted in Figure 7-10(b). The near-wall features of the phase reversal were captured in the measurements for $\eta < 2$. The rms eigenfunction amplitudes normalized by u_{ac} and h are presented in Figure 7-11 for various values of the forcing product. The outer peak of the normalized profiles indicate a near linear response with forcing product. The same linear response was not observed for the inner peak (maximum). One plausible explanation may be related to the strength of the vertical vorticity component resulting from the distorted mean flow. The streamwise velocity contains a strong component due to the vertical vorticity. The inner peak of the eigenfunctions has been shown by Cohen *et al.* [100] to be affected by the vertical vorticity component which is driven by the wall-normal mean shear. Since the mean shear and consequently the vertical vorticity tend to zero outside the boundary layer, the outer peak of the eigenfunctions are not significantly influenced by the vertical vorticity component.

129
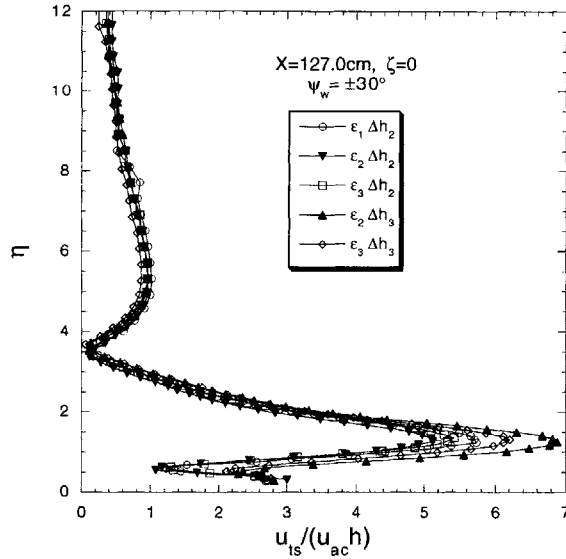
Figure 7-11: Normalized 3-D disturbance amplitudes for various values of u_{ac} and Δh. Measurements taken along $\zeta = 0$.

As per the discussion in Section 3.6.1, wave kinematics were computed using closely-spaced velocity data measured over a streamwise distance of approximately $1.5\lambda_{w,x}$. Measurements were acquired at $\zeta = 0$ (peak) and $\zeta = 0.25$ (valley) at a fixed wall-normal location near the maximum amplitude of the 3-D eigenfunction. The disturbance phase speeds measured were in the range of $0.34 < c_{ph}/U_\infty < 0.37$ $(\bar{c}_{ph}/U_\infty = 0.35)$ at a streamwise location corresponding to $R \approx 1038$ for all possible forcing combinations. The wall-normal location of the critical layer $(\eta \approx 1)$ was just below the location corresponding to the maximum amplitude of the 3-D eigenfunction $(\eta \approx 1.2)$. Phase speed results are consistent with those measured with oblique wall waviness (refer to Figure 6-4).

7.2 Disturbance evolution

Broadband rms fluctuating velocities, u, were measured with the 3-D wall roughness. Results obtained for the low-frequency Klebanoff modes were very similar to those for the 2-D and oblique wall roughnesses (refer to Sections 5.3 and 6.3) and consequently will not be presented. As a measure of the streak amplitude, ΔU was defined as

130
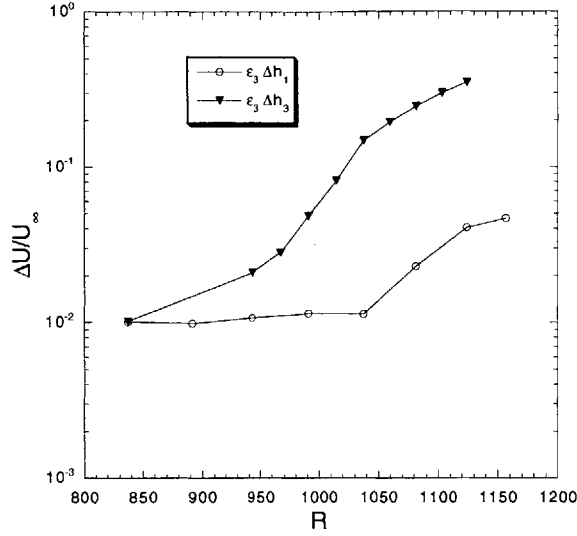
Figure 7-12: Streamwise distribution of the measured streak amplitude, ΔU, at the indicated forcing combinations. Measurements were acquired at wall-normal locations corresponding to $U/U_\infty \approx 0.40$ at $\zeta = 0$.

the difference between the maximum (valley location) and minimum (peak location) value of U in the spanwise profile at a given streamwise and wall-normal location. A plot of the streak amplitude versus streamwise distance is presented in Figure 7-12 for two forcing combinations, $\epsilon_3 \cdot \Delta h_1$ and $\epsilon_3 \cdot \Delta h_3$. The spanwise U measurements were obtained at wall-normal locations near the maximum eigenfunction amplitude at f_o. Streak amplification was observed for both scenarios for large downstream distances. For the configuration where the flow remained laminar ($\epsilon_3 \cdot \Delta h_1$), ΔU remained relatively constant over the range $838 < R < 1038$ ($101.6 < x < 152.4cm$) and streak amplification was observed further downstream ($R > 1038$). For the largest forcing product where nonlinear breakdown occurred, streak amplification was observed for all measurements. The growth rate was seen to increase at $R = 968$ ($x = 133.4cm$) near the first occurrence of the upwelling of u_t on the sides of peaks in the spanwise profiles. The growth rate then decreased further downstream at $R = 1038$ ($x = 152.4cm$). It is interesting to note that the streak amplitudes measured at the first streamwise position ($R = 838$ or $x = 101.6cm$), which was approximately $21cm$ downstream of the trailing edge of the roughness samples, were the same for both forcing combinations (factor of 4 difference in $\epsilon \cdot \Delta h$). Since the stationary

131

streamwise vortex system $(0, \pm 2)$ was responsible for the formation of the streaks, this suggests that the streamwise vortex system produced by the nonlinear interaction of the primary modes $(1, \pm 1)$ were of equal strengths for both forcing combinations. The equal strengths of the vortex system at $R = 838$ may imply that the initial nonlinear interaction reached a saturated state by $R = 838$ (sufficient data are not available for upstream locations). This leads one to conclude that the significant difference observed in the streak amplification rates for $R > 838$ was primarily due to nonlinear interactions of nonstationary boundary-layer disturbances assuming some threshold amplitude of the $(0, \pm 2)$ mode was satisfied.

It was therefore instructive to examine the disturbance evolution in the frequency-wavenumber plane. This was done by conducting spanwise surveys of the streamwise velocity at wall-normal locations near the maximum eigenfunction amplitude at f_o for several x-locations. The spanwise surveys extended $101.6mm$ $(0 < \zeta < 1.12)$ with a spacing of either $4.1mm$ or $5.1mm$. Temporal Fourier transforms of the velocity were computed at each data point and the energy in a $2\text{-}Hz$ bandwidth about the desired frequencies $(f_o, 2f_o, 3f_o, \cdots)$ were computed. Spanwise energy profiles were then constructed for each desired frequency using the energy computed from the temporal spectra and the corresponding spanwise locations. Spatial Fourier transforms were then applied to the spanwise energy profiles to obtain the modal components of the velocity, $u_t(f, \beta)$. Figure 7-13 presents results obtained for the forcing combinations discussed above. Modal velocities are presented for (i) the primary oblique modes – $(1,1)$ – , (ii) the first set of nonlinear interactions – $(0,0)$, $(0,2)$, $(2,0)$, and $(2,2)$ –, and (iii) selected higher-order interactions – $(1,3)$, $(3,1)$, and $(3,3)$. Note that the $\pm$ on the spanwise wavenumber component was dropped. For the configuration where the flow remained laminar $(\epsilon_3 \cdot \Delta h_1)$, the modal data in part (a) of the figure indicate a dampening of all the significant nonstationary modes after some initial amplification. However, when laminar breakdown was present $(\epsilon_3 \cdot \Delta h_3)$, all nonstationary modes were seen to amplify significantly as expected (see part (b) of the figure). Excellent qualitative agreement between the measured modal velocities in Figure 7-13 and the simulation results of Joslin et al. [103] was observed as described below. For the simu-

132
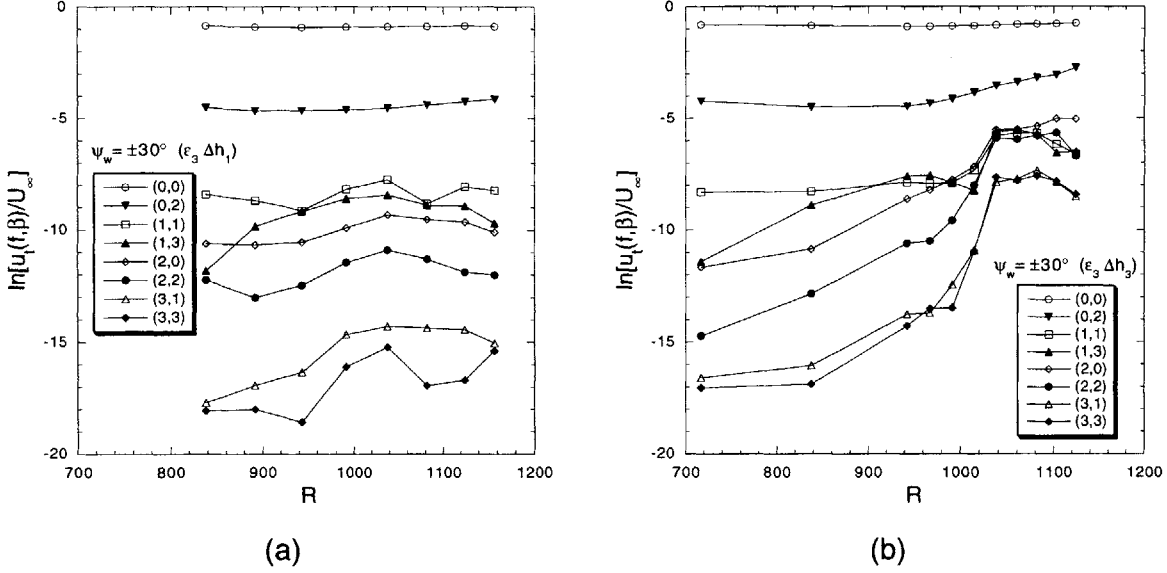
Figure 7-13: Modal velocity distribution of the measured streamwise velocity for (a) $\epsilon_3 \cdot \Delta h_1$ and (b) $\epsilon_3 \cdot \Delta h_3$. The mode designations given in the plot legends are $(f/f_o, \beta/\beta_w)$. Spanwise measurements acquired at wall-normal locations corresponding to $U/U_\infty \approx 0.40$ at $\zeta = 0$.

lation where the flow remained laminar, all nonstationary modes where first amplified and then dampened. The streamwise vortex mode $(0,2)$ was seen to have an initial amplification significantly larger than the other modes due to the self interaction of the primary mode $(1,1)$ in the simulations. The fact that the current experimental disturbance input did not contain a $(0,2)$ mode, one can infer that the same was true for the current results in that the $(0,2)$ mode was more than an order of magnitude larger than any other nonstationary mode. The $(1,3)$ mode, which resulted from a nonlinear interaction of the $(0,2)$ and $(1,1)$ modes, was seen to overtake the first set of excited modes, namely the $(2,0)$ and $(2,2)$ modes, in both the simulation and experiment. For the simulation results with laminar breakdown, the $(0,2)$ mode is again the dominant higher-order mode as in the experimental results. The nonstationary modes now grow with significantly larger growth rates than the case where the flow remained laminar.

For comparison, the modal velocity data for the $(1,1)$, $(0,2)$, and $(1,3)$ modes are presented in Figure 7-14 for both forcing combinations. The open symbols represent data for $\epsilon_3 \cdot \Delta h_1$ and closed symbols for $\epsilon_3 \cdot \Delta h_3$. The relative amplitudes between the

133
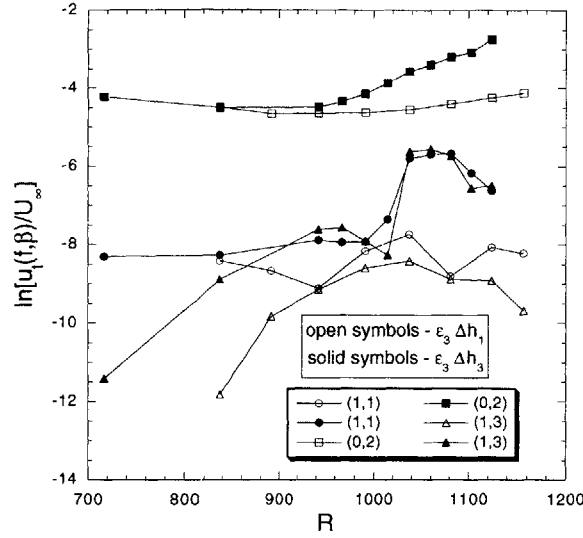
Figure 7-14: Comparison of the measured modal velocity distributions for the $(1,1)$, $(1,3)$, and $(0,2)$ modes. Data taken from Figure 7-13 for $\epsilon_3 \cdot \Delta h_1$ and $\epsilon_3 \cdot \Delta h_3$.

corresponding modes are clearly illustrated in the figure. The primary oblique $(1,1)$ mode at $R = 838$ for both forcing products was approximately equal indicating that the $(1,1)$ modes may be in a saturated state. The modal velocity corresponding to the $(0,2)$ mode has a similar amplification curve as the streak amplitude ΔU presented earlier (see Figure 7-12). The modal data also support the conclusion drawn earlier that the $(0,2)$ modes at $R = 838$ were of equal strength despite the difference in the initial forcing amplitudes, indicating a saturated $(0,2)$ mode at $R = 838$. However, the same was not true for the nonstationary $(1,3)$ mode at $R = 838$. For the larger forcing amplitude, the $(1,3)$ mode is expected to have a larger initial amplitude due to the nonlinear interaction of the $(1,1)$ and $(0,2)$ modes followed by a subsequent growth due to linear mechanism. This is clearly illustrated in the figure where the modal $(1,3)$ velocity for the largest forcing combination was approximately a factor of 20 larger than that for $\epsilon_3 \cdot \Delta h_1$. It is plausible that after some critical amplitude of the $(1,3)$ mode was reached, a nonlinear (feedback) interaction of the $(1,1)$ mode with the $(1,3)$ mode was responsible for the enhancement of the stationary $(0,2)$ mode. These results support the conjecture proposed earlier concerning the observed differences in the growth rates of the measured streak amplitudes with the forcing-combination amplitude. The energy transfer between modes appear to favor the low frequencies

134
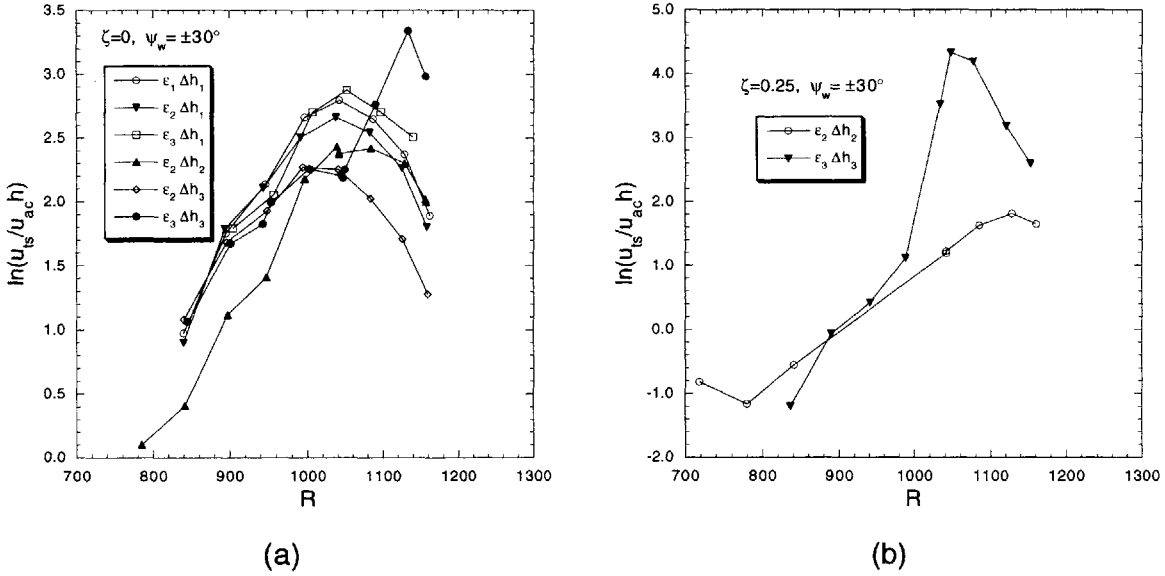
Figure 7-15: Streamwise amplification data (includes all spanwise wavenumbers) for various forcing combinations at (a) $\zeta = 0$ and (b) $\zeta = 0.25$. Data obtained at wall-normal locations corresponding to $U/U_\infty \approx 0.40$ at $\zeta = 0$.

as depicted in the modal velocity data in Figure 7-13 and other data not shown. Similar findings, the so called "β-cascade", have been reported in the simulations of Henningson et $al.$ [126] and experiment of Breuer et $al.$ [101] for localized disturbances in plane Poiseuille flow and boundary-layer flow, respectively.

Wall-normal surveys of the streamwise velocity at several streamwise locations were acquired at two spanwise locations corresponding to a peak and valley for various levels of $\epsilon \cdot \Delta h$. The maximum amplitude of the measured eigenfunction profiles were plotted versus the streamwise location. The results are presented in Figure 7-15. Note that the velocity results here are inclusive of all spanwise wavenumbers present at f_o. The normalized amplification curves for the various forcing combinations at the peak location ($\zeta = 0$) do not collapse as was seen for the 2-D wall waviness results (refer back to Figure 5-4). Again, this may be a result of contributions from other spanwise modal components and/or the effects of vertical vorticity on u_{ts}. The onset of laminar breakdown is clearly evident in the amplification curves for $\epsilon_3 \cdot \Delta h_3$. Transition occurred in the valley region ($\zeta = 0.25$) before it occurred in the peak region ($\zeta = 0$). A plot of u/U_∞ versus Reynolds number for a wall-normal location of

135
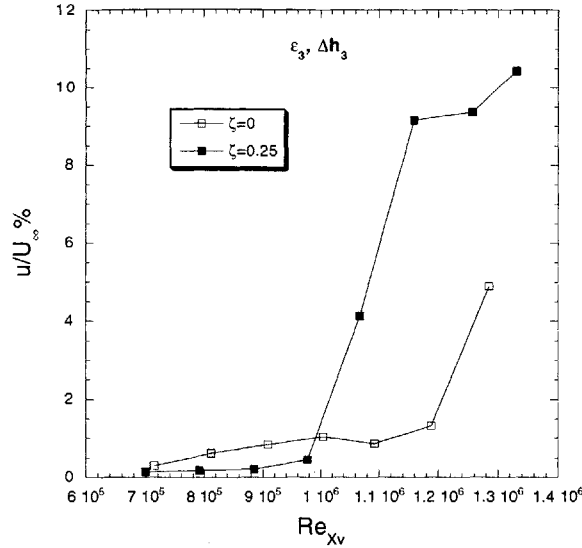
Figure 7-16: u/U_∞ versus Reynolds number for a wall-normal location of $\eta \approx 1.2$ at a peak ($\zeta = 0$) and valley ($\zeta = 0.25$) location.

$\eta \approx 1.2$ is given in Figure 7-16. The transition Reynolds number is in the approximate range of $9.6 \times 10^5 < Re_{tr} < 1.2 \times 10^6$.

Broadband spectra for rms velocity data are presented in Figure 7-17 for a forcing combination ($\epsilon_2 \cdot \Delta h_2$) that did not result in laminar breakdown. The spectral content at a peak location ($\zeta = 0$) was not very different from that at a valley location ($\zeta = 0.25$). As was observed for both the 2-D and oblique wall waviness in the absence of laminar breakdown, T-S wave amplification was observed in the unstable T-S band at both spanwise locations. Figure 7-18 shows broadband spectra for the largest forcing product at a peak and valley spanwise location. At the peak location shown in part (a) of the figure, energy concentrated in frequency bands about the fundamental and first two harmonics are clearly evident in the transitional zone. The spectra indicate an abrupt change in the flow state from laminar to turbulent. At the valley in part (b) of the figure, energy bands at the fundamental and higher-harmonics frequencies (up to the low-pass filter settings) dominated the spectrum in the transitional zone. The streamwise location at which the harmonic bands first became dominant ($x = 139.7cm$, $R = 991$) coincided with the location of the appearance of the upwelling of $u_t(f_o)$ in the spanwise profiles resulting from the strong spanwise

$\zeta=0$
$(\epsilon_2\ \Delta h_2)$

(a)

$\zeta=0.25$
$(\epsilon_2\ \Delta h_2)$
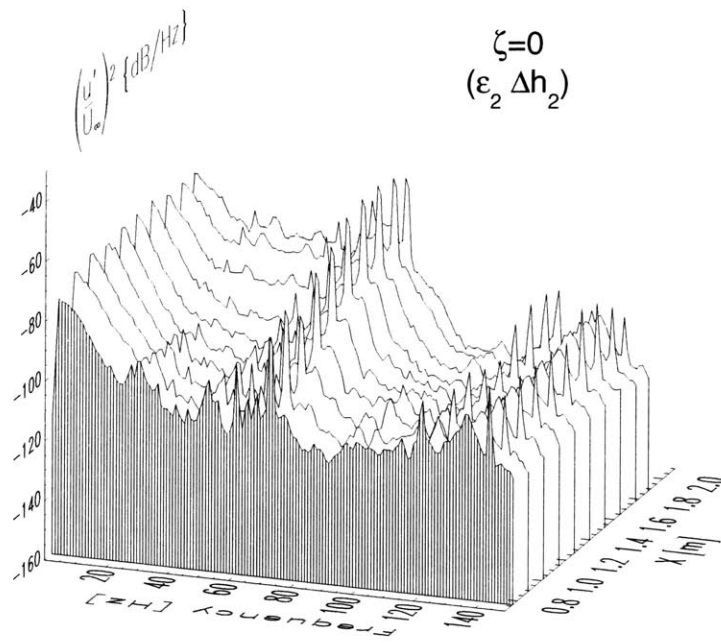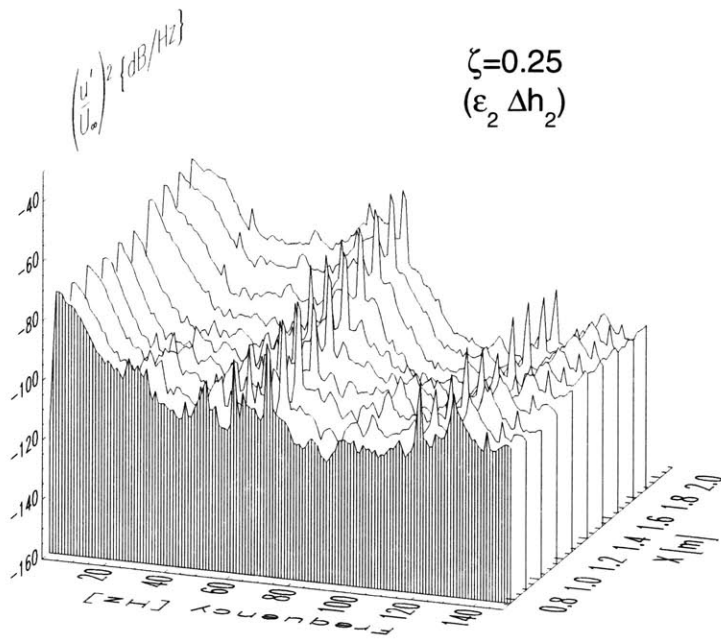
(b)

Figure 7-17: Spectra of streamwise velocity taken at $u_{t,max}$ $(U/U_\infty \approx 0.40)$ for a scenario where breakdown did not occur $(\epsilon_2 \cdot \Delta h_2)$. Measurements were obtained along spanwise locations corresponding to (a) a peak and (b) and valley.
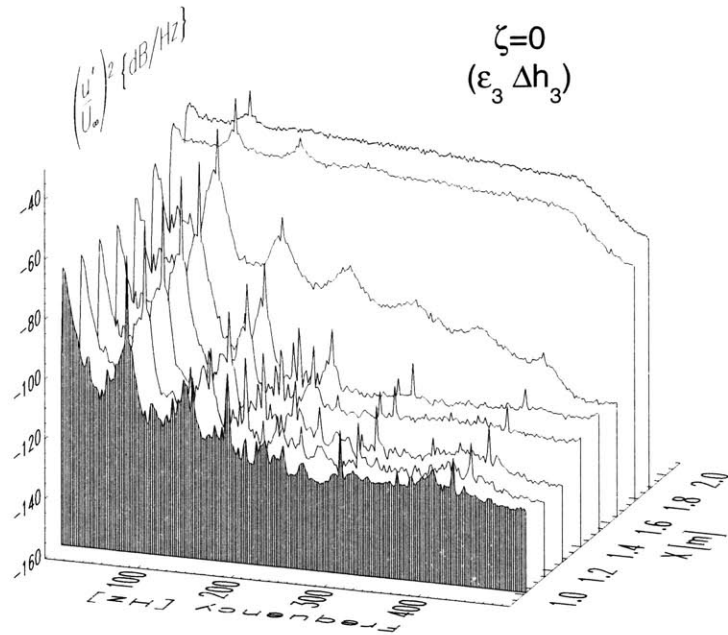
(a)
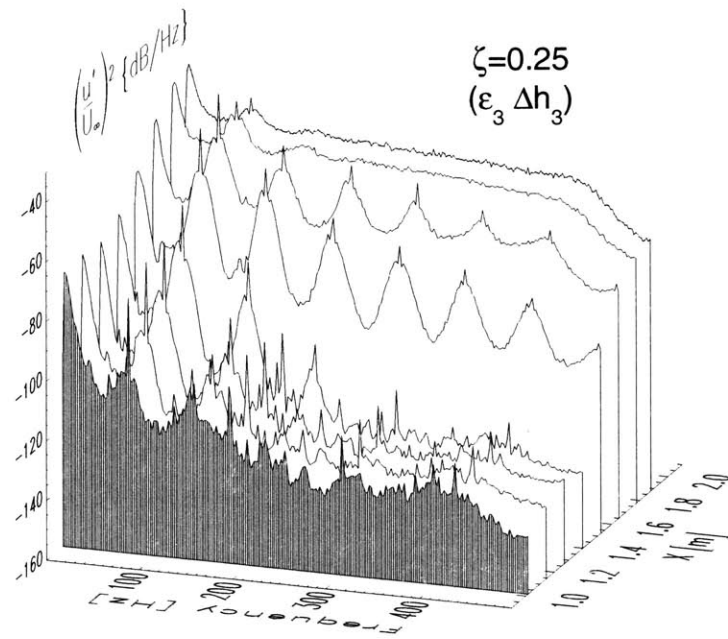
(b)

Figure 7-18: Spectra of streamwise velocity taken at $u_{t,max}$ ($U/U_\infty \approx 0.40$) for a scenario where breakdown occurred ($\epsilon_3 \cdot \Delta h_3$). Measurements were obtained along spanwise locations corresponding to (a) a peak and (b) and valley.

mean shear (refer to Section 7.1). The transitional region associated with the valley appear to be dominated by coherent disturbances and appear more gradual than at the peak location.

For the flow configuration where laminar breakdown occurred with 2-D wall waviness (refer to Chapter 5), energy at subharmonic frequencies were not observed. To focus on the energy in the subharmonic frequency range, the spectral data in Figure 7-18 were re-plotted to magnify the desired frequency range. The resulting spectra in addition to the spectra acquired with 2-D wall waviness (shown for comparison) are presented in Figure 7-19 for $\epsilon_3 \cdot \Delta h_3$. Energy in the subharmonic frequency band was evident in the spectra for the 3-D wall roughness and for that matter in the spectra with smaller forcing products and in the spectra with the oblique wall waviness ($\psi_w = 30°$) for $\epsilon_2 \cdot \Delta h_2$. The energy in the subharmonic band was not dominated by the actual subharmonic frequency ($f_o/2 = 35.5 Hz$) but by a broad band of frequencies ($20 < f < 50 Hz$). The subharmonic energy at the peak location ($\zeta = 0$) was found to be more significant than the associated energy at the valley location (refer to parts (b) and (c) of the figure). At the peak location, narrow-band energy centered at $f = 22 Hz$ and $48 Hz$, for which the source of either was unknown, were evident. Either one of these disturbance energy can possibly interact with the fundamental frequency ($f_o = 71 Hz$) to produce the other. Higher-order spectral methods applied to multipoint measurements are necessary to resolve the issue of a sum or difference interaction. Such measurements were not acquired in this study. Broader energy bands were also observed for central frequencies of $f = 29 Hz$ and $42 Hz$. The same can be said about this frequency pair as was done for $f = 22 Hz$ and $48 Hz$. The first of the main points to be made here is the evidence of energy in the subharmonic frequency range, though much less than the energy in the harmonic frequency bands. Secondly, at the peak location where the subharmonic energy band was largest, more spectral filling/broadening at frequencies in between the harmonic bands were observed in the transitioning boundary layer (see Figure 7-18) implying nonlinear interactions between subharmonic and harmonic disturbances. Last but not least, despite the presence of subharmonic energy, the dominant energy transfer is clearly to the higher

139
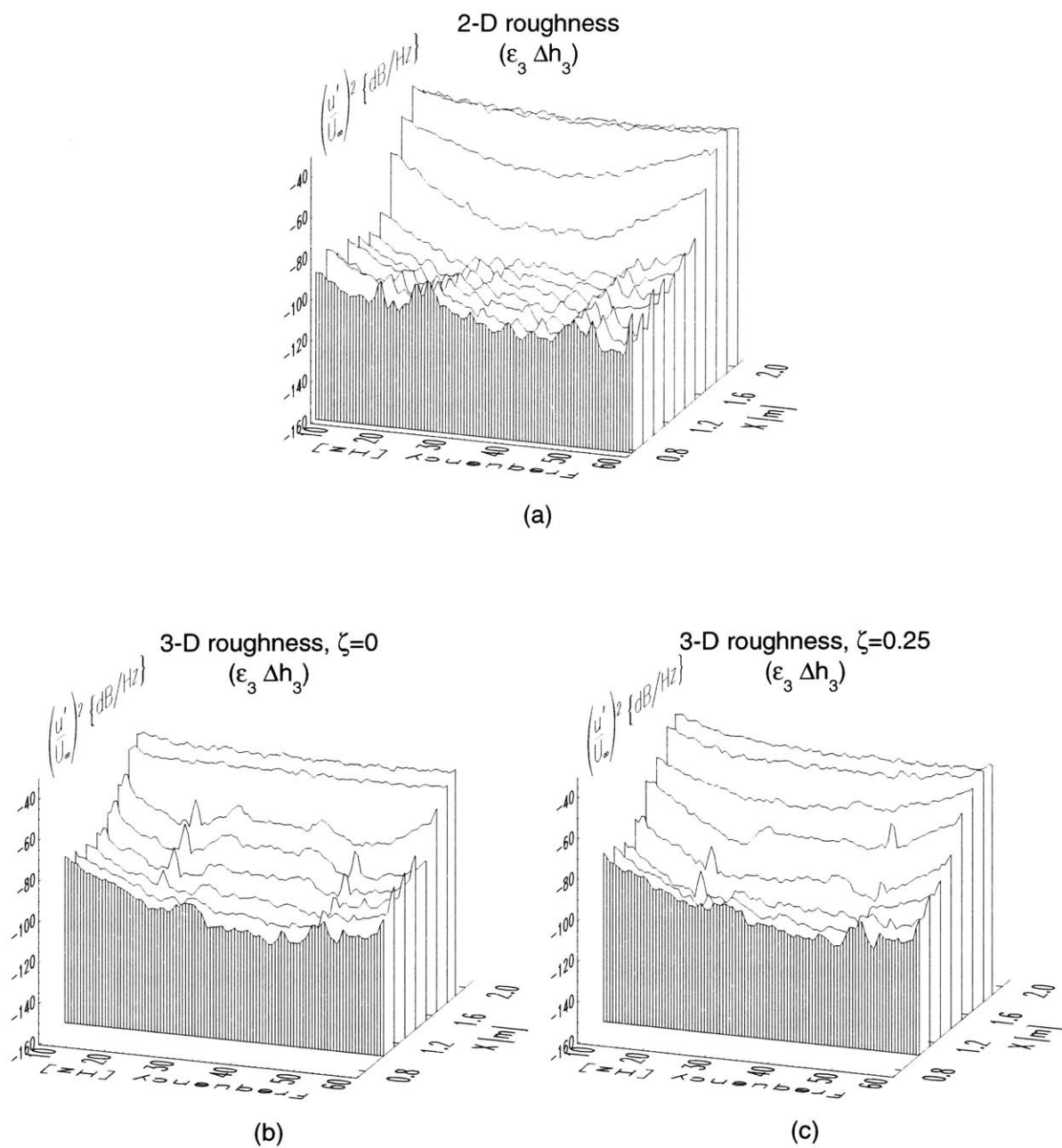
Figure 7-19: Spectra of streamwise velocity in the subharmonic frequency range taken at $u_{t,max}$ for scenarios where breakdown occurred. Measurements are shown over a range of streamwise locations for (a) two-dimensional surface waviness, (b) three-dimensional roughness along $\zeta = 0$, and (c) three-dimensional roughness along $\zeta = 0.25$.

harmonics as is evident from the spectra shown in Figure 7-18. In other words, there is some redistribution of energy (second-order effect) to the subharmonic frequency band but the physical process responsible for spectral broadening is dominated by the nonlinear interactions (self and mutual) of the fundamental and higher-harmonic energies.

7.3 Summary

Oblique transition of a Blasius boundary layer was initiated by generating a pair of oppositely-oriented oblique O-S modes with the use of non-localized three-dimensional (3-D) surface waviness patterns $(\alpha_w, \pm\beta_w) = (\alpha_{ts,I}, \pm\beta_{ts,I})$. Spanwise and wall-normal measurements of the instantaneous streamwise velocity were acquired for various acoustic forcing levels, ϵ, and roughness heights, Δh (see Table 3.1). Primary instability waves, $(f/f_o, \pm\beta/\beta_w) = (1, \pm 1)$, were introduced into the boundary layer by proper selection of the wall-roughness spectrum and freestream acoustic forcing to enhance the receptivity mechanism. The oblique primary modes $(1, \pm 1)$ were observed to interact nonlinearly to create low- and high-speed streaks. The *lift-up* effect resulting from the stationary vortex system $(0, 2)$ was believed responsible for the streak formation that culminated in a peak-valley structure in the spanwise profiles of the streamwise velocity component. The growth rates of the streaky structures were believed to be enhanced by nonlinear interactions of two nonstationary boundary-layer disturbance modes, namely the $(1, 1)$ mode and $(1, 3)$ mode, provided some threshold amplitude of the $(0, \pm 2)$ mode was initially satisfied. For the largest value of the forcing product $(\epsilon_3 \cdot \Delta h_3)$, an *explosive* secondary instability was observed that ultimately lead to laminar breakdown. The onset of breakdown was observed in regions of large spanwise velocity gradients, $|dU/d\zeta|$, and manifested itself in the form of an upwelling of $u_t(f_o)$ on the both side of a peak location. The maximum values of u_t were found to scale with $|dU/d\zeta|$. Velocity-deficit profiles acquired for the perturbed boundary layer suggest a tendency towards wall-normal inflectional velocity profiles, $U(\eta)$, except for the velocity profiles acquired in the valley regions downstream of the

onset of laminar breakdown.

Three-dimensional eigenfunctions, amplitude and phase, were measured which included phase-locked velocity fluctuations at f_o for all values of the spanwise wavenumber β. Remarkable agreement was observed between the measured O-S eigenfunction with oblique waviness and the 3-D eigenfunction, both in amplitude and phase. An average disturbance phase speed of $\bar{c}_{ph}/U_\infty = 0.35$ was measured at a streamwise location corresponding to $R \approx 1038$ for all possible forcing combinations. Modal velocities were presented for following modes: $(1,1)$, $(0,2)$, $(0,0)$, $(2,0)$, $(2,2)$, $(1,3)$, $(3,1)$, and $(3,3)$. For a configuration where the flow remained laminar, the modal velocity data indicated a dampening of all the significant nonstationary modes after some initial meager amplification. However, for a configuration with laminar breakdown present, all nonstationary modes were seen to amplify significantly as expected. Excellent qualitative agreement was observed between the measured modal velocities and results obtained by spatial direct numerical simulation [103]. The energy transfer between the measured modes appear to favor low frequencies, the so called β-cascade [126, 101].

For broadband spectra obtained through laminar breakdown at a peak location, energy concentrated in frequency bands about the fundamental and first two harmonics were evident. At a valley location, energy bands at the fundamental and higher-harmonic frequencies (up to the low-pass filter settings) dominated the spectrum. The streamwise location at which the harmonic bands first became dominant at a valley location coincided with the location of the appearance of the upwelling of $u_t(f_o)$ in the spanwise profiles resulting from the strong spanwise mean shear. The transitional region associated with the valley appear to be dominated by coherent disturbances and appear more gradual than at a peak location. Evidence of energy in the subharmonic frequency range, though much less than the energy in the harmonic frequency bands, were evident at peaks and valleys. At the peak location where the subharmonic energy band was largest, more spectral filling/broadening at frequencies in between the harmonic bands were observed in the transitioning boundary layer implying nonlinear interactions between subharmonic and harmonic disturbances.

Chapter 8

Concluding Remarks and Future Work

The most widely used transition prediction tool is currently the e^N method which is a semiempirical method based on linear amplification (not disturbance amplitudes) of unstable modes. This approach does not include any physics regarding the role of the external disturbance environment on the boundary-layer instability development. Improved transition prediction tools based on an amplitude approach need to incorporate physics relating the effects of the environment on the transition process. This approach needs, as an input, information about the initial boundary-layer disturbance amplitude, and this need is met by a better understanding of the receptivity process. Consequently, receptivity plays a crucial role in any transition prediction tool that utilizes an amplitude based approach. The objectives of the current research were (i) to better understand the acoustic receptivity process and subsequent disturbance evolution in the presence of wavy surfaces and correlate results with theory and (ii) to improve the current knowledge of the oblique transition process while providing a potential data base for comparison with theory and/or numerical simulations. Experimental investigations were conducted to examine acoustic receptivity and subsequent boundary-layer instability evolution in the presence of 2-D and oblique surface waviness and to explore the transition scenario initially excited by a pair of oppositely-oriented oblique O-S modes, oblique transition. These investi-

gations provided a data base which can ultimately be used to validate current and future theoretical receptivity/transition models and numerical simulations needed to improve the current understanding of laminar-to-turbulent transition.

The experiments were conducted for a nominally zero-pressure gradient boundary layer formed over a flat plate. The receptivity mechanism was facilitated by the use of surface waviness of height Δh and freestream acoustic excitation with amplitude ϵ $(= u_{ac}/U_{\infty})$. The study was performed using a matrix array of forcing combinations, $\epsilon \cdot \Delta h$. Acoustic receptivity was examined in the presence of non-localized 2-D and oblique surface waviness that extended over a streamwise distance of $\Delta x = 0.56m$. The wavenumber of the surface waviness was selected to match the near-resonance condition at Branch I, $(\alpha_w, \beta_w) = (\alpha_{ts,I}, \beta_{ts,I})$, for an acoustic excitation frequency f_o $(= \omega_{ts}/2\pi)$. The location of the surface waviness was selected such that its mid-point was near the location of Branch I to maximize the receptivity. Receptivity coefficients for the near-resonance and detuned conditions were computed based on the Branch I location. The subsequent streamwise development of the boundary-layer disturbance field was acquired to downstream locations just beyond the upper neutral point (Branch II). Oblique transition was investigated by exciting a pair of oppositely-oriented oblique O-S modes, $(f/f_o, \pm\beta/\beta_w) = (1, \pm 1)$. The oblique waves were generated by producing a roughness pattern (3-D) that consisted of a pair of surface waviness with $\psi_w = \pm 30°$ in conjunction with the freestream acoustic field. The extent and location of the roughness pattern are the same as discussed above for the receptivity phase of the study. The focus here was placed on the subsequent nonlinear interactions and modal disturbance velocity evolution.

8.1   Contributions

The current study not only provides an experimental data base, but contributes to the overall understanding of laminar-to-turbulent transition physics. Here, the major contributions achieved throughout this study will be highlighted. A summary with further details for each of the chapters on results and discussions is found in

the last section of the respective chapters, namely Sections 4.4, 5.4, 6.4, & 7.3. A subtle accomplishment was the ability to introduce a variety of steady boundary-layer disturbances via the well-defined receptivity sites without any measurable first-order effects on the base flow.

Existing acoustic receptivity measurements over non-localized surface waviness were limited to results for 2-D surface waviness [83]. The current study explored, in addition to 2-D acoustic receptivity, the subsequent evolution of the boundary-layer instability. The current acoustic receptivity measurements with 2-D waviness are in excellent agreement with the existing experimental measurements [83] and theoretical results [85, 24]. For a configuration where laminar-to-turbulent breakdown occurred ($\epsilon_3 \cdot \Delta h_3$), the breakdown process was found to be dominated by energy at the fundamental and higher-harmonic frequencies, indicative of K-type breakdown. Receptivity data were acquired experimentally for the first time over oblique wavy surfaces ($\psi_w = 15°, 30°$, and $45°$) to measure the dependence of receptivity on roughness obliqueness. The current findings were in substantial agreement with theory and experimentally confirmed the earlier theoretical results [79] that receptivity increases markedly with wave obliqueness. Boundary-layer transition was not observed for the forcing combination used with the oblique surface waviness.

A pair of oppositely-oriented oblique O-S modes was generated with the use of non-localized 3-D surface waviness patterns, $(\alpha_w, \pm\beta_w) = (\alpha_{ts,I}, \pm\beta_{ts,I})$. The oblique primary modes, $(f/f_o, \pm\beta/\beta_w) = (1, \pm1)$, were observed to interact nonlinearly to create low- and high-speed streaks. The *lift-up* effect resulting from the stationary vortex system $(0, 2)$ was believed responsible for the streak formation that culminated in a peak-valley structure of the spanwise U profiles. The growth rates of the streaky structures were believed to be enhanced by nonlinear (feedback) interactions of two nonstationary boundary-layer disturbance modes, namely the $(1, 1)$ mode and $(1, 3)$ mode, provided some threshold amplitude of the $(0, \pm2)$ mode was initially satisfied. For the largest value of the forcing product ($\epsilon_3 \cdot \Delta h_3$), an *explosive* secondary instability was observed that ultimately lead to laminar-to-turbulent transition. The onset of breakdown was observed in regions of large spanwise velocity gradients, $|dU/d\zeta|$,

145

and manifested itself in the form of an upwelling of $u_t(f_o)$ in the spanwise profiles on both sides of a peak location. Modal velocities were presented for the following modes: $(1,1)$, $(0,0)$, $(0,2)$, $(2,0)$, $(2,2)$, $(1,3)$, $(3,1)$, and $(3,3)$. Excellent qualitative agreement was observed between the measured modal velocities and results obtained by spatial direct numerical simulation (see for example [103]). The energy transfer between the measured modes appear to favor low frequencies, the so called β-cascade [126, 101].

The transition Reynolds number measured on the smooth surface without acoustic forcing (baseline configuration) was $Re_{tr} \approx 3.2 \times 10^6$. The values of Re_{tr} for the 2-D and 3-D surface roughness with a forcing combination of $\epsilon_3 \cdot \Delta h_3$ were significantly less ($\sim 60\%$ reduction) than that for the baseline configuration. The drastic shifts in the value of Re_{tr} demonstrate the sensitivity of the transition location to the freestream environment and surface conditions.

8.2 Recommendation for future work

Further work directly related to the current study include the effects of:

- simultaneous forcing at the subharmonic and fundamental frequencies to determine what effect, if any, the inclusion of the subharmonic forcing has on the laminar-to-turbulent breakdown process for the oblique transition scenario.

- broadband forcing (e.g. band-limited white noise) with particular interest placed on subsequent nonlinear mode interactions leading to transition.

- large background freestream turbulence on receptivity and subsequent disturbance growth (e.g. influence on T-S growth rates).

- exciting a difference (nonlinear) interaction between two steady wall-modes ($k_{w,1}$ and $k_{w,2}$) produced by the surface roughness (i.e. $k_w = k_{w,1} - k_{w,2}$ where $k_{w,1}, k_{w,2} > k_w$) to determine the efficiency of the receptivity mechanism.

146

There has been significant progress in the past twenty years regarding our understanding of receptivity. Our knowledge with regards to acoustic receptivity has been more forthcoming than for receptivity due to freestream turbulence. Improved methods for the generation of reproducible freestream turbulence are needed in laboratory studies as well as improvements in the theoretical models of three-dimensional turbulence. Perhaps the most important missing link is our lack of knowledge of actual freestream environments. Detailed measurements of freestream disturbances in terms of spatial scales, orientation, and temporal content are desperately needed in flight environments. Measurements of this type can lead to improved stochastic models for the freestream environment and ultimately lead to more accurate prediction methods of laminar-to-turbulent transition.

Appendix A

Error Analysis

In any experimental study, one needs to consider the *degree of goodness* of the measured and experimental results. This is normally achieved by conducting an uncertainty analysis to obtain estimates of the experimental errors within a defined confidence level. The uncertainty analysis performed in this appendix follows the analysis outlined by Coleman & Steele [127]. The term *accuracy* refers to the closeness of agreement between a measured value and the true value. The total error of a measurement is the sum of a bias error and precision error. The bias error is the fixed or systematic component of the total error and the precision error (repeatability) is the random component.

For the random component or precision error, it is reasonable to assume that the variability follows a Gaussian distribution. Consequently, the experimental measurements are considered samples from a Gaussian parent population. The mean of the sample population is defined by

$$\bar{X} = \frac{1}{N_s} \sum_{i=1}^{N_s} X_i \qquad (A.1)$$

where N_s is the number of sampled data, X. The precision index or standard deviation of the sample population is given as

$$\hat{S}_X = \left[\frac{1}{N_s - 1} \sum_{i=1}^{N_s} (X_i - \bar{X})^2 \right]^{1/2} . \qquad (A.2)$$

149

The precision index associated with the sample mean $\bar{X}$ is expressed as

$$\hat{S}_{\bar{X}} = \frac{\hat{S}_X}{\sqrt{N_s}}. \tag{A.3}$$

The precision limit, $\hat{P}$, is defined as

$$\hat{P}_{\bar{X}} = t \cdot \hat{S}_{\bar{X}} \tag{A.4}$$

where the value of t depends on the confidence interval. For a confidence interval of 95%, the probability that the true mean, $\hat{\mu}$, lies within $\bar{X} \pm t\hat{S}_{\bar{X}}$ can be written as

$$\text{Probability}(\bar{X} - t \cdot \hat{S}_{\bar{X}} \le \hat{\mu} \le \bar{X} + t \cdot \hat{S}_{\bar{X}}) = 0.95. \tag{A.5}$$

In the above expression, $(\bar{X} - \hat{\mu})/\hat{S}_{\bar{X}}$ now obeys a t distribution instead of the Gaussian distribution. So for a 95% confidence limit, a value of $t = 2.0$ for $N_s \ge 31$ is used in Equation A.4.

Next, consider the uncertainty component resulting from the bias error. The bias limit, $\hat{B}$, is defined as an estimate of the uncertainty due to the bias error with the same confidence level as $\hat{P}$, namely 95%. This is interpreted to mean that the bias error is equal to or less than $\hat{B}$ with a 95% degree of certainty. The elemental bias limit for the Jth variable is defined using a root-sum-square (RSS) method as follows for M significant elemental errors

$$\hat{B}_J = \left[\sum_{i=1}^{M} \hat{B}_{J,i}^2 \right]^{1/2} \tag{A.6}$$

where $\hat{B}_{J,i}$ is the elemental bias error of the Jth variable due to element i.

The precision and bias limits with regards to a 95% confidence level have been defined. The uncertainty, $\hat{U}_X$, of a variable X is defined using the RSS method as follows

$$\hat{U}_X = \left[\hat{B}_X^2 + \hat{P}_X^2 \right]^{1/2}. \tag{A.7}$$

For a data reduction equation (DRE) of the form

$$f = f(X_1, X_2, \ldots, X_J), \tag{A.8}$$

150

the uncertainty in f resulting from the measured uncertainties, assuming that the measured errors are uncorrelated, is given by

$$\hat{U}_{\mathrm{f}} = \left[\sum_{i=1}^{J} \hat{\theta}_i^2 (\hat{B}_i^2 + \hat{P}_i^2) \right]^{1/2} = \left[\sum_{i=1}^{J} \hat{\theta}_i^2 \cdot \hat{U}_i^2 \right]^{1/2} \tag{A.9}$$

where the absolute sensitivity coefficients are

$$\hat{\theta}_i = \frac{\partial \mathrm{f}}{\partial X_i}. \tag{A.10}$$

Alternately, the uncertainty of the DRE can be written as

$$\hat{U}_{\mathrm{f}} = \left[\hat{B}_{\mathrm{f}}^2 + \hat{P}_{\mathrm{f}}^2 \right]^{1/2}. \tag{A.11}$$

Estimated bias limits, $\hat{B}$, for the pertinent instruments used in the current study are presented in Table A.1 (refer to Section 2.3 for brief instrument descriptions). All of the listed instrumentation were verified to be within the manufacturers tolerance. If the manufacturer specifications were not met, the measured tolerances were used. As a result, the bias limits in the table reflect the largest tolerance, either the manufacturer or measured tolerance. Consider for example the mean output voltages, $E_{\Delta P}$, of the differential pressure transducers (Datametrics Barocell) acquired by the VXI. Note here that ΔP represents differential pressures measured at the tunnel entrance, ΔP_e, and at the calibration location, ΔP_{cal}, both referenced to the settling chamber pressure P_{sc}. The bias limit of the measured mean voltage as a function of $E_{\Delta P}$ is denoted in the table as $\hat{B}_{E_{\Delta P}, \mathrm{VXI}}$. The equation relating ΔP to $E_{\Delta P}$ is indicated in the second column. Using Equations A.9 & A.11, the bias limits are related as follows,

$$\hat{B}_{\Delta P, \mathrm{VXI}}^2 = \left(\frac{d\Delta P}{dE_{\Delta P}} \cdot \hat{B}_{E_{\Delta P}, \mathrm{VXI}} \right)^2 \tag{A.12}$$

where $\hat{B}_{\Delta P, \mathrm{VXI}}$ is the bias limit contribution from the measured voltage to the overall ΔP bias limit. The other bias limits in the table were obtained in a similar fashion as above. In the expression for the bias limit of the amplifier/filter (SR650), $\hat{B}_{e(t), \mathrm{SR650}}$, the reading value, RD, was approximated as RD $\approx \sqrt{2}e$ where e is the rms fluctuating voltage.

151

Label	Instrument	Bais limits $\hat{B}$
I	Mensor 15000	$\hat{B}_{P,\text{mensor}} = \pm 0.01\% \cdot \text{FS} = \pm 13.8 \ \{\text{Pa}\}$
II	Datametrics Barocell	$\hat{B}_{\Delta P,\text{barocell}} = \pm(0.2\% \cdot \text{RD} + 0.003\% \cdot \text{FS})$ $= \pm(0.2 \cdot \Delta P + 4.0) \cdot 10^{-2} \ \{\text{Pa}\}$
III	General Eastern 800LC – Temperature T – Relative humidity ϕ	 $\hat{B}_{T,\text{800LC}} = \pm 0.5 \ \{^\circ\text{C}\}$ $\hat{B}_{\phi,\text{800LC}} = \pm 3 \ \{\%\text{RH}\}$
IV	VXI E1413B – $E_{\Delta P}$ $\quad \Delta P \approx 1333 \cdot E_{\Delta P}$ – E_T $\quad T = 111.1 \cdot E_T - 17.8$ – E_ϕ $\quad \phi = 100 \cdot E_\phi$ – $E_{U_{hw}}$ (hot-wire output) $\quad U_{hw} = \sum_{n=0}^{4} a_n E^n$	 $\hat{B}_{E_{\Delta P},\text{VXI}} = \pm(1.0 \cdot 10^{-8} E_{\Delta P}^2 + 1.4 \cdot 10^{-8})^{1/2} \ \{\text{V}\}$ $\hat{B}_{\Delta P,\text{VXI}} = \pm(1.0 \cdot 10^{-8} \cdot \Delta P^2 + 2.4 \cdot 10^{-2})^{1/2} \ \{\text{Pa}\}$ $\hat{B}_{E_T,\text{VXI}} = \pm(1.0 \cdot 10^{-8} \cdot E_T^2 + 3.4 \cdot 10^{-9})^{1/2} \ \{\text{V}\}$ $\hat{B}_{T,\text{VXI}} = \pm 7.2 \cdot 10^{-3} \ \{^\circ\text{C}\}$ $\hat{B}_{E_\phi,\text{VXI}} = \pm(1.0 \cdot 10^{-8} \cdot E_\phi^2 + 1.4 \cdot 10^{-8})^{1/2} \ \{\text{V}\}$ $\hat{B}_{\phi,\text{VXI}} = \pm 1.6 \cdot 10^{-2} \ \{\%\text{RH}\}$ $\hat{B}_{E_U,\text{VXI}} = \pm(1.0 \cdot 10^{-8} \cdot E_U^2 + 2.2 \cdot 10^{-7})^{1/2} \ \{\text{V}\}$ $\hat{B}_{U_{hw},\text{VXI}} = \hat{B}_{E_U,\text{VXI}} \cdot \sum_{n=1}^{4} n \cdot a_n E^{n-1} \ \{\text{m/s}\}$
V	IOtech ADC488/8SA max FS = 2 $\{\text{V}\}$	$\hat{B}_{e(t),\text{IOtech}} = \pm 0.02\% \cdot \text{FS} \ \{\text{V}\}$ $= \pm 4 \cdot 10^{-4}/\text{GN} \ \{\text{V}\}$
VI	SR650	$\hat{B}_{e(t),\text{SR650}} = \pm 4.7\% \cdot \text{RD} \approx \pm 4.7\% \cdot (\sqrt{2} \cdot e) \ \{\text{V}\}$

Table A.1: Tabulated instrumentation list (refer to Section 2.3) and corresponding bias limits used for conducting error analysis. FS, RD, and GN denote full-scale, reading, and gain, respectively.

Measured variable	Nominal value	Instrument list	$\hat{B}$	$\hat{P}$	$\hat{U}$
P_{sc} {Pa}	$1.02 \cdot 10^5$	I	± 13.8	± 0.28	± 13.8
ΔP_{min} {Pa}	0.9	II,IV	± 0.16	$\pm 2.0 \cdot 10^{-3}$	± 0.16
ΔP_{max} {Pa}	81.0		± 0.26	$\pm 2.0 \cdot 10^{-3}$	± 0.26
T {°C}	21	III,IV	± 0.5	$\pm 2.8 \cdot 10^{-3}$	± 0.5
ϕ {%RH}	30 - 65	III,IV	± 3.0	$\pm 4.0 \cdot 10^{-3}$	± 3.0
$A_R = \frac{A_e}{A_{sc}}$	0.1013	tape measure	$\pm 2.7 \cdot 10^{-3}$	–	$\pm 2.7 \cdot 10^{-3}$

Table A.2: Table showing measured variables with corresponding instrument list (refer to Table A.1). Typical values of $\hat{B}$, $\hat{P}$, and $\hat{U}$ (same units as noted in first column) for the measured variables are shown.

The precision limits, $\hat{P}$, for the mean measurements were estimated by taking N_s samples and applying Equation A.4 at each data point throughout the experiment. The upper bounds of $\hat{B}$ and $\hat{P}$ along with the resulting $\hat{U}$ for each of the measured values are presented in Table A.2. The corresponding units of measurement are included in the first column. For the measurement of P_{sc}, $N_s = 50$ and for all other measurements, $N_s = 256$. The nominal value of each measured variable is also included. The third column titled **Instrument list** denotes the grouping of instruments (refer back to Table A.1 for label designations) used to acquire the measured value. The bias limits were obtained by considering the most significant elemental sources. Consider for example the bias error of the temperature, T. The two elemental sources are the General Eastern model 800LC temperature indicator (III) and the VXI model E1413B A/D converter (IV). Applying Equation A.6, the bias error, $\hat{B}_T$, was obtained ($\hat{B}_T = [\hat{B}_{T,800LC}^2 + \hat{B}_{T,VXI}^2]^{1/2}$). The bias limit, $\hat{B}_{A_R}$, of the area ratio was estimated by assuming an error of $\pm 12.7 mm$ in each linear dimension used to compute the ratio A_R (area ratio of the test-section entrance to the settling chamber). The precision limit for A_R was considered negligible. Note that in all the measured values, $\hat{P}/\hat{B} \ll 1$ so that $\hat{U} \approx \hat{B}$.

Data reduction variable	Equation reference(s)	Uncertainty $\{\%\}$ $\%\hat{U}$
$P_T(P_{sc}, P_e, A_R)$	3.11 or A.13	± 0.014
$U_{cal}(\rho, \Delta P_{cal}, \Delta P_e, A_R)$ or $U_e(\rho, \Delta P_e, A_R)$	A.18 or A.19	Min. U : ± 9.0 Max. U : ± 1.4
$\rho(P, T, \phi)$	3.5	± 3.0
$\mu(T, \phi)$	A.20	± 2.0
$Re(\rho, U_{cal}, \mu)$	$\rho U_\infty / \mu$	± 4.0
$U_{hw}(E, U_{cal}, \mathrm{MSE})$	A.24 $-$ A.28	Min. U : ± 9.0 Max. U : ± 1.4
$u_{hw}(E, e(t))$	A.33 & A.36	± 4.7

Table A.3: Estimated percent uncertainties for the given data reduction variables acquired throughout the experiment. The functional form of the data reduction variables emphasizes the variables that affected the uncertainties.

The uncertainty limits for the DRE are tabulated in Table A.3. The equation references of the equations used for the computations are included in the second column. Note that the uncertainties presented here are percent uncertainties. As an example, consider the uncertainty in the data reduction variable P_T (total pressure). Noting that $P_e = P_{sc} - \Delta P_e$, Equation 3.11 can be rewritten in terms of measured variables as

$$P_T = P_{sc} - \Delta P_e + \frac{\Delta P_e}{1 - A_R^2}. \tag{A.13}$$

Applying Equation A.9, the following expression for the total pressure uncertainty, $\hat{U}_{P_T}$, is

$$\hat{U}_{P_T}^2 = \left(\frac{\partial P_T}{\partial P_{sc}}\hat{U}_{P_{sc}}\right)^2 + \left(\frac{\partial P_T}{\partial \Delta P_e}\hat{U}_{\Delta P_e}\right)^2 + \left(\frac{\partial P_T}{\partial A_R}\hat{U}_{A_R}\right)^2 \tag{A.14}$$

where the partial derivatives are

$$\frac{\partial P_T}{\partial P_{sc}} = 1 \tag{A.15}$$

$$\frac{\partial P_T}{\partial \Delta P_e} = \frac{A_R^2}{1 - A_R^2} \tag{A.16}$$

$$\frac{\partial P_T}{\partial A_R} = \frac{2A_R}{(1 - A_R^2)^2} \Delta P_e. \tag{A.17}$$

Similarly, the uncertainties for U_{cal} and U_e are obtained using the following equations

$$U_{cal} = \left[\frac{2}{\rho} \left(\Delta P_{cal} - \frac{\Delta P_e}{1 - A_R^2} - \Delta P_e \right) \right]^{1/2} \tag{A.18}$$

and

$$U_e = \left[\frac{2\Delta P_e}{\rho} \times \frac{1}{1 - A_R^2} \right]^{1/2}, \tag{A.19}$$

respectively. The range of percent uncertainties for U_{cal} (or U_e) given in Table A.3 were obtained at the maximum velocity ($U_\infty \approx 11.1 m/s$) and minimum velocity ($U \approx 0.1 U_\infty$). A plot of calibration velocity percent uncertainty, $\% \hat{U}_{U_{cal}}$ ($\% \hat{U}_{U_{cal}} = \hat{U}_{U_{cal}}/U_{cal} \times 100\%$), versus the calibration velocity, U_{cal}, is shown in Figure A-1. The results are almost identical for $\% \hat{U}_{U_e}$ versus the tunnel entrance velocity, U_e. The velocity percent uncertainties become large for small velocities due primarily to the contribution of the percent FS component of the bias limits in the measurements of the ΔP's. The actual errors are expected to be smaller since special care was taken to reduce drift in the transducers by frequently adjusting the zeroes after each survey profile. The uncertainty for the density, ρ, was obtained using the same procedure outlined above.

For the uncertainty in the moist air viscosity, μ, consider Equation 3.10 which can be rewritten as

$$\mu = K_1 \cdot \mu_v + K_2 \cdot \mu_a \tag{A.20}$$

where K_1 and K_2 are given by

$$K_1 = \left(1 + \left(\frac{P_a}{P_v} \right) \cdot \frac{\left[1 + \left(\frac{\mu_v}{\mu_a} \right)^{1/2} \left(\frac{M_v}{M_a} \right)^{1/4} \right]^2}{\left[8 \left(1 + \frac{M_v}{M_a} \right) \right]^{1/2}} \right)^{-1} \tag{A.21}$$

$$K_2 = \left(1 + \left(\frac{P_v}{P_a} \right) \cdot \frac{\left[1 + \left(\frac{\mu_a}{\mu_v} \right)^{1/2} \left(\frac{M_a}{M_v} \right)^{1/4} \right]^2}{\left[8 \left(1 + \frac{M_a}{M_v} \right) \right]^{1/2}} \right)^{-1}. \tag{A.22}$$

155
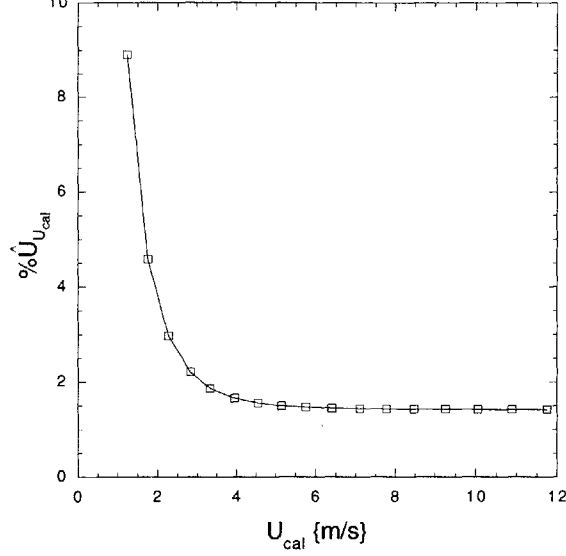
Figure A-1: Typical plot of velocity uncertainty versus velocity for velocities measured using the differential transducers.

Noting that $\mu_a/\mu_v \approx 0.54$ and $M_v/M_a \approx 0.62$, K_1 and K_2 are essentially constants. The viscosity uncertainty, $\hat{U}_\mu$, can be written as

$$\hat{U}_\mu^2 = \left(K_1 \hat{U}_{\mu_v}\right)^2 + \left(K_2 \hat{U}_{\mu_a}\right)^2 \tag{A.23}$$

where the uncertainties due to temperature and relative humidity were neglected. The following uncertainties, $U_{\mu_v} = \pm 2\%$ [115] and $U_{\mu_a} = \pm 2\%$ [114], were used in Equation A.23. The effects of T and ϕ on the uncertainty $\hat{U}_\mu$ were negligible and consequently were not included Equation A.23.

For the mean velocity measured with the hot-wire, U_{hw}, the uncertainty $\hat{U}_{U_{hw}}$ can be estimated by expressing it as a RSS of all pertinent uncertainties as follows

$$\hat{U}_{U_{hw}}^2 = \hat{U}_{U_{hw},\text{VXI}}^2 + \hat{U}_{U_{cal}}^2 + \hat{U}_{fit}^2. \tag{A.24}$$

The first term on the right hand side of Equation A.24, $\hat{U}_{U_{hw},\text{VXI}}$, represents the contribution from the uncertainty in the measured mean voltage, E. Recalling Equation 3.12, $\hat{U}_{U_{hw},\text{VXI}}$ can be expressed as

$$\hat{U}_{U_{hw},\text{VXI}}^2 = \left[\frac{d}{dE}\left(\sum_{n=0}^{4} a_n E^n\right) \times \hat{U}_{E_U,\text{VXI}}\right]^2 \tag{A.25}$$

$$= B_{U_{hw},\text{VXI}}^2 + \left(\sum_{n=1}^{4} n \cdot a_n E^{n-1}\right)^2 \times \hat{P}_{E_U,\text{VXI}}^2 \tag{A.26}$$

156

where $\hat{B}_{U_{hw},\text{VXI}}$ is given in Table A.1 and $\hat{P}_{E_U,\text{VXI}}$ was measured ($\hat{P}_{E_U,\text{VXI}} \approx 3.0 \times 10^{-4}\{V\}$). The second term in Equation A.24, $\hat{U}_{U_{cal}}$, is the uncertainty in the measured value of U_{cal} used as the calibration standard for the hot-wire anemometer system (refer to Table A.3 and Figure A-1 for typical values of $\hat{U}_{U_{cal}}$). The last term, $\hat{U}_{fit}$, represents the uncertainty resulting from the calibration (fourth-order polynomial) fit – see Figure 3-5 for example hot-wire calibration curve. This uncertainty was defined as

$$\hat{U}_{fit} = 2 \times (\text{MSE})^{1/2} \tag{A.27}$$

where MSE is the mean square error of the calibration fit and is defined as

$$\text{MSE} = \frac{1}{N_p} \sum_{n=0}^{N_p} \left(\sum_{i=0}^{4} a_i E^i - U_{cal} \right)_n^2 \tag{A.28}$$

where N_p is the number of calibration points. Using Equations A.24 – A.28, the uncertainties, $\hat{U}_{U_{hw}}$, shown in Table A.3 were obtained. The contribution from $\hat{U}_{U_{cal}}$ was clearly the most significant of the three uncertainties in Equations A.24.

Next, consider an estimate for the uncertainty of the rms fluctuating velocity u_{hw}. Begin by defining the instantaneous velocity, $U_{hw}(t)$, measured by the wire as $U_{hw}(t) = U_{hw} + u_{hw}(t)$ where $u_{hw}(t)$ is the fluctuating velocity component. The uncertainty of the instantaneous velocity, $\hat{U}_{U_{hw}(t)}$ can be estimated as

$$\hat{U}_{U_{hw}(t)}^2 = \hat{U}_{U_{hw},E(t)}^2 + \hat{U}_{U_{cal}}^2 + \hat{U}_{fit}^2 \tag{A.29}$$

similar to Equation A.24 applied to the mean velocity U_{hw}. The first term on the right hand side of Equation A.29, $\hat{U}_{U_{hw},E(t)}$, represents the contribution from the uncertainty in the measured instantaneous voltage, $E(t)$. Upon applying Equation 3.12 in its instantaneous form, $\hat{U}_{U_{hw},E(t)}$ can be expressed as

$$\hat{U}_{U_{hw},E(t)}^2 = \left[\frac{\partial}{\partial E} \left(\sum_{n=0}^{4} a_n \left(E + e(t) \right)^n \right) \times \hat{U}_{E_U,\text{VXI}} \right]^2$$

$$+ \left[\frac{\partial}{\partial e(t)} \left(\sum_{n=0}^{4} a_n \left(E + e(t) \right)^n \right) \times \hat{U}_{e(t)_U} \right]^2 \tag{A.30}$$

$$\approx \hat{U}_{U_{hw},\text{VXI}}^2 + \left[\left(\sum_{n=1}^{4} n \cdot a_n \left(E + e(t) \right)^{n-1} \right) \times \hat{U}_{e(t)_U} \right]^2 \tag{A.31}$$

157

where E was substituted for $E + e(t)$ ($E \gg e(t)$) in the first term on the right hand side of Equation A.30. Substituting Equation A.31 back into Equation A.29 and recalling Equation A.24, the following simplified expression is obtained

$$\hat{U}^2_{U_{hw}(t)} = \hat{U}^2_{U_{hw}} + \left[\left(\sum_{n=1}^{4} n \cdot a_n \left(E + e(t) \right)^{n-1} \right) \times \hat{U}_{e(t)_U} \right]^2 \qquad (A.32)$$

where $\hat{U}_{e(t)_U}$ is the uncertainty in the fluctuating voltage resulting from the amplifier/filter (SR650 – VI) and analog-to-digital converter (IOtech ADC488/8SA – V). The precision limit, $\hat{P}_{e(t)_U}$, was assumed negligible so that $\hat{U}_{e(t)_U}$ was written as

$$\begin{aligned} \hat{U}^2_{e(t)_U} &\approx \hat{B}^2_{e(t)_U} \\ &= \hat{B}^2_{e(t),\text{SR650}} + \hat{B}^2_{e(t),\text{IOtech}} \end{aligned} \qquad (A.33)$$

where expressions for $\hat{B}_{e(t),\text{SR650}}$ and $\hat{B}_{e(t),\text{IOtech}}$ are given in Table A.1. Recalling that the instantaneous velocity is

$$U_{hw}(t) = U_{hw} + u_{hw}(t), \qquad (A.34)$$

it follows that the relationship between the velocity uncertainties is expressible as

$$\hat{U}^2_{U_{hw}(t)} = \hat{U}^2_{U_{hw}} + \hat{U}^2_{u_{hw}(t)}. \qquad (A.35)$$

Assuming the fluctuating velocity, $u_{hw}(t)$, and rms fluctuating velocity, u_{hw}, are related by $u_{hw}(t) \approx \sqrt{2} u_{hw}$, it follows that $\hat{U}_{u_{hw}} \approx \hat{U}_{u_{hw}(t)}/\sqrt{2}$. Comparing Equations A.32 & A.35, the following expression for the uncertainty of the rms fluctuation velocity, $\hat{U}_{u_{hw}}$, is

$$\hat{U}_{u_{hw}} \approx \frac{1}{\sqrt{2}} \cdot \left(\sum_{n=1}^{4} n \cdot a_n E^{n-1} \right) \times \hat{U}_{e(t)_U}. \qquad (A.36)$$

This concludes the uncertainty analysis.

Appendix B

Fluctuating Pressure Measurements on Test-Section Walls

Dynamic pressure measurements were obtained in the test section to identify possible coherent pressure fluctuations, acoustic and/or vortical, present in the *natural* tunnel disturbance environment of the facility. Possible sources of pressure fluctuations include but are not limited to turning vanes, flow treatment devices (honeycomb and screens), tunnel fan system, and flow around sharp corners. The objective here was not to identify the possible sources but to document pressure disturbances in the facility test section that may prove detrimental to this experiment. Special attention was given to the spinning modes generated as a result of the tunnel fan system, rotor-stator interaction.

The goal of these measurements was to identify possible coherent freestream pressure disturbances. Direct fluctuating pressure measurements were obtained using multiple dynamic pressure transducers. Because of the ease of setup associated with flush mounted transducers, the decision was made to acquire the data with the transducers submerged in the turbulent sidewall boundary layers. This was not believed to be a problem since the intent here was not to measure the strength of the coherent disturbances but merely there existence. The unsteady freestream pressure field was

impressed onto the sidewall boundary layers and communicated to the transducers. To eliminate the measurement of coherent structures associated with the turbulent wall layers, transducers were also mounted on opposite sidewalls. The transducers were positioned with separation distances that were large compared to the turbulent length scales of the sidewall boundary layers. Coherence data computed with a transducer on either sidewall were obtained in two independent boundary layers with a common freestream disturbance environment. This suggests that the spectral content of the measured coherence of these submerged transducers were related to that of the freestream coherence data.

The dynamic pressure measurements were acquired using four Endevco differential pressure transducers with a full scale range of $13.8kPa$. The output signals of the transducers were simultaneously sampled using an IOtech ADC488/8SA analog-to-digital converter. The face diameter of the pressure transducers was $2.34mm$. The resonance frequency of the transducers ($70kHz$) was well beyond the frequencies of interest here. The transducers were flush mounted on the sidewalls of the tunnel test section just downstream of the entrance. A schematic showing the transducer locations are shown in Figure B-1. The sketch in the figure represents the first (upstream) test-section door located on the outer loop of the tunnel. The four transducers were labeled **A**, **B**, **C**, and **D**. Transducers **A**, **B**, and **C** were mounted on the door located on the outer loop, and transducer **D** was mounted just opposite of transducer **B** on the inner-loop door. Data from multiple transducers were used to study correlations between sensors. The transducer spacings (order of the test-section cross dimensions) were such that correlations due to both acoustical and vortical freestream disturbances were possible.

B.1   Rotor-stator interaction

The fan system of the tunnel consists of five rotating blades located just upstream of eleven stationary vanes. The interaction of the rotating blades and stationary vanes is a possible source of rotating pressure patterns called spinning modes (see
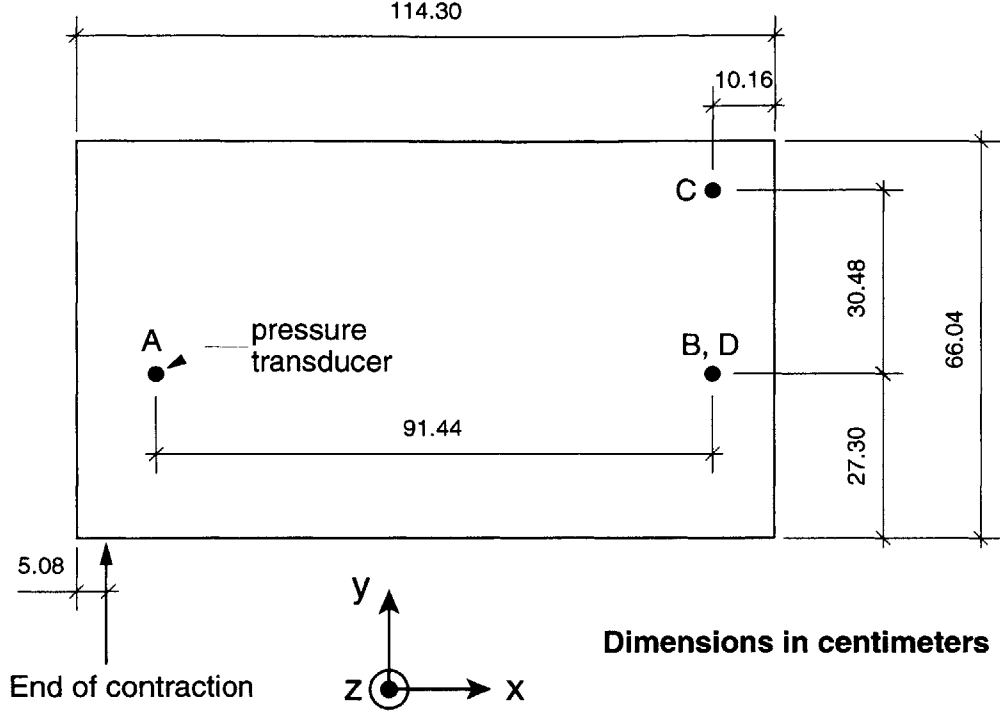
Figure B-1: Pressure transducer arrangement on tunnel sidewall.

work by Tyler and Sofrin [128]). The interaction produces multiple spinning modes corresponding to a single frequency. The structure of the fluctuating pressure field, p, in the vicinity of the interaction region can be written as

$$p(t,\theta) \approx \sum_{n,k} a_{n,k} \cos[(nB + kV)\theta - nB\Omega t + \phi_{n,k}] \tag{B.1}$$

where t denotes time, θ is the circumferential coordinate, $a_{n,k}$ is the amplitude of the (n,k) mode, n denotes the harmonic of the blade passing frequency, k denotes the spatial harmonic produced by the stator vanes, B is number of rotor blades, V is number of stator vanes, Ω is the rotor angular frequency, and $\phi_{n,k}$ is the phase of the (n,k) mode. From Equation B.1, the effective phase speed or spin rate of the propagating mode then becomes

$$\Omega_{eff} = \frac{nB}{nB + kV}\Omega \tag{B.2}$$

where, $n = 1, 2, \ldots$ and $k = \ldots, -1, 0, 1, \ldots$. The circumferential wavenumber m can be defined as $m = nB + kV$. If the spin rate of the m-lobe pattern is sufficiently large, the sound pattern propagates in a spiral pattern with constant amplitude through

161

Figure B-2: Rotor shaft frequency versus tunnel velocity.

the tunnel. On the other hand, if the spin rate is low, the amplitude decays exponentially with distance from the source (evanescent wave). A necessary condition for propagation is that the outer wall sweep speed is supersonic [128]. 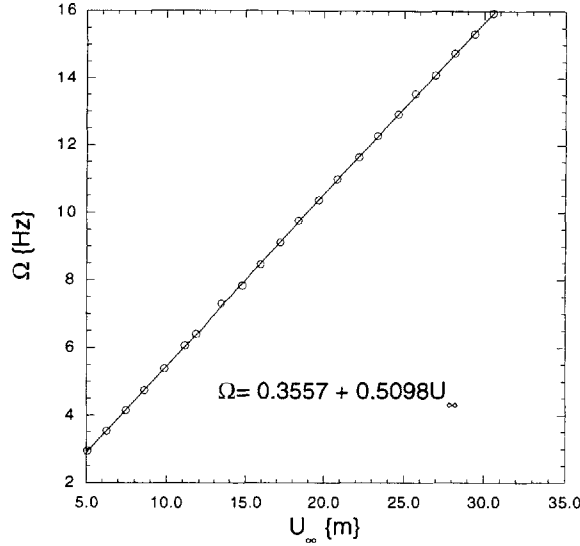If the interacting pattern has fewer lobes, m, than the number of rotor blades, then $\Omega_{eff} > \Omega$ in order to generate the same frequency. It therefore becomes possible to generate propagating modes through the rotor-stator interaction when the rotor tip speed is subsonic. Sofrin [129] described a convenient way to represent the characteristics of rotor-stator interactions by means of modal-frequency spectra.

Before any modal-frequency spectrum can be computed, the rotational speed Ω of the rotor shaft was required. The tunnel drive system is powered by a 30-hp DC motor that drives the rotor shaft via a pulley-belt connection. The rotational speed of the pulley on the DC motor was measured using a Strobotac Type 1531-AB stroboscope for various tunnel speeds. The rotation speed of the DC motor was then related to the rotation speed of the rotor shaft by a simple kinematic equation relating the diameters and rotation speeds of both pulleys assuming no slippage of the belt. A plot of the rotor shaft speed Ω versus tunnel velocity U_∞ along with the corresponding linear regression fit denoted by the line is given in Figure B-2. The value of Ω at the test velocity ($U_\infty = 11.1m/s$) is $\Omega = 6.0Hz$. The radius to the tip
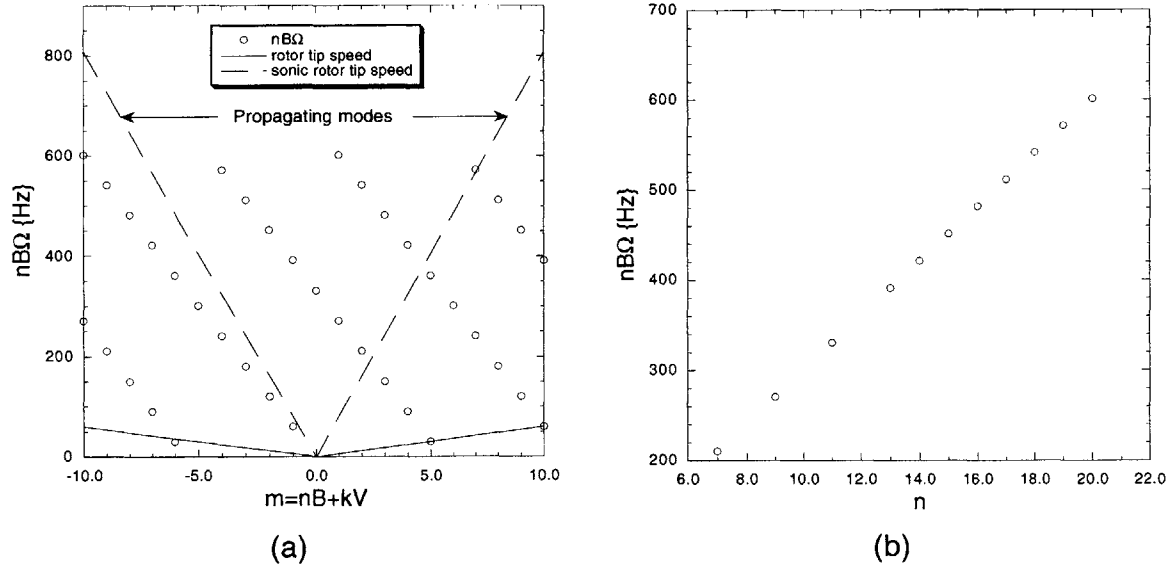
Figure B-3: Plots showing the (a) modal-frequency spectrum and (b) the frequency of the propagating modes for $U_\infty = 11.1 m/s$.

of the rotor blades is $68.0cm$ which implies a rotor tip speed of $25.7m/s$. For a sonic tip speed, the shaft rotation is $\Omega_s = 81 Hz$.

All the required information to compute the modal-frequency spectrum [129] is now available. The modal-frequency spectrum is a plot of the harmonic blade passage frequency versus the circumferential wavenumber for various values of (n, k) as shown in Figure B-3(a). The possible propagating modes are all bounded by the dashed lines denoting the sonic rotor tip speed. All other modes decay exponentially with distance and are not expected to be measurable in the tunnel test section. A positive circumferential wavenumber, m, implies forward spin (same direction as rotor blades) and a negative values of m implies reverse spin. Figure B-3(b) shows the harmonic blade passage frequency versus the blade passage harmonic index n for the propagating modes shown in part (a) of the figure.

B.2   Results of dynamic pressure measurements

The dynamic pressure measurements were acquired using two different data-sampling conditions. For detailed frequency resolution $(0.12Hz)$, 102400 points were sampled
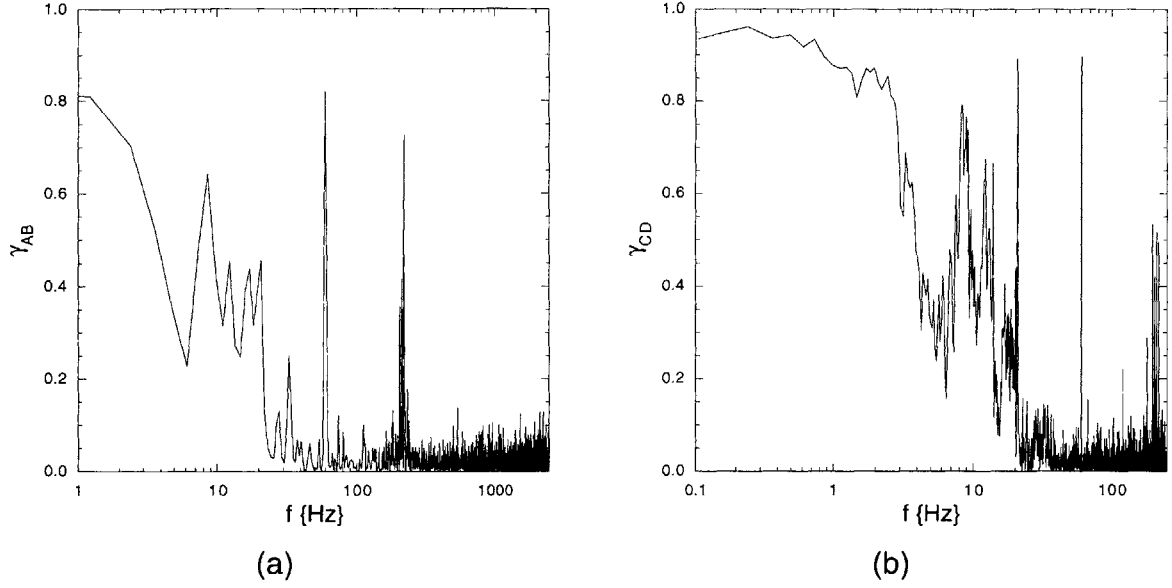
Figure B-4: Coherence function plots for two pairs of submerged pressure transducers for $U_\infty = 12m/s$. Data shown in parts (a) and (b) were obtained with low and high frequency resolution, respectively.

at a rate of $500Hz$ after being band-pass filtered in the range $0.1 < f < 200Hz$. The sampled signal was divided into 49 records (50% overlapping) of 4096 points per records. The second condition was set to obtain data over a wider frequency range, $0.1 < f < 2kHz$, with a frequency resolution of $1.2Hz$. The signal was sampled at a rate of $5kHz$ using the same number of sampled points and record size as the first condition. The data presented here were obtained at $U_\infty = 12m/s$, eight percent larger than the actual test condition. Coherence functions computed using the outputs of two different pairs of pressure transducers are presented in Figure B-4. The subscripts of γ denote the transducer outputs used for the calculation of the coherence function. Note that six coherence functions are computable with each set of measurement. The coherence data shown in parts (a) and (b) were obtained with low and high frequency resolution, respectively. The data show significant coherence at low frequencies, typically $f < 40Hz$. The $60Hz$ electronic noise is evident in both coherence functions. Note the presence of a coherent disturbance at $f \approx 220Hz$ in both coherence plots. This is believed to be related to the lowest propagating mode ($n = 7$) of the rotor-stator interaction field (refer to Figure B-3(b)). Significant co-
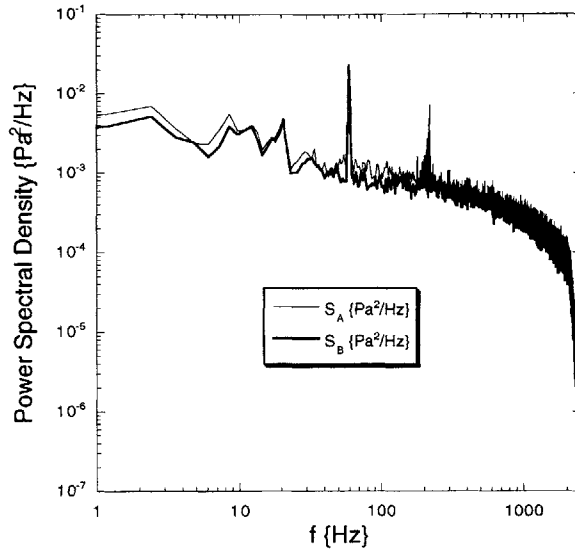
Figure B-5: Typical power spectral densities of two submerged pressure transducers for $U_\infty = 12m/s$.

herence at $f \approx 220Hz$ was observed using the outputs of any pair of transducers. For a lower velocity of $U_\infty = 10m/s$ where the $n = 7$ mode was a borderline propagating mode, the corresponding harmonic was not evident in the coherence data. Note the similarity in coherence function computed with transducers submerged in the same wall layer (part (a) of figure) and γ computed with transducers submerged in different wall layers (part (b) of figure). Two broadband spectra for transducers **A** and **B** are shown in Figure B-5. The coherent disturbance at $f \approx 220Hz$ is clearly evident in both plots along with the $60Hz$ electronic noise. An apparent amplification of this disturbance by the test-section wall boundary layer is believed since the disturbance was not generally detected in freestream spectra obtained using hot-wire anemometry (refer to Figure 4-6). The coherent disturbances present, provided the amplitudes are small as ascertained from hot-wire measurement (refer to Section 4.2) , are not considered to be dangerous for the current experimental study.

Bibliography

[1] O. Reynolds. An experimental investigation of the circumstances which determine whether the motion of water shall be direct or sinuous, and the law or resistance in parallel channels. *Phil. Trans. Roy. Soc. Lond.*, 174:935–982, 1883.

[2] W. Tollmien. Über die entstehung der turbulenz. Nachr. Ges. Wiss. Göttingen, 21–44, 1929. (English translation NACA TM 609, 1931).

[3] H. Schlichting. Zur entstehung der turbulenz bei der plattenströmung. Nachr. Ges. Wiss. Göttingen, 181–208, 1933.

[4] G. B. Schubauer and H. K. Skramstad. Laminar-boundary-layer oscillations and transition on a flat plate. NASA Report 909, 1948.

[5] H. W. Emmons. The laminar-turbulent transition in a boundary layer–Part I. *J. Aeronaut. Sci.*, 18:490–498, 1951.

[6] P. S. Klebanoff and K. D. Tidstrom. Evolution of amplified waves leading to transition in a boundary layer with zero pressure. NASA TN D-195, 1959.

[7] P. S. Klebanoff, K. D. Tidstrom, and L. M. Sargent. The three-dimensional nature of boundary-layer instability. *J. Fluid Mech.*, 12:1–34, 1962.

[8] H. Schlichting. *Boundary-Layer Theory*. McGraw Hill, seventh edition, 1979.

[9] L. M. Mack. Boundary-layer linear stability theory. AGARDOgraph 709, 1984.

[10] H. L. Reed, W. S. Saric, and D. Arnal. Linear stability theory applied to boundary layers. *Ann. Rev. of Fluid Mech.*, 28:389–428, 1996.

[11] W. S. Saric. Görtler vortices. *Ann. Rev. of Fluid Mech.*, 26:379–409, 1994.

[12] A. M. O. Smith and N. Gamberoni. Transition, pressure gradient and stability theory. Technical Report ES 26388, Douglas Aircraft Co., 1956.

[13] J. L. van Ingen. A suggested semi-empirical method for the calculation of the boundary layer transition region. Technical Report V.T.H.-74, Department of Aeronautical Engineering, University of Delft, 1956.

[14] D. M. Bushnell, M. R. Malik, and W. D. Harvey. Transition prediction in external flows via linear stability theory. In J. Zierep and H. Oertel, editors, *Symposium Transsonicum III*, pages 225–242. Springer-Verlag, 1988.

[15] Th. Herbert. Secondary instability of boundary layers. *Ann. Rev. of Fluid Mech.*, 20:487–526, 1988.

[16] M. V. Morkovin. Critical evaluation of transition from laminar to turbulent shear layers with emphasis on hypersonically traveling bodies. Technical Report AFFDL-TR-68-149, Wright-Patterson Air Force Base, 1969.

[17] M. V. Morkovin. On the many faces of transition. In C. S. Wells, editor, *Viscous Drag Reduction*, pages 1–31. Plenum Press, 1969.

[18] E. Reshotko. Boundary-layer stability and transition. *Ann. Rev. of Fluid Mech.*, 8:311–347, 1976.

[19] M. E. Goldstein. The evolution of Tollmien-Schlichting waves near a leading edge. *J. Fluid Mech.*, 127:59–81, 1983.

[20] M. E. Goldstein, P. M. Sockol, and J. Sanz. The evolution of Tollmien-Schlichting waves near a leading edge Part 2. Numerical determination of amplitudes. *J. Fluid Mech.*, 129:443–453, 1983.

[21] M. E. Goldstein. Scattering of acoustic waves into Tollmien-Schlichting waves by small streamwise variations in surface geometry. *J. Fluid Mech.*, 154:509–529, 1985.

[22] N. A. Zavol'skii, V. P. Reutov, and G. V. Rybushkina. Excitation of Tollmien-Schlichting waves by acoustic and vortex disturbance scattering in boundary layer on a wavy surface. *J. Appl. Mech. Tech. Phys.*, 25:355–361, 1984. (English translation, 1983).

[23] A. I. Ruban. On the generation on Tollmien-Schlichting waves by sound. *Fluid Dynamics*, 19:709–716, 1985.

[24] M. Choudhari. Boundary-layer receptivity due to distributed surface imperfections of a deterministic or random nature. *Theoret. Comput. Fluid Dynamics*, 4:101–117, 1993.

[25] J. D. Crouch. Initiation of boundary-layer disturbances by nonlinear mode interactions. In D. C. Reda, H. L. Reed, and R. Kobayashi, editors, *Boundary Layer Stability and Transition to Turbulence*, volume 114, pages 63–68. ASME, 1991.

[26] M. E. Goldstein and L. S. Hultgren. Boundary-layer receptivity to long-wave free-stream disturbances. *Ann. Rev. of Fluid Mech.*, 21:137–166, 1989.

[27] E. J. Kerschen. Boundary layer receptivity. AIAA Paper 89-1109, 1989.

[28] R. A. Heinrich, M. Choudhari, and E. J. Kerschen. A comparison of boundary layer receptivity mechanisms. AIAA Paper 88-3758, 1988.

[29] M. Choudhari and C. L. Streett. Theoretical prediction of boundary-layer receptivity. AIAA 94-2223, 1994.

[30] J. D. Crouch. Theoretical studies on the receptivity of boundary layers. AIAA Paper 94-2224, 1994.

[31] M. Nishioka and M. V. Morkovin. Boundary-layer receptivity to unsteady pressure gradients: experiments and overview. *J. Fluid Mech.*, 171:219–261, 1986.

[32] V . V. Kozlov and O. S. Ryzhov. Receptivity of boundary layers: asymptotic theory and experiment. *Proc. R. Soc. Lond. A*, 429:341–373, 1990.

[33] R. W. Wlezien. Measurement of acoustic receptivity. AIAA Paper 94-2221, 1994.

[34] W. S. Saric, H. L. Reed, and E. J. Kerschen. Boundary-layer receptivity to freestream disturbances. *Ann. Rev. of Fluid Mech.*, 32, 2000.

[35] Yu. S. Kachanov. Three-dimensional receptivity of boundary layers. *Eur. J. Mech. B/Fluids*, 1999. (Accepted for publication).

[36] P. J. Shapiro. The influence of sound upon laminar boundary layer instability. Technical Report 83458-83560-1, M.I.T. Acoustics and Vibration Lab., 1977.

[37] P. Leehey and P. Shapiro. Leading edge effect in laminar boundary layer excitation by sound. In R. Eppler and H. Fasel, editors, *Laminar-Turbulent Transition*, pages 321–331. Springer-Verlag, 1980.

[38] P. Leehey. Influence of environment in laminar boundary layer control. In G. R. Hough, editor, *Viscous Flow Drag Reduction*, volume 72, pages 4–16. American Institute of Aeronautics and Astronautics, 1980.

[39] P. Leehey, C. J. Gedney, and J. Y. Her. The receptivity of a laminar boundary layer to external disturbances. In V. V. Kozlov, editor, *Laminar-Turbulent Transition*, pages 283–294. Springer-Verlag, 1984.

[40] C. J. Gedney. The response of a laminar boundary layer to sound and wall vibration. Technical Report 83560-3, M.I.T. Acoustics and Vibration Lab., 1983.

[41] A. V. Dovgal, Yu. S. Kachanov, V. V. Kozlov, V. Ya. Levchenko, and V. P. Maksimov. Development of perturbations in the boundary layer. *Akad. Nauk USSR, Siberian Div., Inst. Theor. Appl. Mech., Novorsibirsk*, pages 4–22, 1979. (in Russian). (Translated as NASA TM-77986, 1986).

[42] N. G. Ball. Acoustic excitation of Tollmien-Schlichting waves in a laminar boundary layer. Technical Report 321, University of Toronto, Institute of Aerospace Studies, 1987.

[43] D. E. Parekh, P. Pulvin, and R. W. Wlezien. Boundary layer receptivity to convected gusts and sound. In D. C. Reda, H. L. Reed, and R. Kobayashi, editors, *Boundary Layer Stability and Transition to Turbulence*, volume 114, pages 69–75. ASME, 1991.

[44] R. W. Wlezien, D. E. Parekh, and T. C. Island. Measurement of acoustic receptivity at leading edges and porous strips. *Appl. Mech. Rev.*, 43(5):S167–S174, 1990.

[45] W. S. Saric, H. L. Reed, and E. J. Kerschen. Leading edge receptivity to sound: Experiments, DNS, and Theory. AIAA Paper 94-2222, 1994.

[46] W. S. Saric, W. Wie, B. K. Rasmussen, and T. K. Krutckoff. Experiments on leading-edge receptivity to sound. AIAA Paper 95-2253, 1995.

[47] W. S. Saric, W. Wie, and B. K. Rasmussen. Effect of leading edge on sound receptivity. In R. Kobayashi, editor, *Laminar-Turbulent Transition*, pages 413–420. Springer-Verlag, 1995.

[48] W. S. Saric and E. B. White. Influence of high-amplitude noise on boundary-layer transition to turbulence. AIAA Paper 98-2645, 1998.

[49] P. W. Hammerton and E. J. Kerschen. Boundary-layer receptivity for a parabolic leading edge. *J. Fluid Mech.*, 310:243–267, 1996.

[50] P. W. Hammerton and E. J. Kerschen. Boundary-layer receptivity for a parabolic leading edge. Part 2. The small-Strouhal-number limit. *J. Fluid Mech.*, 353:205–220, 1997.

[51] N. Lin, H. L. Reed, and W. C. Saric. Effect of leading-edge geometry on boundary-layer receptivity to freestream sound. In M. Y. Hussaini, A. Kumar, and C. L. Streett, editors, *Instability, Transition, and Turbulence*, pages 421–440. Springer-Verlag, 1992.

[52] W. S. Saric, E. B. White, and H. L. Reed. Boundary-layer receptivity to freestream disturbances and its role in transition. AIAA Paper 99-3788, 1999.

[53] J. M. Kendall. Experiments on boundary-layer receptivity to freestream turbulence. AIAA Paper 98-0530, 1998.

[54] P. S. Klebanoff. Effect of freestream turbulence on the laminar boundary layer. *Bull. Amer. Phys. Soc.*, 10(11):1323, 1971.

[55] Yu. S. Kachanov, V. V. Kozlov, and V. Ya. Levchenko. Occurrence of Tollmien-Schlichting waves in the boundary layer under the effects of external perturbations. *Fluid Dynamics*, 13(4):704–711, 1979.

[56] J. M. Kendall. Experiments on the generation of Tollmimen-Schlichting waves in a flat plate boundary layer by weak free stream turbulence. AIAA Paper 84-0011, 1984.

[57] J. M. Kendall. Experimental study of disturbances produced in a pre-transitional laminar boundary layer by weak freestream turbulence. AIAA Paper 85-1695, 1985.

[58] J. M. Kendall. Boundary layer receptivity to freestream turbulence. AIAA Paper 90-1504, 1990.

[59] J. M. Kendall. Studies on laminar boundary-layer receptivity to freestream turbulence near a leading edge. In D. C. Reda, H. L. Reed, and R. Kobayashi, editors, *Boundary Layer Stability and Transition to Turbulence*, volume 114, pages 23–30. ASME, 1991.

[60] K. J. A. Westin, A. V. Boiko, B. G. B. Klingmann, V. V Kozlov, and P. H. Alfredsson. Experiments in a boundary layer subjected to free stream turbulence. Part 1. Boundary layer structure and receptivity. *J. Fluid Mech.*, 281:193–218, 1994.

[61] A. V. Boiko, K. J. A. Westin, B. G. B. Klingmann, V. V Kozlov, and P. H. Alfredsson. Experiments in a boundary layer subjected to free stream turbulence. Part 2. The role of TS-waves in the transition process. *J. Fluid Mech.*, 281:219–245, 1994.

[62] T. A. Buter and H. L. Reed. Numerical investigation of receptivity to freestream vorticity. AIAA Paper 93-0073, 1993.

[63] M. E. Goldstein and D. W. Wundrow. On the environmental realizability of algebraically growing disturbances and their relation to Klebanoff modes. *Theoret. Comput. Fluid Dynamics*, 10:171–186, 1998.

[64] M. V. Ustinov, M. N. Kogan, V. G. Shumilkin, and S. G Zhigulev. Experimental study of flat-plate boundary layer receptivity to vorticity normal to leading edge. In *Laminar-Turbulent Transition*, 1999. To Appear.

[65] J. H. Watmuff. Detrimental effects of almost immeasurably small freestream nonuniformities generated by wind-tunnel screens. *AIAA J.*, 36(3):379–386, 1998.

[66] L. B. Aizin and N. F. Polyakov. Acoustic generation of Tollmien-Schlichting waves over local unevenness of surface immersed in streams. *Preprint 17, Akad. Nauk USSR, Siberian Div., Inst. Theor. Appl. Mech., Novorsibirsk*, 1979. (in Russian).

[67] W. S. Saric, J. A. Hoos, and R. H. Radeztsky. Boundary-layer receptivity of sound with roughness. In D. C. Reda, H. L. Reed, and R. Kobayashi, editors, *Boundary Layer Stability and Transition to Turbulence*, volume 114, pages 17–22. ASME, 1991.

[68] W. S. Saric, J. A. Hoos, and Y. Kohama. Boundary-layer receptivity: Part 1. Freestream sound and 2D roughness strips. CEAS-CR-R-90191. College of Engineering and Applied Sciences Report, Arizona State University, 1990.

173

[69] M. D. Zhou, D. P. Liu, and R. F. Blackwelder. An experimental study of receptivity of acoustic waves in laminar boundary layers. *Experiments in Fluids*, 17:1–9, 1994.

[70] V. S. Kosorygin, R. H. Radeztsky, and W. S. Saric. Laminar boundary-layer, sound receptivity and control. In R. Kobayashi, editor, *Laminar-Turbulent Transition*, pages 517–524. Springer-Verlag, 1995.

[71] K. S. Breuer, E. G. Dzenitis, J. Gunnarsson, and M. Ullmar. Linear and nonlinear evolution of boundary layer instabilities generated by acoustic-receptivity mechanisms. *Phys. Fluids*, 8:1415–1423, 1996.

[72] R. Kobayashi, Y. Fukunishi, T. Nishikawa, and T. Kato. The receptivity of flatplate boundary-layers with two-dimensional roughness elements to freestream sound and its control. In R. Kobayashi, editor, *Laminar-Turbulent Transition*, pages 507–514. Springer, 1995.

[73] R. Kobayashi, Y. Fukunishi, and T. Kato. Laminar flow control of boundary layers utilizing acoustic receptivity. In *Sixth Asian Congress of Fluid Mechanics*, volume 1, pages 629–632, 1996.

[74] R. J. Bodonyi, W. J. C. Welch, P. W. Duck, and M. Tadjfar. A numerical study of the interaction between unsteady free-stream disturbances and localized variations in surface geometry. *J. Fluid Mech.*, 209:285–308, 1989.

[75] J. D. Crouch. Localized receptivity of boundary layers. *Phys. Fluids*, 4(7):1408–1414, 1992.

[76] M. E. Grimaldi. Roughness-induced boundary layer transition. Master's thesis, Massachusetts Institute of Technology, Cambridge MA, 1994.

[77] J. Gunnarsson and M. Ullmar. On the evolution of roughness induced TS waves in a flat plate boundary layer. Master's thesis, Luleå University of Technology, Sweden, January 1995.

[78] M. Choudhari and E. J. Kerschen. Instability wave patterns generated by interaction of sound waves with three-dimensional wall suction or roughness. AIAA 90-0119, 1990.

[79] J. D. Crouch and F. P. Bertolotti. Nonlocalized receptivity of boundary layers to three-dimensional disturbances. AIAA Paper 92-0740, 1992.

[80] R. W. Wlezien. Measurement of boundary-layer receptivity at suction surfaces. AIAA Paper 89-1006, 1989.

[81] E. Reshotko. Disturbances in a laminar boundary layer due to distributed surface roughness. In T. Tatsumi, editor, *Turbulence and chaotic phenomena in fluids*, pages 39–46, North-Holland, 1984. Elsevier Science Publishers B. V.

[82] T. C. Corke, A. Bar-Sever, and M. V. Morkovin. Experiments on transition enhancement by distributed roughness. *Phys. Fluids*, 29(10):3199–3213, 1986.

[83] M. Wiegel and R. W. Wlezien. Acoustic receptivity of laminar boundary layers over wavy walls. AIAA Paper 93-3280, 1993.

[84] M. Wiegel. Acoustic receptivity of laminar boundary-layers over wavy walls. Master's thesis, Illinois Institute of Technology, Chicago, IL, December 1992.

[85] J. D. Crouch. Non-localized receptivity of boundary layers. *J. Fluid Mech.*, 244:567–581, 1992.

[86] A. J. Dietz. Boundary-layer receptivity to transient convected disturbances. *AIAA J.*, 36(7):1171–1177, 1998.

[87] A. J. Dietz. Local boundary-layer receptivity to a convected free-stream disturbance. *J. Fluid Mech.*, 378:291–317, 1999.

[88] W. S. Saric, V. V. Kozlov, and V. Ya. Levchenko. Forced and unforced subharmonic resonance in boundary-layer transition. AIAA Paper 84-0007, 1984.

[89] W. S. Saric and A. S. W. Thomas. Experiments on the subharmonic route to turbulence in boundary layers. In T. Tatsumi, editor, *Turbulence and chaotic phenomena in fluids*, pages 117–122. Elsevier Science Publishers B. V., North-Holland, 1984.

[90] A. S. W. Thomas. Experiments on secondary instabilities in boundary layers. In J. P. Lamb, editor, *Proceedings of the Tenth U.S. National Congress of Applied Mechanics*, pages 435–443. The American Society of Mechanical Engineers, 1987.

[91] M. T. Landahl. Wave breakdown and turbulence. *SIAM J. Appl. Math*, 28(4):735–756, 1975.

[92] T. Herbert. Three-dimensional phenomena in the transitional flat-plate boundary layer. AIAA Paper 85-0489, 1985.

[93] C. F. Knapp and P. J. Roache. A combined visual and hot-wire anemometer investigation of boundary-layer transition. *AIAA J.*, 6(1):29–36, 1968.

[94] Yu. S. Kachanov, V. V. Kozlov, and V. Ya. Levchenko. Nonlinear development of a wave in a boundary layer. *Fluid Dynamics*, 12:383–390, 1977.

[95] Yu. S. Kachanov and V. Ya. Levchenko. The resonant interaction of disturbances at laminar-turbulent transition in a boundary layer. *J. Fluid Mech.*, 138:209–247, 1984.

[96] T. C. Corke and R. A. Mangano. Resonant growth of three-dimensional modes in transitioning Blasius boundary layers. *J. Fluid Mech.*, 209:93–150, 1989.

[97] A. D. D. Craik. Non-linear resonant instability in boundary layers. *J. Fluid Mech.*, 50:393–413, 1971.

[98] B. Singer, H. L. Reed, and J. H. Ferziger. Investigation of the effects of initial disturbances on plane channel transition. AIAA Paper 86-0433, 1986.

[99] M. Gaster and I. Grant. An experimental investigation of the formation and development of a wave packet in a laminar boundary layer. *Proc. R. Soc. Lond. A*, 347:253–269, 1975.

[100] J. Cohen, K. S. Breuer, and J. H. Haritonidis. On the evolution of a wave packet in a laminar boundary layer. *J. Fluid Mech.*, 225:575–606, 1991.

[101] K. S. Breuer, J. Cohen, and J. H. Haritonidis. The late stages of transition induced by a low-amplitude wavepacket in a laminar boundary layer. *J. Fluid Mech.*, 340:395–411, 1997.

[102] P. J. Schmid and D. S. Henningson. A new mechanism for rapid transition involving a pair of oblique waves. *Phys. Fluids A*, 4(9):1986–1989, 1992.

[103] R. D. Joslin, C. L. Streett, and C.-L. Chang. Spatial direct numerical simulation of boundary-layer transition mechanisms: Validation of PSE theory. *Theoret. Comput. Fluid Dynamics*, 4:271–288, 1993.

[104] S. Berlin, A. Lundbladh, and D. S. Henningson. Spatial simulations of oblique transition in a boundary layer. *Phys. Fluids A*, 6(6):1949–1951, 1994.

[105] P. A. Elofsson and P. H. Alfredsson. An experimental study of oblique transition in plane Poiseuille flow. *J. Fluid Mech.*, 358:177–202, 1998.

[106] M. T. Landahl. A note on an algebraic instability of inviscid parallel shear flows. *J. Fluid Mech.*, 98:243–251, 1980.

[107] P. A. Elofsson, M. Kawakami, and P. H. Alfredsson. Experiments on the stability of streamwise streaks in plane Poiseuille flow. *Phys. Fluids*, 11(4):915–930, 1999.

[108] A. A. Bakchinov, G. R. Grek, B. G. B. Klingmann, and V. V. Kozlov. Transition experiments in a boundary layer with embedded streamwise vortices. *Phys. Fluids*, 7(4):820–832, 1995.

[109] M. Wiegel and M. Fischer. Proper orthogonal decomposition applied to PIV data for the oblique transition in a Blasius boundary layer. In S. S. Cha and J. D. Trolinger, editors, *Optical Techniques in Fluid, Thermal, and Combustion Flow*, volume 2546, pages 87–97. SPIE, 1995.

[110] M. Wiegel and M. Fischer. Utilizing a laser light sheet technique in a boundary-layer flow to study different transition types. In J. P. Crowder, editor, *Flow Visualization VII*, pages 432–437. Begell House, Inc., 1995.

[111] W. S. Saric. Low-speed boundary-layer transition experiments. In T. C. Corke, G. Erlebacher, and M. Y. Hussaini, editors, *Transition: Experiments, Theory & Computations*, pages 1–114. Oxford, 1994.

[112] J. M. Smith. The effect of localized heating on boundary-layer stability and receptivity. Master's thesis, The George Washington University, Washington, DC, July 1995.

[113] E. Ower and R. C. Pankhurst. *The Measurement of Air Flow*. Pergamon Press, 1977.

[114] Frank M. White. *Viscous Fluid Flow*. McGraw-Hill, Inc, New York, New York, 1974.

[115] J. V. Senger and B. Kamgar-Parsi. Representative equations for the viscosity of water substance. *J. Phys. Chem. Ref. Data*, 13(1):185–205, 1984.

[116] J. Kestin and J. H. Whitelaw. Measurements of the viscosity of dry and humid air. In Arnold Wexler, editor, *Humidity and Moisture: Measurement and Control in Science and Industry*, volume 3. National Bureau of Standards, Reinhold Publishing Corporation, 1963.

[117] H. H. Bruun. *Hot-Wire Anemometry: Principles and Signal Analysis*. Oxford University Press, 1995.

[118] K. Bremhorst. Effect of fluid temperature on hot-wire anemometers and an improved method of temperature compensation and linearisation without use of small signal sensitivities. *J. Phys. E: Sci. Instrum.*, 18:44–49, 1985.

[119] J. C. Hardin. Introduction to time series analysis. Reference Publication 1145, NASA, 1986.

[120] J. S. Bendat and A. G. Piersol. *Random Data: Analysis and Measurement Procedures*. John Wiley & Sons, Inc., 1986.

[121] H. S. Kanner. *Evolution of an acoustic disturbance to transition in the boundary layer on an airfoil*. PhD thesis, Virginia Polytechnic and State University, 1999.

[122] R. L. Panton. *Incompressible Flow*. John Wiley & Sons, Inc., New York, New York, 1996.

[123] M. R. Malik. e^{Malik}: A new spatial stability analysis program for transition prediction using the e^N method. High Technology Report No. HTC-9203, Hampton, Virginia, 1992.

[124] T. Herbert and N. Lin. Studies of boundary-layer receptivity with Parabolized Stability Equations. AIAA Paper 93-3053, 1993.

[125] F. P. Bertolotti. *Linear and nonlinear stability of boundary layers with streamwise varying properties*. PhD thesis, The Ohio State University, Columbus, OH, 1991.

[126] D. S. Henningson, A. Lundbladh, and A. V. Johansson. A mechanism for bypass transition from localized disturbances in wall-bounded shear flows. *J. Fluid Mech.*, 250:169–207, 1993.

[127] H. W. Coleman and W. G. Steele. *Experimentation and Uncertainty Analysis for Engineers*. John Wiley & Sons, Inc., New York, New York, 1989.

[128] J. M. Tyler and T. G. Sofrin. Axial flow compressor noise studies. SAE Report 345D, 1961.

[129] T. G. Sofrin. Some modal-frequency spectra of fan noise. AIAA Paper 81-1990, 1981.

4797 - 5